PHYSIK-DEPARTMENT

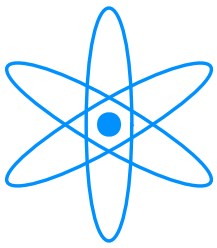

Interplay of structural instability and lattice dynamics in Ni_2MnAl shape memory alloys

Dissertation

von

Tarik Mehaddene

TECHNISCHE UNIVERSITÄT
MÜNCHEN

Physik-Department der
Technischen Universität München
Lehrstuhl für Experimentalphysik 4

Interplay of structural instability and lattice dynamics in Ni_2MnAl shape memory alloys

Tarik Mehaddene

Vollständiger Abdruck der von der Fakultät für Physik der Technischen Universität München zur Erlangung des akademischen Grades eines

Doktors der Naturwissenschaften (Dr. rer. nat.)

genehmigten Dissertation.

Vorsitzender: Univ.-Prof. Dr. M. Kleber

Prüfer der Dissertation:

1. Univ.-Prof. Dr. W. Petry
2. Univ.-Prof. Dr. Chr. Pfleiderer (schriftl. Beurteilung)
   Univ.-Prof. Dr. P. Böni (mündl. Prüfung)

Die Dissertation wurde am 20.12.2006 bei der Technischen Universität München eingereicht und durch die Fakultät für Physik am 12.02.2007 angenommen.

Contents

Zusammenfassung **v**

Summary **ix**

1 Introduction **1**
1.1 Materials with mind . . . 1
1.2 Review of litterature . . . 2
1.3 Outline of this work . . . 6

2 Martensitic transition **7**
2.1 Definitions . . . 7
2.2 Thermodynamics and kinetics . . . 10
2.3 Crystallographic characteristics . . . 11
2.4 The shape memory effect . . . 14
2.5 Superelasticity . . . 15
2.6 Applications . . . 16

3 Ni_2MnAl a high-temperature shape memory alloy **19**
3.1 Ni_2MnAl phase diagram . . . 19
3.2 Sample synthesis . . . 23
3.3 Differential scanning calorimetry . . . 24
3.4 Martensitic transition in Ni_2MnAl alloys . . . 26

4 Single crystal growth **33**
4.1 General considerations . . . 33
4.2 Bridgman method . . . 34
4.3 Czochralski method . . . 35
4.4 Floating-zone technique . . . 37
4.5 Characterisation . . . 38

5 Lattice dynamics theory **43**
5.1 Classical theory . . . 43
5.2 Quantum theory . . . 46
5.3 Phonon density of states . . . 48
5.4 Lattice specific heat . . . 49
5.5 Debye's model . . . 51
5.6 Born-von Kármán model . . . 52

6 Experimental investigation of the normal modes of vibration **53**
6.1 Inelastic neutron scattering 53
6.2 Three-axis spectrometer 55

7 Lattice dynamics in Ni_2MnAl **57**
7.1 Experiment 57
7.2 Phonon dispersions in Ni_2MnAl 58
7.3 *ab-initio* phonons in Heusler Ni_2MnAl 64
7.4 Anomalous $TA_2[\xi\xi 0]$ phonon softening 67
7.5 Elastic neutron scattering 75
7.6 Discussion 78

8 Outlook **83**
8.1 Interplay of magnetism and vibrational degrees of freedom in MSM alloys . 83
8.2 Role of lattice dynamics in domain flipping in martensitic MSM alloys . . . 84

Acknowledgment **87**

Bibliography **89**

Zusammenfassung

Die vorliegende Arbeit untersucht den Zusammenhang von Gitterdynamik und strukturellem Phasenübergang in Ni_2MnAl Formgedächtnislegierungen. Formgedächtnislegierungen haben die Eigenschaften plastische Verformungen durch ein Erhitzen oberhalb der Phasenübergangstemperatur (Martensit-Temperatur) rückgängig zu machen. Der martensitische Phasenübergang steht im Zusammenhang mit einer anomalen Erweichung spezifischer Phononenmoden in der Hochtemperaturphase. Die inelastische Neutronenstreuung, die eine leistungsfähige Methode zur Untersuchung von Schwingungsmoden darstellt, wurde verwendet um dynamische Vorläufer einer strukturellen Instabilität in Ni_2MnAl-Legierungen zu untersuchen.

Die dynamische Differenz-Kalorimetrie (DSC) wurde verwendet um die Phasenumwandlung in Ni_2MnAl-Legierungen zu untersuchen. Hierbei wurde der Einfluß der Zusammensetzung und Anlaßbehandlungen bezüglich der Umwandlungstemperatur untersucht. Die beobachtete Martensitstarttemperatur ändert sich drastisch mit einer geringen Variation der Zusammensetzung. Der Aluminiumgehalt hat hierbei den größten Einfluß auf die Umwandlungstemperatur. Als Ursache kann hierfür die besonders große Änderung des e/a-Verhältnisses angesehen werden, die Aluminium auf den mittleren Wert der Ni_2MnAl-Legierung hat. In Übereinstimmung mit früheren Untersuchungen variert die Umwandlungstemperatur linear mit dem e/a-Verhältnis. Hieraus kann die Schlußfolgerung gezogen werden, dass die Anzahl der Valenzelektronen einen Ordnungsparameter für die strukturelle Instabilität in diesen Heusler-Legierungen darstellt. First-principle Rechnungen, die durch die hier aufgeführten Messungen bestätigt werden, kommen zu der gleichen Schlußfolgerung.

Eine Vorbedingung für die Durchführung von Phononenmessungen mit inelastischer Neutronenstreuung ist die Verfügbarkeit von Einkristallen mit guter Qualität. Die Züchtung von Ni-Mn-Al Einkristallen stellte sich als schwierige und zeitaufwendige Arbeit dar. Zwei Einkristalle mit unterschiedlicher Zusammensetzung konnten mit Hilfe der Czochralski-Method erfolgreich gezüchtet werden. Die Mosaikbreite der Kristalle betrag etwa 1°, was qualitativ hochwertige Phononenmessungen ermöglichte. Akustische und optische Phononen in den Hauptsymmetrierichtungen konnten bei Raumtemperatur gemessen werden. Axialsymmetrische Kraftkonstanten eines Born-von Kármán Modells wurden an die gemessenen Phononenfrequenzen angepaßt. Im Gegensatz zu dem allgemeinen Verhalten der Phononfrequenzen zeigte der $TA_2[\xi\xi 0]$ Phononenast mit Polarisation in $\{1\bar{1}0\}$-Richtung ein anomales Erweichen mit abnehmender Temperatur begleitet vom Erscheinen einer Absenkung im q-Bereich von 0.1-0.25 r.l.u. Dieses Verhalten kennzeichnet niedrige Rückstellkräfte für Bewegungen von (110)-Ebenen in die $[1\bar{1}0]$-Richtung. Derartige Auslenkungen, im Zusammenhang mit Verschiebungen in den (110)-Ebenen, ergeben die Basisebenen der dichtgepackten Tieftemperaturphase. In beiden Proben erniedrigt sich die Absenkung im Phononenast mit abnehmender Temperatur ohne sich jedoch zu einem klaren Minimum bis hinunter zu 10 K zu entwickeln. Die Art der Phononenerweichung, die in den Ni_2MnAl-Legierungen gemessen wurde, entspricht dem Muster der atomaren Auslenkung in die Tieftemperaturmodulation 2M, 10M, 12M und 14M, wie sie in mas-

siven als auch dünnen Filmen von Ni_2MnAl beobachtet wurden.

Der Einfluss der Zusammensetzung auf die Gitterinstabilität wurde durch die Phononenmessungen in zwei unterschiedlichen Kristallen mit den Zusammensetzungen $Ni_{51}Mn_{18}Al_{31}$ und $Ni_{53}Mn_{22}Al_{25}$ mit einem e/a-Verhältnis von 7.29 beziehungsweise 7.59 untersucht. Die Phononendispersion der beiden Proben ähnelt einander sehr. Insbesondere skalieren alle Phononenmoden, mit Ausnahme des $TA_2[\xi\xi 0]$-Astes, mit der Wurzel der Masse und dem Gitterparameter. Im Gegensatz hierzu sind die Phononenfrequenzen des $TA_2[\xi\xi 0]$-Astes, normiert auf die Zonenrandphononen, in der $Ni_{53}Mn_{22}Al_{25}$-Legierung ($e/a = 7.59$) deutlich niedriger. Der Unterschied beträgt bis zu 20% in dem q-Bereich, wo die Phononenanomalie beobachtet wird. Dieses Verhalten, die zunehmende Gitterinstabilität mit zunehmendem e/a-Verhältnis, wurde von *ab-initio*-Rechnungen vorhergesagt. Es erklärt auf der atomaren Skala die DSC Messungen und liefert einen klaren Hinweis auf die Rolle, die das Verhältnis Valenzelektronen pro Atom für die strukturelle Instabilität spielt.

Der Versuch einen einphasigen Ni_2MnAl Kristall mit der $L2_1$-Struktur durch Anlaßglühung eines $Ni_{51}Mn_{18}Al_{31}$ Einkristalls während 45 Tagen bei 673 K herzustellen war nicht erfolgreich. Trotz der langen Glühzeit konnte keine einphasige $L2_1$-Struktur stabilisiert werden, da entweder die Diffusionsgeschwindigkeit zu gering ist oder sich ein Phasengleichgewicht zwischen der B2- und der $L2_1$-Phase einstellt. Phononenmessungen des $TA_2[\xi\xi 0]$-Astes in dieser angelassenen Probe zeigten einen nennenswerten Effekt. Die Absenkung im Phononenast ist noch sichtbar. Der Effekt der Erweichung ist unterhalb von 673 K jedoch deutlich geringer und verändert sich substanziell oberhalb von 673 K, was leicht unterhalb der B2→B2+$L2_1$ Ordnungs-Unordnungs-Umwandlungstemperatur liegt, wie sie in der Literatur berichtet wird. Sowohl der Ordnungsvorgang als auch Ausscheidungbildung können die Änderung bei der Phononenerweichung erklären. Die Bildung von Ausscheidungen durch die lange Anlaßglühung kann eine Änderung des e/a-Verhältnisses bedingen, worauf die Phononen im $TA_2[\xi\xi 0]$-Ast sehr empfindlich sind.

Die Untersuchung der Temperaturabhängigkeit der akustischen Phononen wurde auf die optischen Phononenäste ausgeweitert. Messungen der optischen Phononen in Heusler-Legierungen wurden bislang nicht in der Literatur berichtet. Im Gegensatz zu den Vorhersagen neuerer *ab-initio*-Rechnungen in der $L2_1$-Phase von Ni_2MnAl wurde keine Anomalie in den optischen Phononen mit gleicher Polarisation wie der $TA_2[\xi\xi 0]$-Ast beobachtet. Weder Messungen in der abgeschreckten Probe (B2 Phase) noch in der über lange Zeit geglühten Probe (B2+$L2_1$ Phase) zeigten eine anomale Temperaturabhängigkeit der optischen Moden. Ein normales Absenken der Frequenzen mit steigender Temperatur wurde beobachtet, das vermutlich auf anharmonische Wechselwirkungen zurückzuführen ist. Ob die Diskrepanz zwischen *ab-initio*-Rechnungen und experimentellem Befund auf den Unterschied in der atomaren Ordnung oder der induzierten magnetischen Ordnung zurückzuführen ist, kann hier nicht entschieden werden.

Die anomale Phononenerweichung in Ni_2MnAl wurde mit anderen Ni-basierten Legierungen verglichen. Das Maß der Erweichung ist vergleichbar in unterschiedlichen Ni_2MnAl-Proben und hat den gleichen Umfang wie in NiAl und paramagnetischem Ni_2MnGa.

Das einzige besondere Verhalten wurde im Fall von Ni_2MnGa beobachtet, wenn es ferromagnetisch ordnet und dann eine besonders hohe Phononenerweichung aufzeigt. Unabhängig von der Tatsache, dass die untersuchten Ni_2MnAl-Proben unterhalb von 300 K antiferromagnetisch ordnen, wurde keine wesentlicher Unterschied in der Erweichung der Phononenmoden zwischen der para- und antiferromagnetischer Phase beobachtet. Diese Ergebnisse legen nahe, dass die Magnetisierung der Probe einen starken Einfluß auf die Phononenenfrequenzen mittels einer magnetoelastischen Kopplung hat.

Summary

The work presented here is devoted to investigate the interplay of lattice dynamics and structural instability in Ni_2MnAl shape memory alloys. Shape memory alloys have the ability to recover large stress-induced deformations by heating above the phase transition temperature called *martensitic transition* temperature. The martensitic transition can be related to an anomalous softening of particular phonon modes in the high temperature phase. Inelastic neutron scattering, which is a powerfull technique for investigating normal modes of vibration, is used to get more insight on the dynamic precursors of structural instability in Ni_2MnAl.

Differential Scanning Calorimetry was used to characterise the martensitic transition in Ni_2MnAl alloys. Effects of composition and heat treatments have been investigated. The martensitic transition temperature was found varying rapidly with small changes in the concentration of the constituents. Aluminum has the strongest influence on the martensitic transition. The reason is that its number of valence electrons differs most strongly from the average valence electrons per atom ratio (e/a) of Ni_2MnAl. In agreement with other investigations of Ni-based systems, the measured martensitic transition temperature in Ni-Mn-Al alloys depends linearly on the valence electron concentration. This implies that the number of valence electrons can be considered as an order parameter for the occurrence of structural instabilities in the Heusler alloys. First-principle calculations, verified by the present lattice dynamics measurements, support this idea.

The prerequisite for phonon measurements using inelastic neutron scattering is a good quality single crystal. The growth of Ni-Mn-Al single crystals was a tedious and time consuming task. Two single crystals with different compositions have been succesfully grown using the Czochralski technique. Their mosaic spread were in the order of 1° allowing for good quality phonon measurements. Acoustic and optical phonon modes have been measured at room temperature in the high symmetry directions of the cubic B2 phase. The force constants have been fitted to the measured data using the Born-von Karman model. Contrary to the overall behaviour of the phonon branches, the $TA_2[\xi\xi 0]$ phonon branch with the polarisation $\{1\bar{1}0\}$ showed an anomalous softening with decreasing temperature associated with a wiggle in the q-range 0.1–0.25 r.l.u. This behaviour indicates low-restoring forces against the sliding of the (110) atomic planes in the $[1\bar{1}0]$ direction. Such displacements, associated with atomic shuffles in the (110) planes, constitute basal planes of the close-packed martensite low-temperature phase. In both samples, the wiggle deepens with decreasing temperature but does not result in any clear minimum down to 10 K. The character of the phonon softening measured in Ni_2MnAl corresponds to the pattern of atomic displacements of the modulations 2M, 10M, 12M and 14M observed in bulk and thin-films of Ni_2MnAl.

The effect of the composition on the lattice instability has been investigated by measuring normal modes of vibration in two different crystals, $Ni_{51}Mn_{18}Al_{31}$ and $Ni_{53}Mn_{22}Al_{25}$, with e/a ratios of 7.29 and 7.59 respectively. The phonon dispersions of the two samples resemble very much each other. In particular, all measured normal modes (apart

the $TA_2[\xi\xi 0]$) scale with the square root of the mass and the lattice parameter. On the contrary, phonon frequencies of the $TA_2[\xi\xi 0]$ branch, normalised to the zone boundary phonons, are smaller in $Ni_{53}Mn_{22}Al_{25}$ ($e/a = 7.59$). The difference is enhanced up to 20% in the q-range where the phonon anomaly is observed. This behaviour, synonym of increasing lattice instability with increasing e/a, was predicted by *ab-initio* calculations. It provides an explanation on the atomic scale of the DSC measurements and gives a clear evidence of the role played by the number of valence electrons per atom ratio in structural instability.

The stabilisation of a single $L2_1$ phase in Ni_2MnAl by annealing a $Ni_{51}Mn_{18}Al_{31}$ single crystal at 673 K during 45 days has been attempted. Despite of the long-time annealing, a single $L2_1$ phase could not be stabilised because of either a slow diffusion kinetics or the establishment of an equilibrium between the $L2_1$ and the B2 phases. Phonon measurements of the $TA_2[\xi\xi 0]$ branch in the annealed sample revealed a substantial effect. The wiggle, associated with the anomalous softening, is still present but the degree of softening is smaller below 673 K and changes substantially beyond this temperature which is slightly below the B2$\rightarrow$B2+$L2_1$ order-disorder transition temperature reported in literature. Both ordering effects and precipitates formation can account for this change in the phonon softening. Formation of precipitates, due to the long-time annealing, can lead to changes in the valence electron per atom ratio in the matrix for which the $TA_2[\xi\xi 0]$ phonons are highly sensitive.

The investigation of the temperature dependence of the acoustic phonons has been extended to the optical modes which, to our knowledge, has not been reported in any of similar systems investigated up to now. Contrary to the predictions of recent *ab-initio* phonon calculations in $L2_1$-Ni_2MnAl, no anomaly is seen in the optical phonons with the same polarisation as the $TA_2[\xi\xi 0]$ branch. Neither measurements on the as-quenched sample (B2 phase) nor on the long-time annealed sample (B2+$L2_1$ phase) did reveal any anomalous phonon softening of the optical modes. Indeed, a normal decrease in the frequencies with increasing temperature, presumably due to increasing anharmonicity, is observed. Whether the discrepancy between first-principle calculations and experiment is due to the difference in the atomic ordering or to the induced magnetic order can not be concluded here.

The anomalous phonon softening in Ni_2MnAl has been compared to that of other Ni-based alloys. The degree of softening is comparable in different investigated Ni_2MnAl samples and has the same magnitude as in NiAl and paramagnetic Ni_2MnGa. The only peculiar behaviour is seen in the case of Ni_2MnGa when it orders ferromagnetically in which case a substantial enhancement of the phonon softening is observed. Despite of the fact that the investigated Ni_2MnAl samples order antiferromagnetically below 300 K, no substantial change in the degree of softening has been observed between the paramagnetic and the antiferromagnetic phases. These results suggest that the magnetization of the sample influences strongly the phonon frequencies through a magnetoelastic coupling.

Chapter 1

Introduction

1.1 Materials with mind

Many metallic and intermetallic compounds undergo a martensitic transition, which is a first order, diffusionless, structural solid-solid transformation from a symmetric high-temperature phase called *austenite* to a low-symmetry low-temperature phase called *martensite*. Some of them have the ability to recover large stress-induced deformations by heating through the martensitic transition temperature. They are known as shape memory materials. This property makes them potential candidates for use as actuators, clamps and sensors. Recent studies even suggest that the characteristic distortions of such materials can be exploited to create micrometric machines [Bha05]. It is now well known that these displacive transitions are phonon-triggered and can be explained by strongly temperature dependent interaction which in turn manifests by a softening of particular phonon modes. The suggestion that certain kind of solid-solid phase transitions might be triggered by phonon instabilities was first made by Anderson [And60] and Cochran [Coc64], since then many experimental studies on martensitic materials have been performed.

The crystal structure of a given material depends on its enthalpy and also on its entropy, which plays an increasingly important role as temperature is raised. In nonmagnetic metallic systems, the entropy has two major contributions: the electronic contribution arising from electronic states near the Fermi level, and the vibrational contributions related to the lattice. Basically, the vibrational contribution has two distinct effects: change in the stability of the ordered compound with respect to the random alloy at the same composition (configurational entropy), and change in the phase stability of an alloy or ordered compound in a given configuration with respect to the pure solid constituents (binding enthalpy). The first effect will affect the order-disorder transition temperature and the second effect will affect the formation free energy and may lead to changes in the structure like during a martensitic transition.

More than 50 years ago, Zener was the first to point out that, in general, there is more entropy in the bcc phases, which have lower Debye temperatures, than in their close-packed counterparts [Zen47]. Within this framework, the important point to be stressed is that the phonons corresponding to the atomic motion associated with the structural change

have rather low energy. On the one hand, these soft-phonons confer a large vibrational entropy to the bcc phase and thus are the origin of its thermodynamic stability at high temperature. On the other hand, as a result of the weak restoring forces for these specific atomic motions, these phonons facilitate the mechanical instability that brings the bcc structure toward the close-packed phase (martensite).

Shape memory materials belong to the Hume-Rothery class of materials. They are based on noble (Cu, Ag and Au) or transition metals (Ni, Mn and Co), usually alloyed with *sp*-valence elements. The phase diagrams of these materials are remarkably similar. This is a consequence of the fact that their phase stability is largely dominated by the average number of valence electrons per atom, e/a, but only to lesser degree do they depend on the particular elements in the binary or ternary system. Shape memory alloys have an open bcc structure, denoted as the β-phase, only stable at high-temperatures. For kinetic reasons, the β-phase can be retained as a metastable phase below its stability region by means of a fast enough cooling. In this process, the bcc structure is configurationnaly ordered in the B2, $L2_1$ or DO_3 superstructures. On further cooling, the martensitic transition takes place at a temperature that depends strongly on composition. Because this transition is diffusionless, martensite inherits the ordered arrangement of the high-temperature β-phase. This is obviously very relevant because it ensures that the atomic ordering is not involved in determining the force that drives these phase transitions. Martensite is a close-packed phase that can be described by the application of a combination of shear and shuffle mechanisms to the high-temperature bcc phase. A convenient choice considers the following combinations : $(110)[1\bar{1}0]$ and $(1\bar{1}2)[\bar{1}11]$ homogenous shears together with a superimposed static modulation (or shuffle), which corresponds to a phonon mode on the transverse TA_2 branch, with a specific wavenumber q. This leads to the physical stacking sequences of close-packed planes with a basal plane derived from the $\{110\}$ planes of the β-phase. For instance, the 9R (or 18R in the case of ordered DO_3 or $L2_1$ β-phase) and the 2H structures (in Ramsdell notations) are usually observed in Cu-based alloys. They correspond to the following sequence of close-packed planes: $ABCBCACAB$ for the 9R and AB for the $2H$, and are obtained for the $q = \frac{2}{3}q_{BZ}$ and $q = q_{BZ}$, where q_{BZ} is the Brillouin zone boundary wavenumber in the [110] direction of the β-phase. I come back to these notations in more detail in the next chapter.

1.2 Review of litterature

The simplest materials exhibiting martensitic transitions are the Alkali metals: Li and Na. These exhibit nearly free electron behaviour and the high temperature stable phase has a simple bcc structure. Li and Na undergo a martensitic transformation near 70 K and 35 K respectively. The low temperature structure of Li is now established to be a 9R structure although the transformation may not be complete [Ove84, Smi87]. The low temperature structure of Na is less clear. It was thought to have an hcp structure, but some diffraction study observed a mixture of hcp, 9R and bcc [Sch92].

The lattice dynamics of Li and Na has been studied several years ago. It was noted that there was a large anisotropy in the two transverse modes propagating along the [110] direc-

tion because of the anomalously low value of the elastic constant c'. The ratio $c'/c_{44} = 5$ in Li and Na as determined from neutron scattering measurements [Woo62, Mil71]. Zener noted this over 50 years ago and suggested that this low value of c' is a result of the ion exchange interaction which renders the bcc lattice mechanically unstable with respect to a shear propagating along a [110] direction and displacements along a perpendicular $\langle 1\bar{1}0 \rangle$ direction, referred to as [110]-$\langle 1\bar{1}0 \rangle$ mode. Measurements of the temperature dependence of this phonon branch in Li exhibit a slight softening at the zone boundary between room temperature and just above T_M.

Normal modes of vibration have been also measured in many bcc metals and bcc-based metallic alloys. In the most relevant cases, the data have been obtained by inelastic neutron scattering which is one of the major tools to measure phonon dispersions. A review of neutron scattering studies in bcc-based metals and alloys has been published by A. Nagasawa and Y. Mori [Mor93]. Usually, the frequencies of normal modes of vibration are expected to decrease for increasing temperature due to anharmonic interactions at high temperature, but in martensitic materials, such as in group-III and IV metals, some phonon modes show the opposite behaviour [Pet91a, Pet91b]. Phonon dispersions of the bcc phase of group-III and group-IV metals have been investigated using a unique high-temperature furnace for both growth of single crystals and neutron scattering measurement [Flo87]. The dispersions are dominated by i) a valley of low energy phonons with transverse polarisation and propagation along [112] and [110] directions and ii) a strong dip in the longitudinal branch in the [111] direction for a value 2/3 of the reduced wave vector. The atomic motions corresponding to this mode can be viewed as bringing together two neighbouring (111) planes, while the third stays at rest. This atomic motion gives rise, for a specific wave vector, to the $\beta \rightarrow \omega$ phase transition (Figure 1.1). Actually these characteristics are common to most bcc solids. This behaviour is illustrated in inelastic neutron scattering studies undertaken by Petry and co-workers in group III and IV bcc metals. Furthermore, the phonons along these branches are strongly damped and show at large $\mathbf{q}$ a typical lifetime as short as one vibrational period. This feature seems to be common to other bcc-based materials and is due to their natural instability towards the formation of close-packed structures.

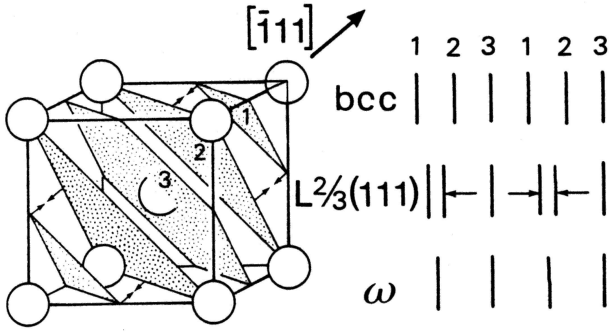

Figure 1.1: $\beta \rightarrow \omega$ transformation scheme taken from [Pet91c]. The ω phase has an hexagonal structure with three atoms per unit cell with $a_\omega = a_\beta\sqrt{2}$ and $c_\omega = a_\beta\sqrt{3}/2$, where a_β is the lattice parameter of the bcc Bravais lattice. The c- and a-axis of the ω-phase point along the [111] and [110] directions of the bcc lattice respectively.

Petry and co-workers have extended the investigation of the lattice dynamics to binary compounds. Phonon dispersions in Zr-Nb and Ti-Cr systems revealed anomalous phonon softening of the $TA_2[\xi\xi 0]$ and the $TA_2[\xi\xi 2\xi]$ phonon branches. The degree of softening has been found to decrease substantially witht Nb content, synonym of increasing lattice stability with increasing Nb content. Elastic neutron scattering performed in Zr-Nb samples revealed the presence of a diffuse elastic signal which has been identified as the result of static lattice displacements due to the misfit of the Nb atoms in the Zr matrix [Neu91]. The diffuse scattering appears mostly at q-positions where low-lying phonons are observed. This can be explained by the "*weakness*" of the lattice a these q-positions.

The low-lying TA_2 phonon branch has attracted the attention of many scientists and has been the subject of numerous studies in a number of shape memory alloys. Cu-based materials are among the most investigated ones [Man93, Man99, Nic00]. The low value of the whole $TA_2[\xi\xi 0]$ branch plus the low value of the corresponding elastic constant $c^{'}$ show that the bcc structure has a low dynamical stability for deformations on the $\{110\}$ planes along $\langle 1\bar{1}0\rangle$ direction with wave vectors spanning over the entire Brillouin zone. Such an incipient dynamical instability becomes more pronounced as the alloys approaches the transition temperature; in this case the whole $TA_2[\xi\xi 0]$ softens anomalously upon cooling. However, as occurs with the elastic constant $c^{'}$, the phonon softening is not complete in the sense that there is no frequency that reaches zero value at the transition temperature which is a clear evidence of the first-order character of the martensitic transition. For Cu-based alloys, it has been shown that the frequencies of the $TA_2[\xi\xi 0]$ branches are very similar, with a value at the zone boundary of approximately 1 THz. Lattice dynamics of CuAlMn have been intensively studied by K. Nicolaus in the frame of his Ph.D performed at the E13 institute [Nic00]. Normal modes of vibration of 6 different crystals have been investigated by inelastic neutron scattering. The phonon frequencies of the $TA_2[\xi\xi 0]$ branches have been found very similar with a value at the zone boundary of approximately 1 THz. The $TA_2[\xi\xi 0]$ mode with $\xi = 2/3$ leads to the stacking sequence with a modulation of 3, 9, 18 that is to martensite 3R, 9R and 18R, respectively; whereas the $TA_2[\xi\xi 0]$ mode with $\xi = 1$ leads to the martensite structure 2H. Even if in the investigated range of Al and Mn contents both 18R and 2H martensite structures have been observed, no particular enhancement in the softening of the two responsible modes has been observed in CuAlMn. This can be explained by the small difference in the free energy of the two martensite structures which may lead to the simultaneous decrease in the frequency of the two modes and by the way to the continuous softening of the $TA_2[\xi\xi 0]$ branch over the whole Brillouin zone. It has been stated that in the case of CuAlMn the selection of the modulation of the low-temperature phase cannot be exclusively determined by the anomalies of the $TA_2[\xi\xi 0]$ branch; rather, the final structure selected by the alloy depends on small details of the internal energy such as local defects.

Besides the Cu-based shape memory alloys the Ni-based alloys are the second most investigated systems. Since 1962, year of the discovery of the shape memory effect in NiTi by the US Naval Ordinance Laboratories [Bue63], NiTi has attracted the attention of many research groups. Special research programs have been devoted to the study of its thermodynamic and physical properties. Whereas the microstructural and thermomechanical

properties of NiTi have been extensively investigated, only few works have been devoted to the dynamical properties of its martensitic transition. To our knowledge, the only attempts to measure the phonon dispersion curves of NiTi turn back to early eighties. Most of measurements were restricted to the acoustic modes. Measurements of the optical phonons turned out to be exceptionally difficult because of their extremely low intensities. Even so, large discrepancies have been observed. Tietze *et al.* [Tie84] have investigated acoustic phonon branches in [110] and [111] directions in the austenitic B2 phase at different temperatures. They observed a complete softening of the $TA_2[\xi\xi 0]$ phonon mode at a reduced wave vector value of 0.33 at 338 K in contrast to the measurements of Bührer *et al.* [Buh81] where a small minimum in the frequency of the same branch has been measured near to this wave vector. Besides, Tietze *et al.* have found a normal behaviour of the major part of the $LA[\xi\xi\xi]$ with no crossover of the $TA[\xi\xi\xi]$ branch in disagreement with the predictions of Bruinsma *et al.* [Bru82], which were fitted to the data of Bührer *et al.*. Recent first-principle *ab-initio* calculations of the phonon dispersions in B2 NiTi predict lattice instabilities in different branches throughout the entire Brillouin zone [Hua01]. Along with the anomalous phonon softening, various anomalies in the physical properties of NiTi have been reported prior to the martensitic transition, e.g. anomalous peak in the electrical resistivity and supperlattice reflections in neutron and x-ray diffraction patterns. Whether these precursor effects are due to the martensitic transition itself or to the appearance of premartensitic intermediate phase (called R phase) is up to now ambiguous. Recent progress in the NiTi phase diagram showed multiple step transformation in NiTi are likely to occur when Ni_4Ti_3 precipitates form within the matrix and it is now possible through a substantial heat treatment to monitor single step B2→B19 transformation and avoid any intermediate phase [Kha02].

Among the Ni-based shape memory alloys, the Heusler Ni_2MnGa is of particluar interest owing to its magnetic properties. This system undergoes a martensitic transition within its ferromagnetic phase. It is thus a promising candidate for a new class of functional materials in which the shape recovery can be explored by an external magnetic field. In the martensitic state, the application of a magnetic field can cause strains up to about 10% [Soz02]. Lattice dynamics of Ni_2MnGa has been investigated by inelastic neutron scattering [Zhe95]. A wiggle in the $TA_2[\xi\xi 0]$ branch which deepens with decreasing temperature resulting in a distinct minimum at $\xi_0 = 0.33$ below 300 K has been revealed. Furthermore an enhancement of the phonon softening when Ni_2MnGa orders ferromagnetically has been observed. Ni-Mn-Al and Ni-Mn-Ga are isoelectronic at equal Ga and Al concentrations when the Ni and Mn contents are kept constant. Stoichiometric Ni_2MnAl is structurally stable down to the lowest temperatures, but martensitic transformations occur in the slightly off-stoichiometric compounds, and their mechanical properties are more favorable than those of the relatively brittle Ni_2MnGa. It is, therefore, thought that Ni_2MnAl could be an alternative material if its magnetic shape memory properties are as favorable as those of Ni_2MnGa.

1.3 Outline of this work

This work reports on the interplay of lattice dynamics and strutural instability in Ni_2MnAl shape memory alloys. Basic properties of martensitic transition and its link to anomalous phonons softening is the topic of the chapter 2. Chapter 3 is devoted to the structural and physical properties of the Ni-Mn-Al system. The polycrystalline sample preparation and the characterisation of their martensitic transition using Differential Scanning Calorimetry are also presented. Prerequisite for phonon measurements using inelastic neutron scattering is the growth of single crystals. Relevant details of the experimental techniques used to grow and characterise Ni-Mn-Al single crystals are the topic of chapter 4. Lattice dynamics theory and related thermodynamics relevant for the method of investigation and data analysis are presented in chapter 5. A brief overview of inelastic neutron scattering using the three-axis spectrometer is given in chapter 6. The reader is referred to several references for more details. The results of phonon measurement are presented and discussed in Chapter 7. We start first to present the dispersion curves of both optical and acoustic phonons $Ni_{51}Mn_{18}Al_{31}$. The phonon density of state and related thermodynamic quantities are deduced. The central aspect is the temperature dependence of the normal modes of vibration. Anomalous phonon softening, related to which shuffle modes contribute to the martensitic transition, is revealed. Finally, the phonon softening measured in Ni_2MnAl is compared to that of other Ni-based systems.

Chapter 2

Martensitic transition

In this chapter, the key microscopic and macroscopic aspects of martensite will be qualitatively reviewed. Although one may be tempted to pass over some of the microscopic aspects, it must be emphasized that these form a foundation upon which subsequent discussions of the results presented in the next sections are based. After an introduction to martensite, the shape memory effect itself will be introduced, along with the related phenomenon called superelasticity.

2.1 Definitions

Solid state transformations are usually of two types: diffusional and displacive. Diffusional transformations are those in which a new phase can only be formed by moving atoms over relatively long distances. Since long range diffusion is required, the progress of this type of transformation is dependent upon both time and temperature. In contrast, displacive transformations do not require such long-range movements. In this case, atoms are cooperatively rearranged into a new, more stable crystal structure, without changing the chemical nature of the matrix. These displacive transformations generally progress in a time-independent fashion because no atomic migration is involved. They are referred as athermal transformations, since the amount of the new phase present is usually dependent only on temperature, and not amount of time at temperature.

Martensitic transformations are generally of this second type, and are formed upon cooling from a higher temperature phase called the austenite phase, or *austenite* to a low temperature phase called *martensite*. The terms martensite and austenite were originally intended to refer only to phases of steels; although some argue the point, the more generalized definition referring to the type of transformation product, and not the particular material, is now widely accepted. Martensitic transformations are first-order transformations, meaning that heat is liberated when martensite is formed. There is a hysteresis associated with the transformation and there is a temperature range over which austenite and martensite co-exist. Crystallographically, the transformation from austenite to martensite is often thought of in two parts: the bain strain and the lattice-invariant shear. Although these can be crystallographycally quite complex, a qualitative two-dimensional description can be quite useful for a better understanding.

The bain strain consists of all atomic movements needed to produce the new structure

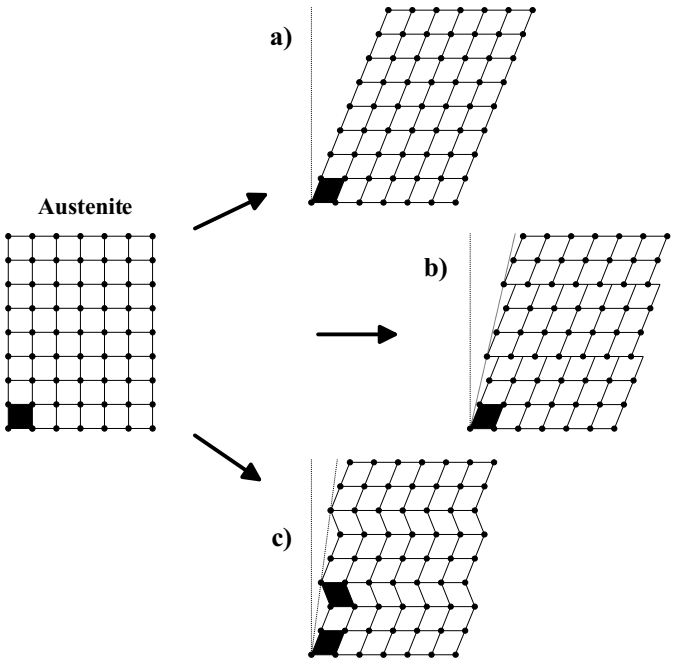

Figure 2.1: The transformation from austenite to martensite is shown schematically in two dimensions, (a) bain strain, (b) accomodation by slip and (c) accomodation by twinning. The shear angle γ is clearly smaller in cases (b) and (c) and lead to smaller stresses.

from the old (Fig. 2.1(a)). The second part of a martensitic transformation, the lattice invariant shear, is an accommodation step: the martensitic structure produced by the bain strain is of different shape, and often volume, than the surrounding austenite. Either the overall shape of the new phase, or the surrounding austenite must be altered to accommodate the new structure. There are two general mechanisms by which this can happen: slip (Fig. 2.1(b)) and twinning (Fig. 2.1(c)). In both cases, each individual cell, or parallelogram, has the new martensite structure, but the overall shape is that of the original austenite. Slip is a permanent process and is a common accommodation mechanism in many martensites. Twinning can accommodate shape changes in a reversible way. For a shape memory to occur to any significant extent, we require that accommodation be fully reversible, or in other words, that the twinning be the dominant accommodation process.

The twinning process of accommodation plays a key role in the shape memory effect and should be reviewed in more details. As can be seen in Fig. 2.1(c) the twin boundary is a mirror plane: when positioned on the boundary, the view in one direction is a mirror of the other. Some key properties of twin boundaries are that they are of a very low energy and that they are quite mobile. Thus the relative stability of martensite phase is not strongly affected by the number or location of these boundaries. By comparing the edges of the structure shown if Fig. 2.1(b) and (c) one can see that slip accommodation requires that atomic bonds be broken, while all bonds remain intact in the twined structure. If a stress is applied to the structure shown in Fig. 2.1(c), the twin boundary will easily move, producing a shape which better accommodates the applied stress. The result of moving a twin boundary is to convert one orientation or twin variant into another. That variant will be chosen which is most favorably oriented to the applied stress. This process is called detwinning.

From a macroscopical point of view, a variety of significant properties are affected dur-

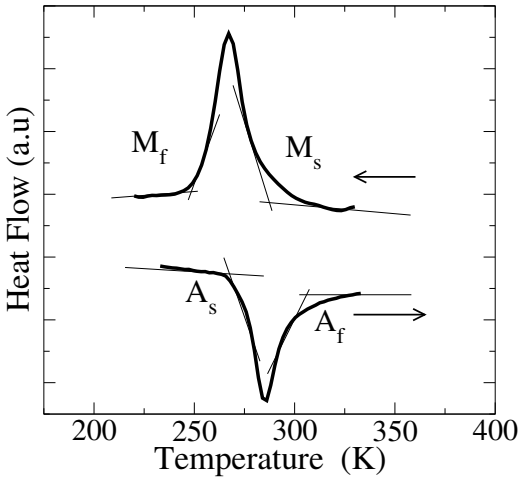

Figure 2.2: Typical plot of heat flow vs. temperature for a martensitic transformation occuring in shape memory alloys from which the characteristic transformation temperatures M_s, M_f, A_s and A_f are determided.

ing a martensitic transformation: resistivity, volume change, heat-flow etc. Any of these can be used to follow the progress of the martensitic transformation, as is illustrated in Fig. 2.2. The figure shows a heat-flow evolution recorded on a NiTi sample by means of a differential scanning calorimeter (DSC) during heating up and cooling down. Detailed description of a DSC will be given in one of the next sections. The temperatures M_s,M_f, A_s and A_f are illustrated in the graph and refer to the temperature at which the transformation to martensite (forward) starts and finishes, and the temperature at which the transformation to austenite (backward) starts and finishes. Note that there is a hysteresis associated with martensitic transformation; in other words transformation temperatures differ upon heating and cooling. The magnitude of hysteresis depends upon the alloy, but values of 20-50 K are typical for shape memory alloys. Microscopically, hysteresis can be thought as the friction associated with movement of twin-related martensite boundaries.

Figure 2.3: Optical micrograph showing martensite plates and surface relief in a self-made NiTi shape memory alloy. The cross section has been mechanically polished and etched.

Martensite normally appears as plates, resting on complex crystallographic planes called habit planes. In many shape memory alloys, the martensite plates are large and can be easily viewed through an optical microscope. Fig. 2.3 shows a micrograph of the typical martensitic material NiTi with different plates giving rise to a surface relief that one can easily feel by rubbing a finger over the surface. This is understood by considering that the plates at the surface are not constrained in three dimensions and need not to be accommodated in a direction normal to the surface.

2.2 Thermodynamics and kinetics

In order to induce a martensitic transformation, the free energy of the martensite must be lower than that of the austenite. However, since the transformation requires an excess of non-chemical energy (such as transformation strain energy and interface energy), if the difference in the free energy of both phases is not greater than the energy barrier, the transformation will not begin. In other word, a driving force is necessary. If the specimen is not supercooled to a suitable low temperature M_s below the equilibrium temperature T_0 (where the free energy of the martensite and the austenite phase are equal), the transformation will not progress (see Fig. 2.4). A driving force is also necessary for the reverse transformation. The specimen must be superheated to a suitably high temperature A_s above T_0. A martensitic transition in shape memory alloys has a thermoelastic character, which means that at each temperature and level of applied stress within the transformation range, thermoelastic equilibrium is achieved [Pla92]. The equilibrium condition is defined by a local balance at the transforming interfaces between competing forces. In the forward (austenite to martensite) transition, the driving force promoting martensite is balanced by the increase in elastic (strain and interfacial) energy. In the reverse transition the elastic energy previously stored promotes, together with the driving force, the reversal into the austenite phase. An ideal thermoelastic transition would proceed without hysteresis. In shape memory alloys the hysteresis is small and is a consequence of different dissipative effects operating during the transition. When the transition is thermally induced and a polyvariant martensite develops, the dominant mechanism of hysteresis has its origin in the relaxation of the elastic strain energy arising from the self-accommodation process and from the interaction between the martensite variants. The relaxation of the elastic strain energy has been found to depend on the specific crystallographic structure of the growing martensite [Ort91]. A different scenario occurs when the transition is stress-induced; the intrinsic hysteresis arising from a single interface transformation has its origin in the interaction of the interface with dislocations [Lov90]. Actually, such an intrinsic hysteresis is very small.

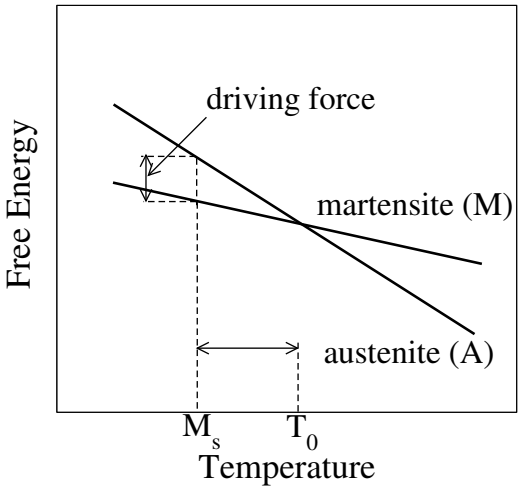

Figure 2.4: Temperature dependence of the chemical free energy of the austenite and martensite phases and their relation to martensitic transformation.

From a kinetic point of view, these transitions are athermal, which means that, contrary to thermally activated systems, thermal fluctuations do not play any relevant role [Chr75]. When cooling from the high-temperature phase, the transition starts at a given temperature. However, the system need to be continously cooled down to increase the transformed fraction of the new phase. At any temperature in the two-phase region, the transition appears to be instantaneous in practical time scales, and hence the transformed fraction virtually does not depend on time, i.e., it increases each time the temperature is lowered. The transition is not completed until the temperature is lowered below a certain value M_f. Hence, in these transitions, the temperature plays the role of an external controlling parameter that determines the free-energy difference between the high- and the low-temperature phases. This free-energy difference provides the driving force for the transition.

Accurate observations [Pla81, Pla82] have revealed that these transitions proceed through a series of discrete jumps connecting metastable equilibrium states separated by high energy barriers ($\gg k_B T$, where k_B is the Boltzmann constant). In these states the thermoelastic equilibrium condition is satisfied. At each step, elastic energy is stored in the system and, at the same time, energy is released, at each new metastable situation, the temperature of the system must be lowered again to restart transformation. For low enough temperature rates, however, avalanches take place in time intervals much smaller than the time of appreciable variation of the driving force. Thus the system spends the overwhelming majority of its time in a situation of thermoelastic equilibrium.

During the avalanches the irreversible energy is (at least partially) released in the form of transient elastic waves. They are emitted in the ultrasonic range and are known as acoustic emission [Pas75, Bar81]. These acoustic waves contain dynamic information of the mechanism associated with the structural change, or source mechanism, which has generated them. Several models have been developed aiming to describe the source mechanism during martensitic transitions [Wad84, Yu87, Man90]. Experiments corroborate that the acoustic radiation pattern mainly corresponds to $\{110\}\langle 1\bar{1}0\rangle$ martenstitic shear mechanism but that it also contains a small effect due to a volume change mechanism [Man89].

2.3 Crystallographic characteristics

Most of the alloys which sustain thermoelastic martensitic transformations have superlattice structures and, almost all of the fundamental lattices are body-centered cubic (bcc). They are classified as β phase alloys. Accordingly, the following describes characteristics of the crystal structures of the austenite and martensite phases which occur in β phase alloys. Figure 2.5 illustrates the crystal structure of a CsCl (B2) austenite phase. It shows the three dimensional structure (a) and the arrangement of the atoms within the (110) plane (b) and above or below (c). The cubic structure in (a) can be viewed as the result of alternately stacking the planes in picture (b) and (c).

The martensitic transformations which occur in these β phase alloys are basically due to the deformation (toward a hexagon) of the (110) planes themselves, and a shearing (including some shuffeling) in the $[1\bar{1}0]$ direction along the (110) plane. Accordingly, the resulting martensitic crystal structure consists of the three types (A,B,C) of close packed

atomic planes shown in Fig. 2.6. The complete structure is constructed by regularly stacking these components in various orders as shown in Fig. 2.7. Such crystals are called *periodic stacking ordered structures*. Martensite created in a β phase alloy can have one of the periodic stacking structures in Fig. 2.7. Labels below the structures such as $(1\overline{1})$ and $(1)_3$ are Zhdanov's notation; symbols such as 2H and 3R are Ramsdell's notation. These notations are widely used as a technique for representing periodic stacking order structures. In the Ramsdell system, H and R indicate the symmetry in the direction vertical to the basal plane. Respectively, they signify and are the first letters of *hexagonal* and *rhombohedral* symmetry. However, these symbols alone cannot provide a complete description of the stacking order. The Zhdanov notation better represents the differences in the stacking order.

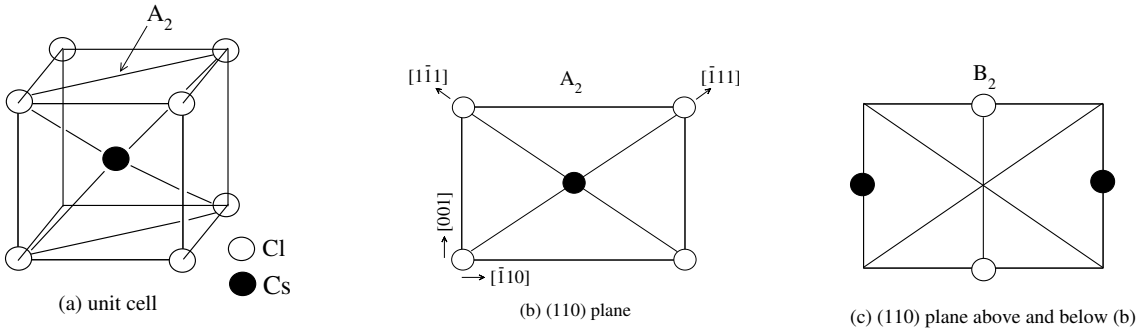

Figure 2.5: Crystal structure of CsCl-type B2 supperlattice and the alternately stacked (110) planes (A_2 and B_2).

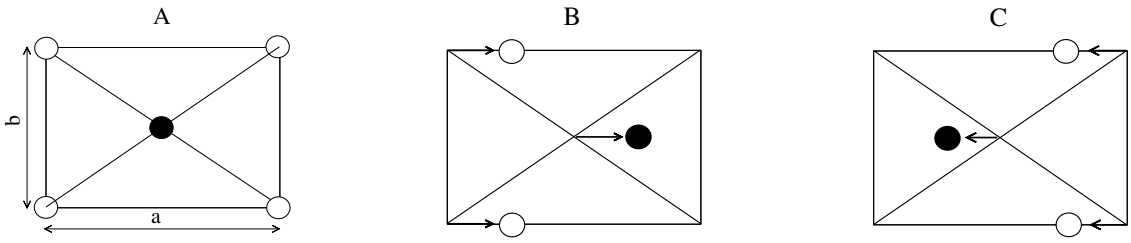

Figure 2.6: Three type of close-packed stacking planes in Martensite with periodic stacking structure produced from a CsCl-type austenite phase.

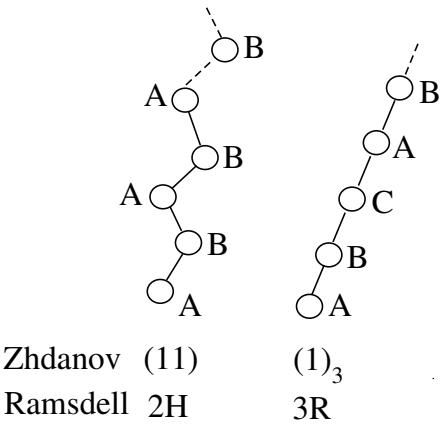

Figure 2.7: Examples of periodic stacking sequences of martensite produced from the CsCl austenite phase. Both notations of Ramsdell and Zhdanov are given.

Table 2.1: Crystallographic characteristics of austenite and martensite phases in a number of shape memory alloys, and phonon modes associated with the stacking sequence. The notation used for the martensite is the most widely used in the litterature.

Material	Austenite phase (space group)	Martensite (space group)	Crystal system	Phonon mode
Ternay Cu-based				
$e/a \geq (e/a)_{eu}$	$L2_1/DO_3$ ($Fm3m$)	2H ($Pnmm$)	Hexagonal	[110]
$e/a \leq (e/a)_{eu}$	$L2_1/DO_3$ ($Fm3m$)	18R ($I2/m$)	Orthorhombic	$\frac{2}{3}$[110]
Cu_xZn_{1-x} $x \approx 0.6$	B2 ($Pm3m$)	9R ($P2/m$)	Orthorhombic	$\frac{1}{3}$[110]
Ni_xAl_{1-x} $0.6 \leq x \leq 0.69$	B2 ($Pm3m$)	7R ($P2/m$)	Orthorhombic	$\frac{1}{7}$[110]
Ni_xTi_{1-x} $x \approx 0.5$	B2 ($Pm3m$)	B$'$19 ($P2/m$)	Monoclinic	$\frac{1}{3}$[110]
Au_xCd_{1-x} $x \approx 0.5$	B2 ($Pm3m$)	ξ' ($P2/m$)	Monoclinic	$\frac{1}{3}$[110]
$AuCuZn_2$	$L2_1$ ($Fm3m$)	18R ($I2/m$)	Orthorhombic	$\frac{1}{3}$[110]
Ni_2AlMn	$L2_1$/B2 ($Fm3m$)	7R-15R ($P2/m$-)	Orthorhombic	$\frac{1}{3}$[110]
Ni_2MnGa	$L2_1$ ($Fm3m$)	18R ($I2/m$)	Orthorhombic	$\frac{1}{3}$[110]

2.4 The shape memory effect

Although it has not been explicitly stated, it is implied from above examples that martensite is generally of a lower symmetry phase than austenite. The consequence of this is that there are several ways in which martensite can form from austenite, but there is only one possible route which will return the austenite structure. In our two-dimensional example in Fig. 2.1, two shear directions can be applied to the squares to produce two different rhombus variants, but there is no other possible variants of austenite so both of these rhombus shapes would have to return to the same square geometry shown in Fig. 2.1. The simple geometrical concept becomes the foundation for the shape memory effect. Upon cooling from the austenite, the self-accommodation variants of martensite are formed. The twin boundaries migrate during deformation resulting in a biased distribution of martensite variants. But whatever the distribution of martensite is, there is only one possible reverted structure and with reversion to austenite must return the original shape.

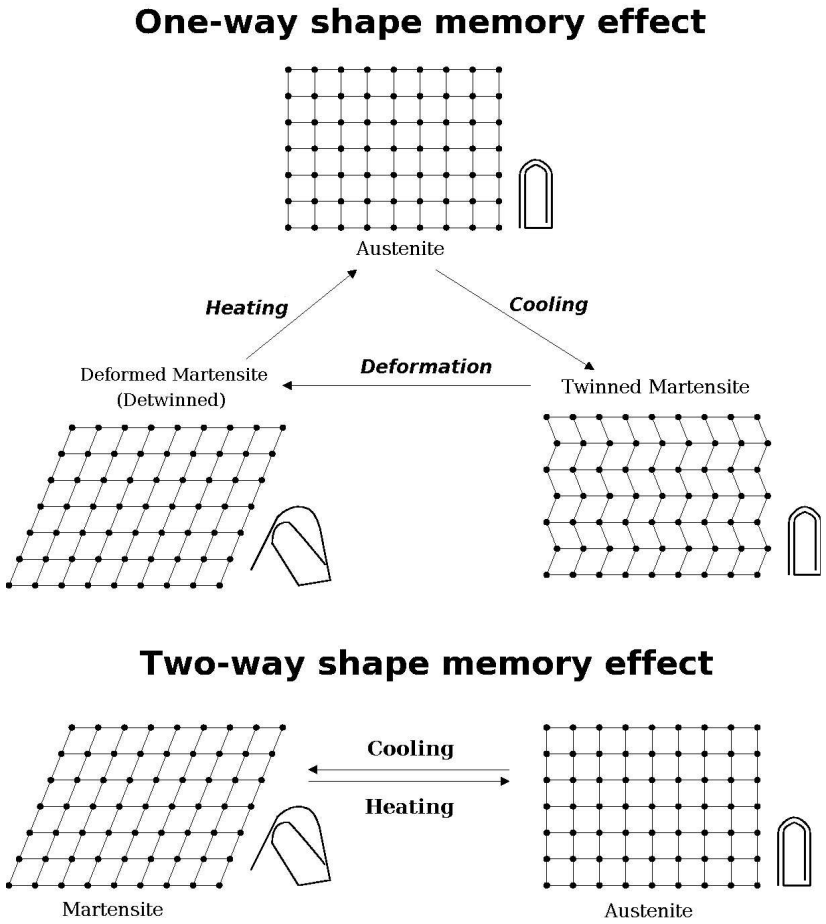

Figure 2.8: Comparison of the one-way (upper) and the two-way shape memory effects using a paper clamp and a schematical square lattice.

The shape memory effect can be described with reference to the cooling and heating curves in Fig. 2.8. There is no change in the shape of the specimen cooled from above A_f to below M_f. When the specimen is deformed below M_f it remains so deformed until it is heated. The shape recovery begins at A_s and is completed at A_f. Once the shape has recovered at A_f there is again no change in shape when the specimen is cooled below M_f and the shape memory can only be reactivated by deforming the martensitic specimen once again. For this reason, this phenomenon is frequently referred to as one-way shape memory effect. Through several thermomechanical treatments, called *training*, one may achieve a two-way shape memory effect in which the shape recovery takes places only by monitoring the temperature without any external deformation. The two-way shape memory effect can be realized in shape memory materials, whereby a specimen is programmed by means of thermomechanical treatment producing mictrostresses in the austenite phase which in turn program the specimen to behave as a stress-induced martensitic transformation. That is, the microstresses favor only a single orientation of martensite upon subsequent cooling, which produces a spontaneous deformation. When the specimen is heated up the normal one-way shape memory process occurs and its original shape is reproduced. The two-way process can be repeated indefinitely (as a thermostat) as opposed to the one-way memory, which is one time only operation.

2.5 Superelasticity

The discussion up to now shows that the shape memory effect is both thermal and mechanical. The martensite is initially formed upon cooling and is then deformed below the M_f temperature then heated above A_f temperature to cause the shape recovery i.e., the shape memory is caused by heating. We now consider another type of shape recovery which is temperature independent: *superelasticity*.

Normally on cooling, the martensite forms at M_s under no applied stress. But in some materials, martensite can form above M_s if stress is applied, and the martensite so formed is called stress-induced martensite. The driving force of the transformation is now mechanical, as opposed to thermal. Above M_s the stress required to produce stress-induced martensite increases with increasing temperature. In fact the variation in the stress needed to produce stress-induced martensite increases linearly with temperature above M_s. The increase in difficulty to stress-induce martensite continues to increase with temperature until M_d, above which the critical stress for inducing martensite is greater than that needed to move dislocations - this makes M_d the highest temperature at which it is possible to have martensite. Thus the temperature range for stress-induced martensite is from M_s to M_d.

Superelasticity occurs when a material is deformed above A_s, but still below M_d. In this range, martensite can be made stable with the application of stress, but becomes unstable again when the stress is removed. Fig. 2.9 shows a typical superelastic stress-strain curve. The upper plateau corresponds to the formation of martensite under applied stress while the lower plateau represents the reversion of the stress-induced martensite when the stress is released. Note that 9% strain is fully recovered during unloading, in what can be viewed as a mechanical shape memory effect. When stress-induced martensite is formed, usually only one variant of martensite is formed and the shape deformation of

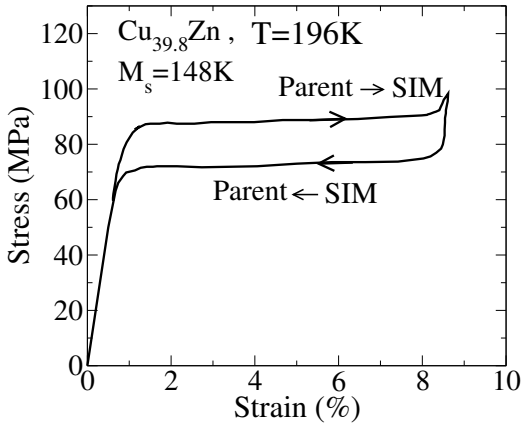

Figure 2.9: Stress-strain curve for a Cu-Zn shape memory alloy loaded above A_s and then unloaded shows distinct superelastic behavior [Due90]. Stress-induced martensite (SIM) is formed during unloading, which becomes unstable and disppears upon unloading.

that particular variant produces maximum elongation of the specimen along the tensile axis. Since only one variant is formed under stress, there is a shape change which is fully recovered upon release of the stress. This situation is unlike the case of thermal martensite, where because of self accommodation, there is no overall shape change accompanying to the formation of many variants of martensite.

2.6 Applications

The unusual properties of shape memory alloys mentioned above are being applied to a wide variety of applications in a number of different fields of electromechanics and surgery. The particular properties of NiTi alloys favour their greater use in biomedical applications. The material is extremely corrosion resistant, demonstrates excellent biocompatibility, can be fabricated into the very small sizes often required and has properties of elasticity and force delivery which are not possible other ways.

Increasing a volume of a device by direct contact or remote heat input has allowed the development of new techniques for keyhole or minimally invasive surgery. This includes instruments that have dynamic properties, such as miniature forceps, clamps and manipulators. SMA-based devices that can dilate, constrict, pull together, push apart and so on have enabled difficult or problematic tasks in surgery to become quite feasible.

In some applications, the shape memory component is designed to exert force over a considerable range of motion, often for many cycles [Kru87]. In electrical connector systems, the SMA component is used to force open a spring when the connector is heated. This allows force-free insertion or withdrawal of a circuit board in the connector. Upon cooling, the NiTi actuator becomes weaker and the spring easily deforms the actuator while it closes tightly on the circuit board and forms the connections. Based on the same principle, CuZnAl shape memory alloys have found several applications in this area. One such example is a fire safety valve, which incorporates a CuZnAl actuator designed to shut off toxic or flammable gas flow when fire occurs [Wal87].

It is possible to use only a part of the shape recovery to accurately position a mechanism by using only a selected portion of the recovery because the transformation occurs over a range of temperatures rather than at a single temperature. Devices have been developed [Hod88] in which a valve controls the rate of fluid flow by carefully heating a shape-memory alloy component just enough to close the valve the desired amount. Repeatable positioning within 0.25 mm is possible with this technique.

Although specific products that might use NiTi alloys in the future cannot be foretold, some directions are obvious. The cost of these alloys has slowly decreased as use has increased, so uses that require lower-cost alloys to be viable are being explored. Alloy development has yielded several ternary compositions with properties improved over those obtained with binary material, and alloys tailored to specific product needs are likely to multiply. Finally, the availability of small wire that is stable, is easily heated by a small electrical current, and gives a large repeatable stroke should lead to a new family of actuator devices. These devices can be inexpensive, are reliable for thousands of cycles, and are expected to move NiTi into the high-volume consumer marketplace.

Recent interest in the development of shape memory alloys has challenged the concept that the magnetic order can enhance the shape recovery in magnetic materials which undergo thermoelastic martensitic transformation. Some magnetic martensitic materials exhibit, beyond the conventional thermal shape memory effect, a shape recovery and large magnetic-field induced strains under a moderate applied magnetic field. They are known as magnetic shape memory materials. In these magnetic materials, the motion of the twin boundaries of the different martensite variants costs less energy than the reorientation of magnetic moment within a magnetic domain, inducing a change in the shape depending on the direction of the applied magnetic field [Suo04]. In contrary to the conventional memory materials where the martensitic transformation takes place in a non-magnetic phase, the structural changes in the magnetic shape memory materials occur in a long-range ordered magnetic phase. At the moment, the largest magnetic field induced deformations have been observed in Ni-Mn-Ga alloys close to the stoichiometric composition Ni_2MnGa, where strains up to 10% are obtained in the field of 1 T [Soz02]. This new class of smart materials will feature an increase in response speed of actuators. Typical response time of less than a millisecond are observed. Although, technological applications are not at hand on a large scale, a breakthrough in the coming years is expected.

Chapter 3

Ni_2MnAl a high-temperature shape memory alloy

This chapter reports on the preparation of polycristalline Ni_2MnAl alloys and their characterisation by means of differential scanning calorimetry. The effect of chemical composition and thermal treatements on the martensitic transition are discussed. Prior to the experimental results, we present first some basics on the phase diagram and the structure of Ni_2MnAl.

3.1 Ni_2MnAl phase diagram

Intermetallic alloys are currently the focus of considerable interest not only as structural but also as functional materials for various applications. The nickel aluminides of the Ni–Al systems with the bcc phase could be cited as specific examples of such materials; they are suitable as high temperature structural materials by virtue of their high thermal stability to undergo a thermoelastic martensitic transformation and exhibit the shape memory effect. It has been recently found that the addition of Mn to NiAl increases the M_s temperature of the thermoelastic martensitic transformation B2 to 2M. This has opened up possibility of producing high-temperature shape memory alloys that can be operated between 370 K and 970 K [Kai92,Kai95,Kai96].

Figure 3.1 shows the binary phase diagrams constituting the Ni–Mn–Al system [Mas90] . From the phase diagram of the Mn–Al system [Liu96], it can be seen that the disordered bcc phase (δ-Mn) of the Mn–Al system extends over a wide range of composition and temperature. This should have consequences on the phase stability of the bcc phase and on the ordering reaction between A2 and B2 phases. Recently, the phase equlibria and ordering reactions in the composition range up to 50 at.% Al have been investigated in the Ni-Mn-Al system in the interval 1120-1470 K mainly by the diffusion couple method [Kai98].

The results pertaining the phase equlibria in the Ni–Mn–Al system are plotted in Fig. 3.1. It shows that the bcc (β and δ-Mn) single-phase regions widen with increasing Mn content and increasing temperature.

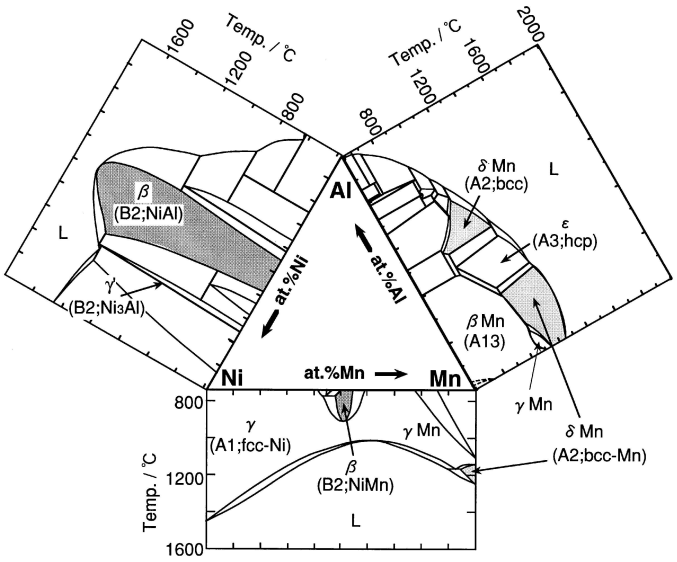

Figure 3.1: Taken from [Mas90]: Phase diagrams of the binary systems consituting the Ni-Mn-Al system (up). Isothermal section diagrams at 850 °C, 1000 °C and 1100 °C in the Ni-Mn-Al systems (right).

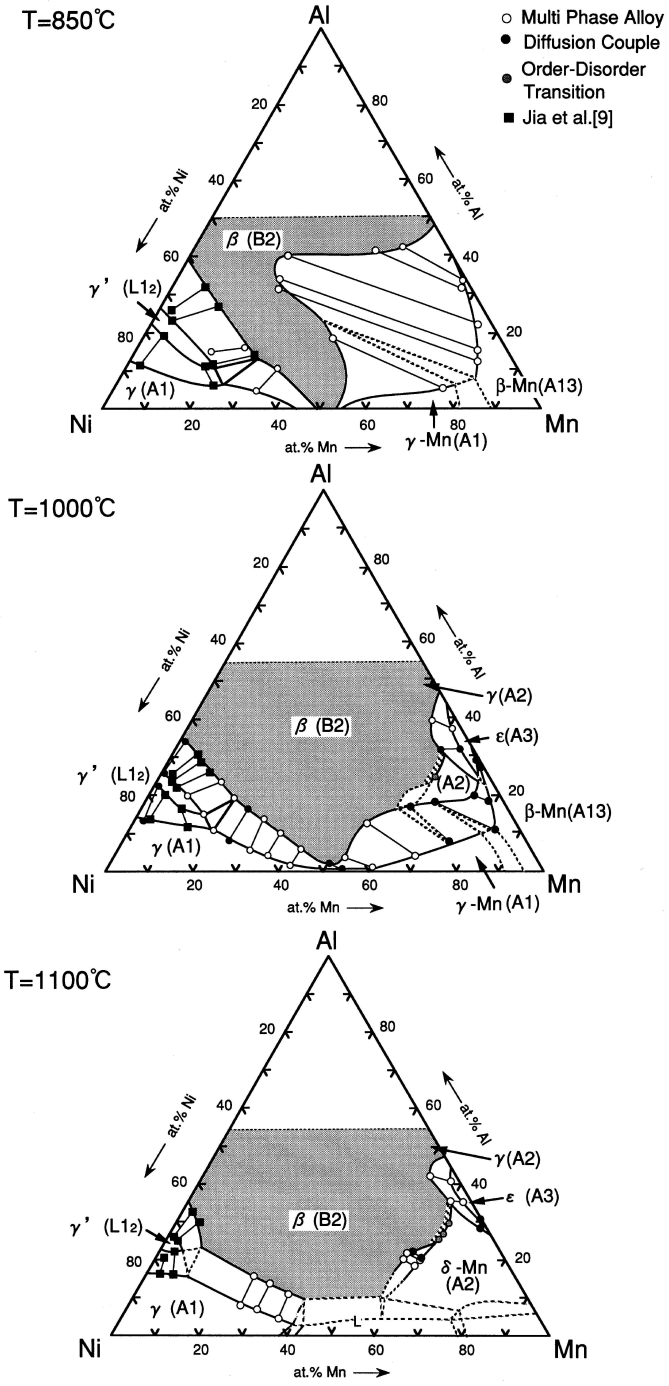

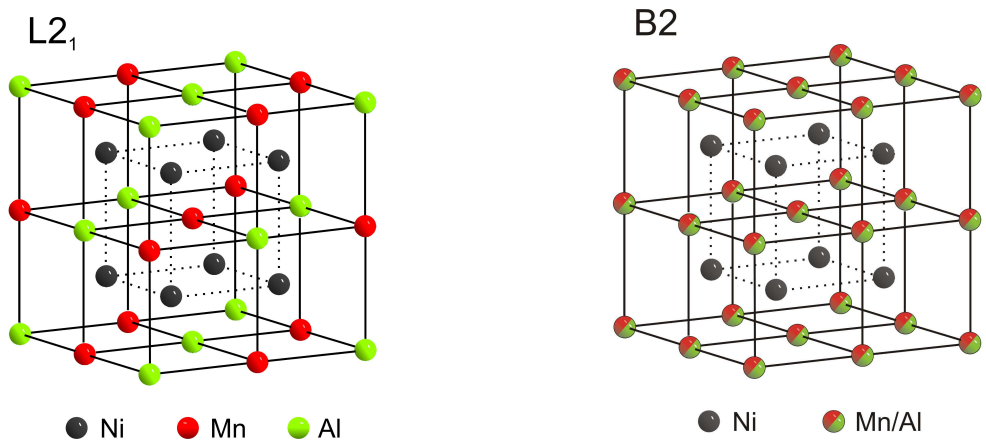

Figure 3.2: Two types of atomic ordering in ternary Ni_2MnAl. The Heusler $L2_1$ structure and the B2 structure where Al and Mn sites become equivalent.

It is interesting to note that the $\beta + \beta$-Mn two-phase region has an unusual shape in the isothermal phase diagram at 850 °C shown in Fig. 3.1. The solubility curve of the β phase of the $\beta + \beta$-Mn equilibrium is made up of a line that starts from near the MnAl composition, runs almost parallel to the line from MnAl to NiAl up to a point left of the center, turns by 120° and runs parallel to the line from NiAl to MnNi ending up at a composition near MnNi, thus describing a very lopsided two $\beta + \beta$-Mn phase field. The reason for such an odd shape is not immediately obvious, but it may be related to the fact that a metastable β(B2)+δ-Mn (A2) miscibility gap island may be hidden in the wide $\beta + \beta$-Mn two-phase region.

Among the Heusler alloys, Ni_2MnGa and Ni_2MnAl undergo martensitic transformations at compositions around stoichiometry, with the transformation temperature M_s varying rapidly with small changes in the concentration of the constituents [Cher95, Kai96, Mor96]. Ni_2MnGa is ferromagnetic in both the austenite $L2_1$ (see Fig. 3.2) and the martensite phase [Cher99], and it has been demonstrated that in the martensitic phase, strains on the order of 10% can be induced in single crystals by applying an external magnetic field of about 1 T leading to the magnetic shape memory effect [Soz02]. Obviously, this property provides a technological value for Ni_2MnGa, and a great deal of effort has been invested in research to understand the properties of the martensitic phase in this alloy [Man00, Cas99]. Stoichiometric Ni_2MnAl is structurally stable down to the lowest temperature, but martensitic transformations occur in the slightly off-stoichiometric alloys. Their mechanical properties are more favorable than those of the relatively brittle Ni_2MnGa. Ni_2MnAl could be used as an alternative material if its magnetic shape memory properties are as favorable as those of Ni_2MnGa. The pure B2 phase in Ni_2MnAl (see Fig. 3.2) can be retained by annealing at 950 K and a subsequent quenching to room temperature. On the other hand, it appears that it is difficult to produce a single $L2_1$ phase, since the B2-$L2_1$ transformation in this compound requires long-time annealing at about 650 K where the diffusion is relatively slow as compared to the stabilisation temperature of the $L2_1$ phase. The magnetic ordering in the retained metastable B2 phase of Ni_2MnAl is conical antiferromagnetic [Zie75]. In the $L2_1$ phase, there is some indirect

evidence based on calorimetric measurements that the magnetic ordering is ferromagnetic [Gej99]. Recently, Acet *et al.* have showed using X-ray and magnetisation measurements that although a single B2 phase can be stabilised at room temperature, a single $L2_1$ phase is not readily stabilised, but rather a mixed $L2_1$+B2 state occurs. The mixed state incorporates ferromagnetic and antiferromagnetic parts for which close-lying Curie and Néel temperatures can be identified from magnetisation [Ace02]. It has been possible to induce a strain on a Ni_2MnAl single crystal specimen by applying a magnetic field. The strain has, however, not exceeded 0.2% [Fuj00]. This appears to be a problem of not having a single $L2_1$ austenite phase in the sample. If it were possible to increase the amount of $L2_1$ in an $L2_1$-B2 mixed phase, the strain in the martensitic state would also increase. This is a point that certainly requires further investigation. The B2 to $L2_1$ transformation in Ni_2MnAl occurs around 700 K, temperature where diffusion kinetics in solids are slow. This enables the high temperature B2 phase to be readily retained at room temperature as a metastable state rather than the thermodynamically more favorable $L2_1$ phase. Annealing just below the temperature of the transformation boundary does not produce a single $L2_1$ phase in Ni_2MnAl in a period of 30 days, because either this time is too short or metastable equilibrium between the B2 and the $L2_1$ phase is reached. The amount of the $L2_1$ phase can certainly depend on the grain size of the sample. However, annealing of a single crystal in the same conditions lead to an $L2_1$ ordering state not exceeding 10%.

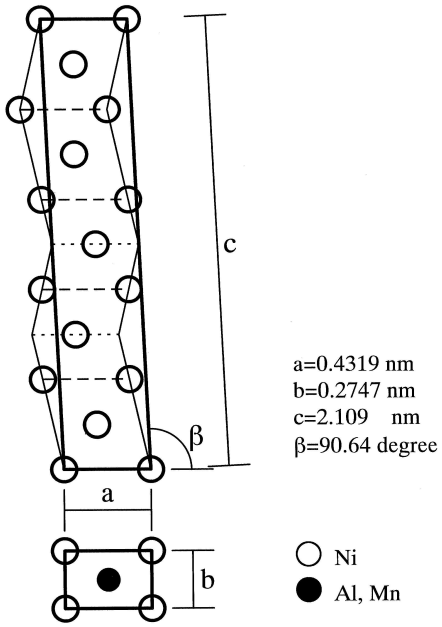

Figure 3.3: Example of 5R martensite structure with the corresponding lattice parameters.

Kainuma et al. have investigated the crystalline structure of martensite $Ni_{50}Mn_{50-x}Al_x$ by means of electron microscopy observations and differential scanning calorimetry. These alloys exhibit long period stacking order structures. $5R(10M,(3\overline{2})_3)$ martensite structure was found for $19 \leq x \leq 20$. For $x \leq 17$ the martensite was invariably $7R(14M,(5\overline{2}))$. For $17 \leq x \leq 19$, various martensite where found, and the situation was in between the above two cases. Based on these results a metastable phase diagram of $Ni_{50}Mn_{50-x}Al_x$ system depicted on Fig. 3.4 was proposed [Mor96]. Other studies of shape memory alloys have

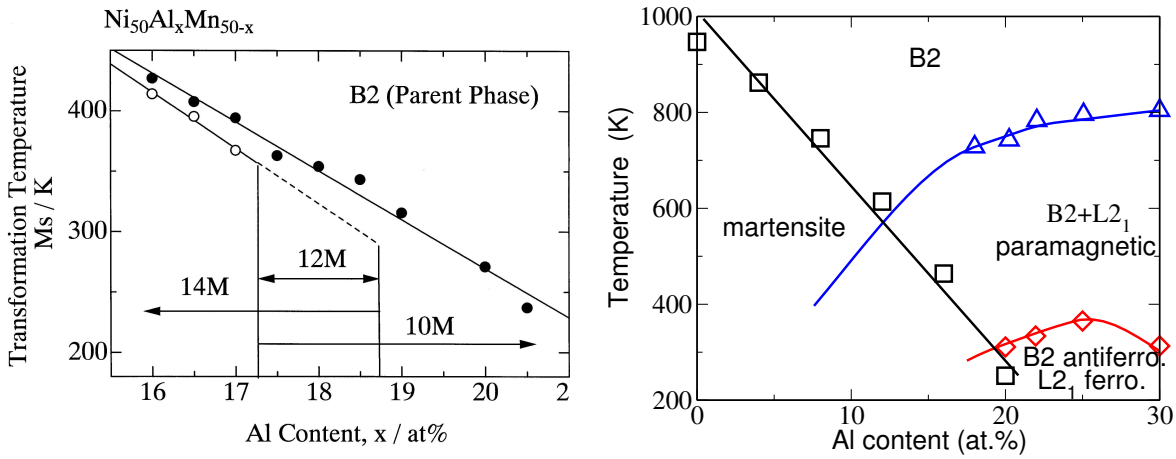

Figure 3.4: Proposed phase diagrams of $Ni_{50}Mn_{50-x}Al_x$ alloys from [Mor96] (left) and [Kai00] (right) showing the different ordering and magnetic states.

already indicated that the martensitic transformation temperature is highly sensitive to composition and can be observed in a wide range of temperature range.

3.2 Sample synthesis

Polycristalline Ni_2MnAl samples have been produced using an arc-melting furnace (Fig. 3.5). In an arc-melting technique, the charge is melted by direct contact with an electric arc. The arc is produced by striking current from a charged electrode to the metal (the neutral point), through the metal, and drawn to an oppositely charged electrode which is made of water-cooled copper plate. At the start of the arc-melting process the electrodes and roof are raised and swung to one side and a charge made of appropriate amount of pure materials is dropped into the furnace. The roof is sealed and the chamber is evacuated down to 10^{-5} mbar and filled with an inert 6N Argon gas. The procedure is repeated three times, then the electrodes are lowered and an arc struck. The arc contacts the scrap charge and the metal is melted.

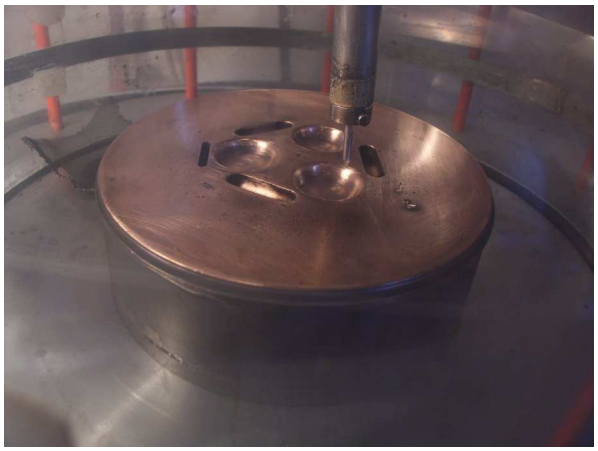

Figure 3.5: Arc-melting chamber showing the W anode used to generate the arc (the needle pointing down) and the Cu cathode with provisions to keep the elements. Different geometries of these slots are used to make samples with different shapes. The cathode and the anode are water cooled.

Polycrystalline Ni_2MnAl alloys with different compositions have been prepared from 5N7 Ni, 4N Al and 4N Mn pure materials. To avoid any source of contamination and ensure a high purity, the starting materials have been etched prior to metling. Nickel has been etched by a mixture of 1:1 HF+HNO_3, Al by a 1:1 H_2O+HF and Mn by 10% HNO_3 solved in Ethanol. Special care has been taken to etch the Mn which is easily oxidable just before to the arc-melting procedure. Longer air exposures result in a yellowish oxide layer on the Mn-plates. It turned out after the first tries that the Mn-plates were cracking at the contact with the arc making a composition control of the samples quite difficult. The reason might be an internal stress cumulated during the casting process of the pure Mn. To avoid this problem a first melt of pure Mn-plates was performed after which the plates were shaped in bullets and resulted in much less brittleness at the contact with the arc. A second difficulty which had to be overcome is the high evaporation of Mn because of its high vapor pressure in comparison to Ni and Al. To avoid Mn loss during the sample preparation, ternary Ni_2MnAl alloys have been prepared in two steps: a first melting of an appropriate amount of Ni and Mn is performed for which the melting point is around 1290 K at the eutectic composition in comparison to 1720 K of stoichiometric Ni_2MnAl. The weight loss is then determined and the appropriate amount of Mn and Al is added and melted with the NiMn charge. This procedure has the advantage of minimising the Mn loss by evaporation. To ensure homogenous atomic distribution, the samples have been turned upside down and remelted at least 4 times.

The disadvantage of an arc-melting technique lies in the relatively small amount of final material. Usually 5-10 g only are possible to prepare in a single run. This is inconvenient when a large amount of material is needed. In this case, several runs are necessary and the whole procedure is very time consuming.

Three sets of Ni_2MnAl alloys have been prepared, each of a fixed composition in Ni, Al or Mn. In total over 20 polycristalline samples have been synthesised. To check for the homogeneity of the samples, a first visual inspection is performed after breaking the samples and looking to the inner parts. Later, a second test is performed by measuring DSC charts of different pieces of the same sample.

3.3 Differential scanning calorimetry

Differential scanning calorimetry (DSC) is a technique for measuring the energy necessary to establish a nearly zero temperature difference between a substance and an inert reference material, as the two specimens are subjected to identical temperature regimes in an environment heated or cooled at a controlled rate. There are two types of DSC systems in common use. In power-compensation DSC the temperatures of the sample and reference are controlled independently using separate, identical furnaces. The temperatures of the sample and reference are made identical by varying the power input to the two furnaces; the energy required to do this is a measure of the enthalpy or heat capacity changes in the sample relative to the reference. In heat-flux DSC, the sample and reference are connected by a low-resistance heat-flow path (a metal disc). The assembly is enclosed in a single

furnace (Fig. 3.6). Enthalpy or heat capacity changes in the sample cause a difference in its temperature relative to the reference; the resulting heat-flow is small compared with that in differential thermal analysis because the sample and reference are in good thermal contact. The temperature difference is recorded and related to enthalpy change in the sample using calibration experiments.

The difference in energy required to maintain them at a nearly identical temperature is provided by the heat changes in the sample. Any excess energy is conducted between the sample and reference through the connecting metallic disc. The thermocouples are not embedded in either of the specimens; the small temperature difference that may develop between the sample and the inert reference (usually an empty sample pan and lid) is proportional to the heat-flow between the two. The fact that the temperature difference is small is important to ensure that both containers are exposed to essentially the same temperature program. The main assembly of the DSC cell is enclosed in a cylindrical, silver heating block, which dissipates heat to the specimens via a constantan disc which is attached to the silver block. The disc has two platforms on which the sample and reference pans are placed. A chromel disc and connecting wire are attached to the underside of each platform, and the resulting chromel-constantan thermocouples are used to determine the differential temperatures of interest. Alumel wires attached to the chromel discs provide the chromel-alumel junctions for independently measuring the sample and reference temperature. A separate thermocouple embedded in the silver block serves a temperature controller for the programmed heating cycle. An inert gas can be passed through the cell at a constant flow-rate. The thermal resistances of the system vary with temperature, but the instrument can be used in the calibrated mode, where the amplification is automatically varied with temperature to give a nearly constant calorimetric sensitivity.

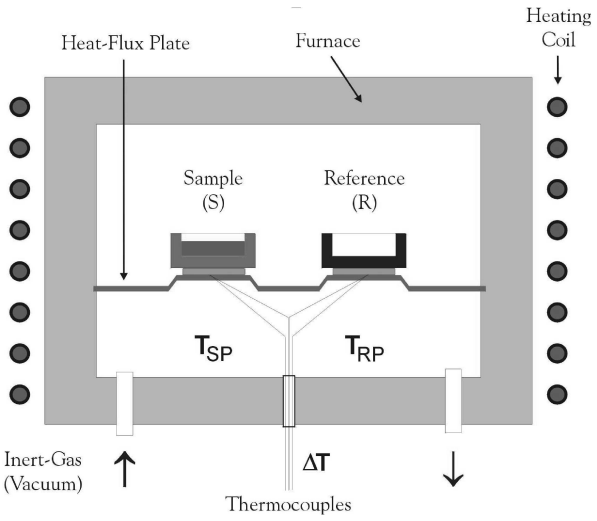

Figure 3.6: Main components of a typical heat-flux DSC setup.

Thermal analysis techniques such as DSC have the advantage that only a small amount of material is necessary. This ensures uniform temperature distribution and high resolution. The sample can be encapsulated in an inert atmosphere to prevent oxidation, and low heating rates lead to higher accuracies. The reproducibility of the transition temperature can be checked by heating and cooling through the critical temperature range. During a first-order transformation, a latent heat is evolved, and the transformation obeys the classical Clausius-Clapeyron equation. Second-order transitions do not have accompanying latent heats, but like first-order changes, can be detected by abrupt variations in compressibility, heat capacity, thermal expansion coefficients and the like. These variations reveal phase transformations using thermal analysis techniques.

Greater care is needed when studying solid-solid transitions where the enthalpy changes are much smaller than those associated with melting. Stored energy in the form of elastic strains and defects can contribute to the energy balance, so that the physical state of the initial solid, and the final state of the product, become important. This stored energy reduces the observed enthalpy change.

3.4 Martensitic transition in Ni_2MnAl alloys

To retain the B2 atomic ordering at low temperatures and ensure for a good homogeneity, the as-prepared samples have been solution annealed in fused quartz tubes with Argon atmosphere during 72h, followed by quenching in water. To perform the calorimetric measurements, small pieces of about $1\times3\times3$ mm^3 have been cut by spark erosion. The weight of the pieces ranges from 15-50 mg. The calorimetric measurements were performed by a heat-flux differential scanning calorimeter from Scientific Rheometrics. The measurements were carried out by heating up and cooling down at a thermal constant rate of 20 K/mn. A liquid nitrogen cooling accessory was used when necessary. In the following, we present the results of the calorimetric measurements. The effect of chemical composition and the heat-treatment on the martensitic transition in Ni_2MnAl are discussed.

Figure 3.7 shows two typical DSC charts recorded upon heating up and cooling down of two samples $Ni_{50}Mn_{45}Al_5$ and $Ni_{50}Mn_{40}Al_{10}$ solution annealed and subsequently water quenched. An endothermic peak, related to the transformation from martensite to austenite is observed while heating up. The transformation from austenite to martensite is revealed by an opposite peak recorded on cooling down. It can be seen that there is only one endothermic or exothermic peak in the heating or cooling DSC curves, respectively, indicating that only one phase transformation appeared in each run. A shift in transformation temperatures, related to the hysteresis of the transformation is seen. There are four critical martensitic transition temperatures in the forward and backward martensitic transition. The martensitic start (M_s) and finish temperature (M_f), the austenite start temperature (A_s) and finish temperature (A_f). These temperatures are defined as being the crossing of the baseline with the peak tangents as shown in Fig. 2.2. Among these temperatures, A_f is referred to as the switching temperature and possesses the largest engineering meaning [Ots99] whereas M_s reveals the phonon-triggered phase transition

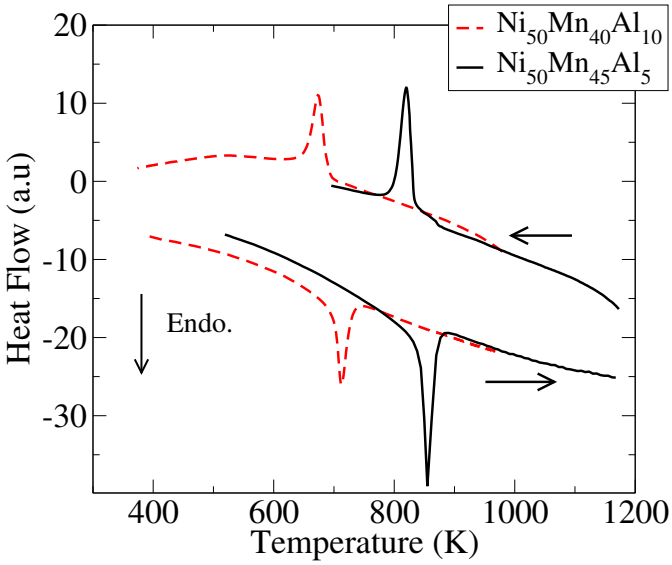

Figure 3.7: Typical DSC charts measured in as-quenched $Ni_{50}Mn_{45}Al_5$ (M_s=833 K) and $Ni_{50}Mn_{40}Al_{10}$ (M_s=695 K) samples upon heating up and cooling down at a constant rate of 20 K/min. Note that 5 at.% difference in Al. content induces a shift of 45 K in M_s.

and deserves much more interest from a fundamental point of view.

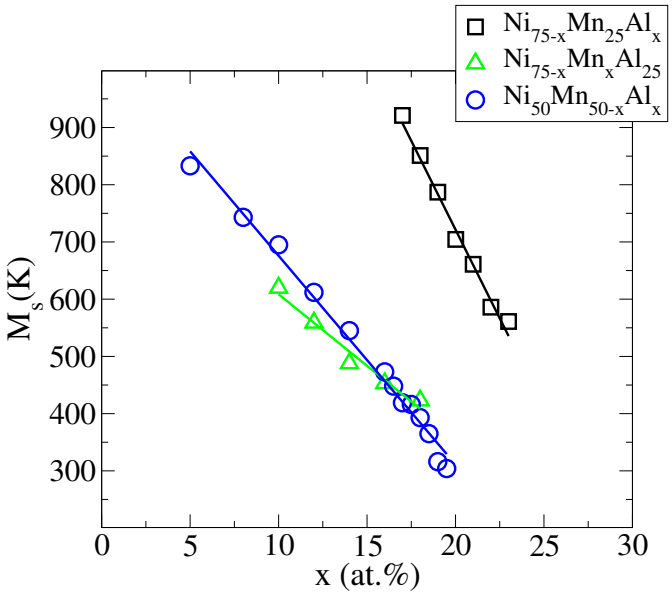

Figure 3.8: Martensitic start temperature measured on as-quenched $Ni_{75-x}Mn_{25}Al_x$, $Ni_{75-x}Mn_xAl_{25}$ and $Ni_{50}Mn_{50-x}Al_x$ samples.

All measured DSC charts on the three set of quenched samples are summarised in Table 3.1. The martensite start temperatures M_s obtained in different samples with fixed Ni, Al and Mn respectively are depicted on Fig. 3.8 as function of the chemical compositions. Within the limited composition range considered here, the impacts of individual elements on M_s can be described based on Fig. 3.8 as follows:
(1) increased Ni content increases M_s whether it replaces Mn or Al, (2) increased Mn content decreases M_s if Mn replaces Ni, while M_s will be increased if Mn replaces Al at

Table 3.1: Nominal chemical compositions and martensitic transformation temperatures in studied Ni_2MnAl alloys

	Content (at.%)			M_s	M_f	A_s	A_f	e/a
Alloy	Ni	Al	Mn	(K)	(K)	(K)	(K)	
1	50	5	45	833	784	828	870	8.30
2	50	8	42	743	701	743	783	8.18
3	50	10	40	695	647	687	730	8.10
4	50	12	38	612	572	612	650	8.02
5	50	14	36	545	498	542	584	7.94
6	50	16	34	473	452	483	502	7.86
7	50	16.5	33.5	448	406	452	494	7.84
8	50	17	33	419	395	415	432	7.82
9	50	17.5	32.5	416	388	410	453	7.80
10	50	18	32	393	371	382	401	7.78
11	50	18.5	31.5	365	327	345	378	7.76
12	50	19	31	316	294	302	322	7.74
13	50	19.5	30.5	304	283	308	312	7.72
14	58	17	25	648	522	553	578	8.06
15	57	18	25	578	549	570	584	7.99
16	56	19	25	514	492	518	527	7.92
17	55	20	25	433	407	429	458	7.85
18	54	21	25	388	343	372	398	7.78
19	53	22	25	313	292	319	324	7.71
20	52	23	25	288	260	290	310	7.64
21	35	25	10	620	592	612	642	7.95
22	63	25	12	559	538	546	572	7.89
23	61	25	14	488	462	475	502	7.83
24	59	25	16	453	425	438	472	7.77
25	57	25	18	423	392	409	442	7.71

constant Ni, and (3) increased Al content will lower M_s whether it replaces Ni or Mn. Aluminium seems to have the strongest influence on M_s. The reason is that its e/a ratio differs most strongly from the average value of Ni_2MnAl. Aluminium is thus worthy of being treated with caution in processing alloys. These conclusions agree well with the available results about the composition dependence of transformation temperature in Ni_2MnGa [Cher95, Vas99].

Besides the nominal compositions, the average number of valence electrons per atom ratio was used to describe the electronic structure dependence of M_s. The relationship between martensitic transformation temperature and the valence electrons per atom ratio of measured Ni_2MnAl samples is presented in Fig. 3.9. Here, it is assumed that the number of valence electrons per atom for Ni, Mn, and Al atoms are 10 ($3d^9 4s$), 7 ($3d^5 4s^2$) and 3($4s^2 4p^1$), respectively. A linear dependence of M_s with e/a is observed. The data

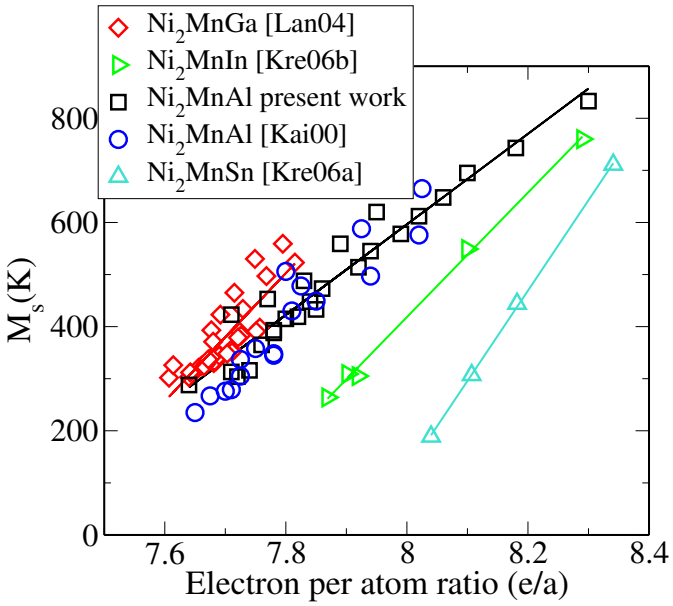

Figure 3.9: M_s *versus* the average number of valence electrons per atom (e/a) in different Ni-based systems. The linear regression fits to the data are shown in solid lines.

are compared to other typical Heusler shape memory alloys yielding different slopes for different systems. The lattice instability in Ni_2MnAl occurs at electron atom ratio slightly higher than these of Ni_2MnGa [Lan04]. Furthermore, alloying of Ni_2MnAl with $3d$ transition elements can also considerably increase the martensitic transformation temperature [Zhi03]. Early studies of composition dependence of the martensitic transition in Heusler alloys already showed that there is a clear relation between M_s and the electron concentration e/a, and that M_s increases with increasing e/a [Cher95]. These results imply that the number of valence electrons can be considered as the primary driving force for the occurrence of structural instabilities. First-principle calculations, evidenced by lattice dynamics measurements performed in the frame of this work, support this idea.

Based on the linear regression: $M_s[K] = 870(e/a) - 6356$. Together with the linear composition dependence for M_s presented above, the martensitic transformation temperature can be evaluated as $M_s[K] = 2344 - 60.9x_{Al} - 26.1x_{Mn}$, where x_{Al} and x_{Mn} are the atomic percent numbers for Al and Mn, respectively.

The effect of aging in the austenitic (Fig. 3.10) and martensitic (Fig. 3.11) state on the martensitic transformation has been investigated on a $Ni_{58}Mn_{25}Al_{17}$ sample. The M_s transformation temperature in an as-quenched sample was found to be 702 K. The aging in the austenitic state was performed at a temperature of 723 K. DSC charts of the aged samples as measured upon cooling immediately after each thermal treatment are shown in Fig. 3.10. To ensure for a good homogeneity, all pieces have been cut from a unique charge and have been used only one time. The DSC measurements evidence that aging in the austenitic state results in a marked change of the martensitic start temperature. As evident from Fig. 3.12, in the early stage of aging, the change in M_s is relatively small but after 3h aging M_s starts to decrease drastically with aging time and for time $t \geq 7h$ it is equal to 668 K, 34 K lower than that observed in as-quenched sample before aging.

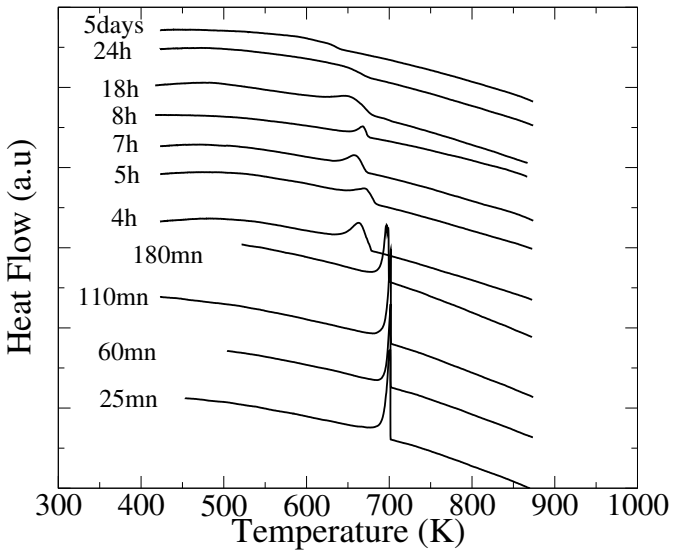

Figure 3.10: Influence of aging performed in the austenitic state at 723 K on the transformation behaviour of water-quenched $Ni_{58}Mn_{25}Al_{17}$. DSC charts are taking upon cooling from the austenitic phase.

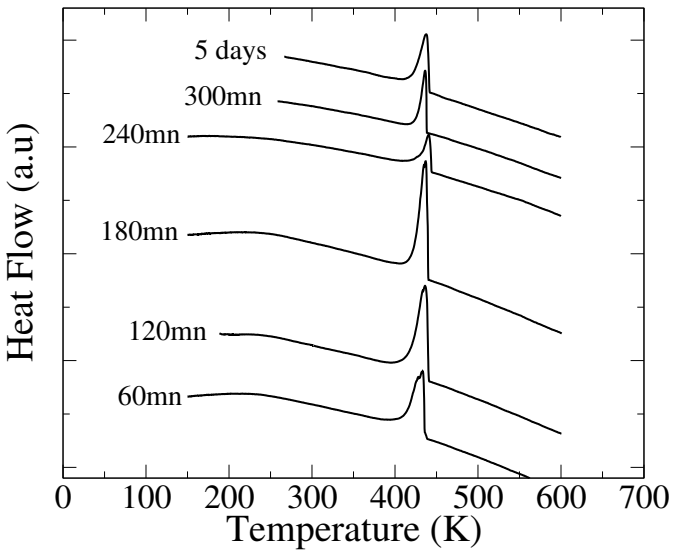

Figure 3.11: Influence of aging performed in the martensitic state at 625 K on the transformation behaviour of water-quenched $Ni_{58}Mn_{25}Al_{17}$.

There are several scenarios, which can explain the decrease in M_s after aging in the austenitic state. Considering that the samples after water quenching have a high concentration of vacancies, which is enhanced by the significant deviation of the studied composition from stoichiometry, the high density of vacancies can actually produce a permanent strain in the samples due to static atomic displacements. In this sense, the high density of vacancies is equivalent to an internal stress, leading to an increase in the martensitic start temperature. Ageing of the samples above the martensitic transformation followed by a subsequent furnace cooling results in a drastic decrease in the density of vacancies. This process is equivalent to the release of the internal stress, decreasing the martensitic

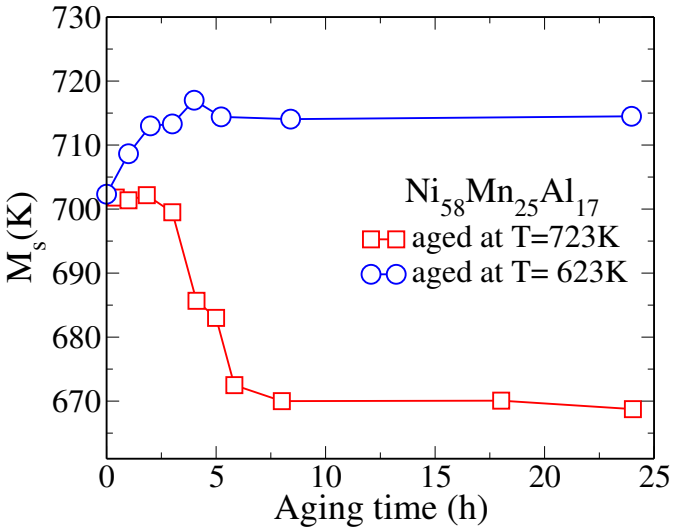

Figure 3.12: M_s *versus* aging time of $Ni_{58}Mn_{25}Al_{17}$ annealed in the austenitic state at 723 K (squares) and in the martensitic state at 625 K (circles).

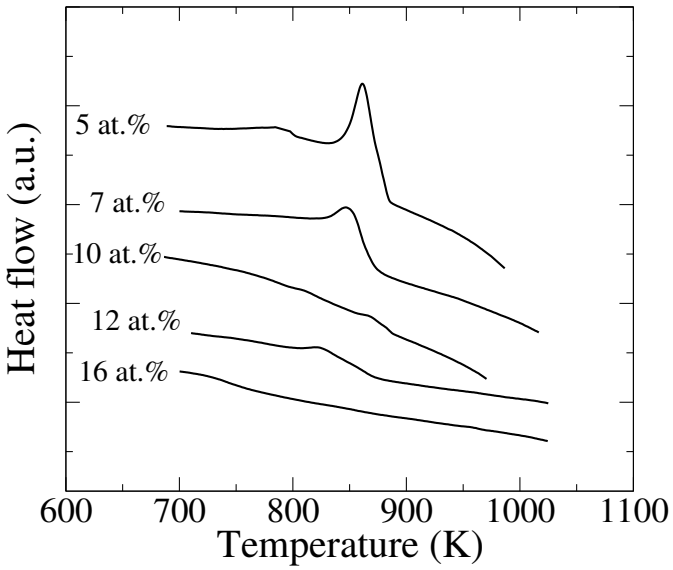

Figure 3.13: Influence of Al content on the transformation behaviour of as-prepared $Ni_{50}Mn_{50-x}Al_x$. The reported compositions of the figure refer to the Al. content.

transformation temperature. Besides this possibility, the decrease in M_s can be explained by aging-induced changes in the thermodynamical properties of the martensitic phase in such a way that the crystal structure of martensite forming upon martensitic transformation in the aged samples differs from that in the as-quenched samples. Formation of the austenite-aging martensite having an other crystalline structure can result in the alteration of the characteristic temperatures and the temperature hysteresis of the martensitic transformation.

An other striking feature of the aging effect is the decrease of the transformation heat with aging time. The DSC chart show well pronounced peaks in the early stages of aging and become smoother at higher aging times. The martensitic transformation are hardly seen

at very long aging times where the DSC curves show a tiny kink around M_s. A possible explanation is the relatively high aging rate which can induce precipitation of a second phase within the B2 austenite. In fact, at higher aging time, there is no significant change in M_s but only the area under the DSC peaks become smaller indicating a decrease in the volume fraction of the transforming B2 phase. Indeed, as shown in Fig. 3.13, as-prepared samples with such a high Al content did not show a martensitic transformation because of the presence of Al-rich precipitates unless they are solution annealed and subsequently water-quenched.

Ageing in the martensitic state performed at 625 K, revealed a typical influence of aging of a shape memory material in the martensitic state, *i.e.* an increase in the martensitic transformation temperature due to the thermal stabilisation of martensite (Fig. 3.12).

Chapter 4

Single crystal growth

This chapter surveys the main part of this work: the single crystal growth. The first part is devoted to some basics and to the different techniques used to grow Ni_2MnAl single crystals. A lot of effort has been put in the challenging task of growing good quality NiTi single crystals. The growth was however not successful. The related experimental procedure is also highlighted. The last part of this chapter deals with the chemical analysis and with the characterisation of the grown Ni_2MnAl single crystals.

4.1 General considerations

The crystal growth can be called, in a wide sense, the science and technology of controlling phase transitions that lead to single crystalline solids. The optimum growth method can be described as the sequence of preparative steps (preparation of starting material, growth and after-treatment of crystal) that lead to certain compositional and structural properties of a real crystal which are desired for a specific experiment or application. A thorough knowledge of the thermodynamics of phase equlibria and skill in deducing from phase diagrams their consequences for crystal growth are among the key to efficient work in this area.

Growth from a melt is the oldest established method of growth. The basic requirements of the method are very simple but for some purposes the presence of a crucible presents experimental difficulties. One needs a wealth of information to anticipate the reaction of the material with its environment during the preparation. Questions must be answered include: How does the material interact with containers, what are the consequences of fluctuations in environmental parameters *e.g.* temperature, stress ? The container-related difficulties are most easily overcome by the use of the floating-zone technique. However, a prerequisite for a successful growth using this technique is high enough surface tension of the melt. Surface tension is the principle force supporting a molten zone. Cohesion between solid and liquid and levitation due to RF coil fields are usually negligible. This turned out to a determinant factor in the case of Ni_2MnAl. Floating-zone technique has been used to grow Ni_2MnAl single crystals. The rod diameter and growth speed have been varied, however, the low surface tension made extremely difficult an accurate control of the molten charge and hindered, by the way, a successful growth.

4.2 Bridgman method

The basic concept of the Bridgman method is to start the growth process with the whole charge molten and then to solidify from one end, where there can, if necessary, be a seed crystal. The Bridgman growth method is basically a controlled freezing process taking place under liquid-solid equilibrium conditions. The growth also takes place under a temperature gradient, and the mechanism is to produce a single nucleus from which a single crystal will propagate and grow. This is achieved by allowing the solid-liquid interface to move slowly until the whole molten charge is solidified. If a seed crystal is used it is usually necessary to be able to see that it has partially melted, which is an essential condition for satisfactory growth. Visibility can be achieved by using a transparent furnace or one with a window to see the surface of the melt. If however an opaque crucible is used then it is much easier not to use a seed. In this case, crystals with random orientations may have to be accepted unless there is a very strongly preferred growth direction. In order to increase the yield of single crystal it is sometimes desirable to use crucibles of a particular form. Generally crucibles with a neck at the bottom can help to decrease the possibility of more than one crystal growing in the major part of the crucible. In this case, it is necessary to use a crucible which can be split to remove the crystal, or to destroy the crucible at the end of the run.

Compared to other growth methods, the Bridgman method is considered to be a rather simple crystal growth method, but several limitations still exist. The Bridgman method is not very suitable to material systems having components with high vapour pressure, and materials exhibiting destructive solid-solid phase transformations which will compromise the crystalline quality on cooling the crystal at the end of the growth run. Besides, the permanent contact of the liquid-solid interface with the crucible, in some cases, substantially hinders a successful crystal growth.

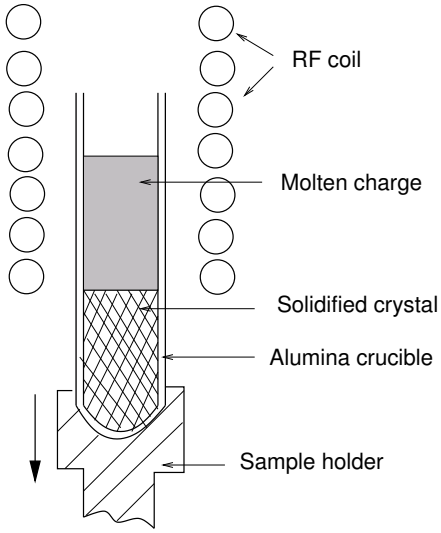

Figure 4.1: Scheme of the experimental setup used to grow Ni_2MnAl single crystals using the Bridgman method.

In order to grow Ni_2MnAl single crystals, a premelting of a polycrystalline samples with the desired composition has been performed following the procedure reported in section 3.2. Several pieces, each of roughly 10-12 g, have been melted together in a suitable copper plate and shaped in rods with different diameters. Our arc melting furnace lacks a mould, a grinding of the starting rods was necessary to get regularly shaped rods prior to the single crystal growth run. First tries with graphite crucible turned out to be unsuccessful because of the high reactivity with the samples. A suitable crucible was found to be Alumina (Al_2O_3) with a density of 3.7–3.95 g/cm^3 and a mean grain size of 10μm. The crucibles were purchased from FRIATEC. Different tube diameters namely, 6 and 8 mm have been used. The melting of the charge was ensured by using RF coils with different designs. Both high and low gradient coils have been used. The starting rod was placed into the Alumina crucible and put into the center of the coil. To avoid the cracking of the Alumina crucible, the charge was heated slowly up to 100 K above the melting point (1720 K). To ensure for a good homogeneity, the temperature was maintained for about 20 mn, then the Alumina tube was moved downwards at constant speed. Speeds from 10 down to 1 mm/h have been tried. A scheme of the experimental set up used to grow Ni_2MnAl single crystals is shown in Fig. 4.1

The final rods are then cut along the growth direction, mechanically polished and etched. Optical micrographs revealed the presence of several grains with different orientations. The average grain size was 8-10 mm^3. Only a polishing of the inner part of the Alumina crucible using a diamond paste with 5μm grain size lead to typical grain size of 10-15 mm along the growth direction. Nevertheless, the grain did not extend over the whole cross-section of the rod.

4.3 Czochralski method

The Czochralski method consists in pulling the crystal from the melt. It is in many ways the most satisfactory method of growing crystals with a real scope for producing large dislocation-free single crystals. This is because the solid-liquid interface is no longer in contact with a crucible and the radial temperature gradients can be kept small by a suitable design of the crucible system. However, it has the disadvantage that a crucible is still present.

The material to be grown is initially melted in a suitable crucible. A seed crystal is lowered into the liquid. The temperature of the melt is adjusted so that a portion of the seed melts and the temperature is then slowly lowered until the seed crystal starts to grow. The seed crystal is then slowly raised. The diameter of the growing crystal can be controlled by varying the melt temperature and the pulling speed. An other inconvenience of the Czochralski method lies in the relative large amount of material necessary for a run. Usually starting charges of 150-200 g are needed.

Polycrystalline Ni_2MnAl samples with a weight of 10-15 g have been prepared in the arc melting furnace using the procedure explained in section 3.2. The individual charges are then chemically etched, weighted and brought together in an Alumina container. To ensure a good heat transfer, the Alumina crucible is put into an outer graphite pan. The

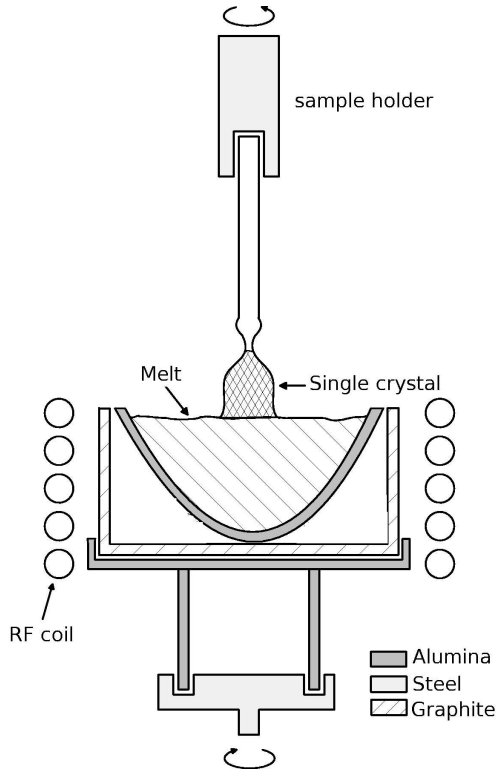

Figure 4.2: Scheme of the experimental setup used to grow Ni_2MnAl single crystals using the Czochralski method.

whole is mounted on a rotating axes made of steel. A scheme of the experimental set up used to grow Ni_2MnAl single crystals is shown in Fig. 4.2. In absence of a crystal seed, a polycrystalline rods of 5 mm in diameter and 40 mm in length having the same composition as the charge was used. The polycrystalline seed is held in a chuck attached to a shaft which is raised and rotated by a mechanical system. To ensure for a good homogeneity and avoid any temperature or concentration gradient in the melt, both seed and molten charge have been rotated in opposite directions at a rate of about 5 RPM. The molten charge is contained in Alumina crucible which is heated by a RF field from the coil. After keeping the molten charge at 100 K above the melting point for about 10mn, the polycrystalline seed is lowered until it catches the liquid charge and raised again at a constant speed. In the early stage of the growth run, a temperature and a speed control are used to create a neck in the pulled rod. The neck is made with the purpose of encouraging a single grain growth. Even if several crystals are nucleated at the start, there is high probability of only one or two growing through the neck. Due to the low surface tension of the Ni_2MnAl and considering the manual power and speed control, a lot of training and sometimes several tries were necessary for getting a relevant neck.

Strictly speaking, a prerequisite for a successful growth is that the surface of the melt should be free of foreign particles and films. This implies that the surface must be protected from dust and flakes of material condensed on the side and top of the growth chamber. This has been done by carefully cleaning the chamber prior to each run. After sealing, the chamber was pumped down to 10^{-5}mbar and filled with a 5N Argon gas at a slightly overpressure. Even so, an oxide layer inherent to the Mn has been systematically observed and covered the molten charge. The behaviour of this oxide layer during the growth was determinant. In some cases, it was just a question of time that the oxide layer

partially vanishes leaving the solid-liquid interface free after 10-15 h. In other cases, the oxide layer remained in a partial or total contact of the liquid solid interface hindering a successful growth.

It turned out that very low pulling speed, typically of 2-3 mm/h are necessary. A single whole run lasted two to three days. Typical relative differences of 8 to 10% in the weight of the starting material and the final pulled rods have been observed meaning a significant deviation from the nominal compositions. Besides, the same charge was used several times during repetitive runs.

Two large single crystals with different compositions have been successfully grown using the Czochralski technique (Fig. 4.3). Their orientation and characterisation are the topic of the following section.

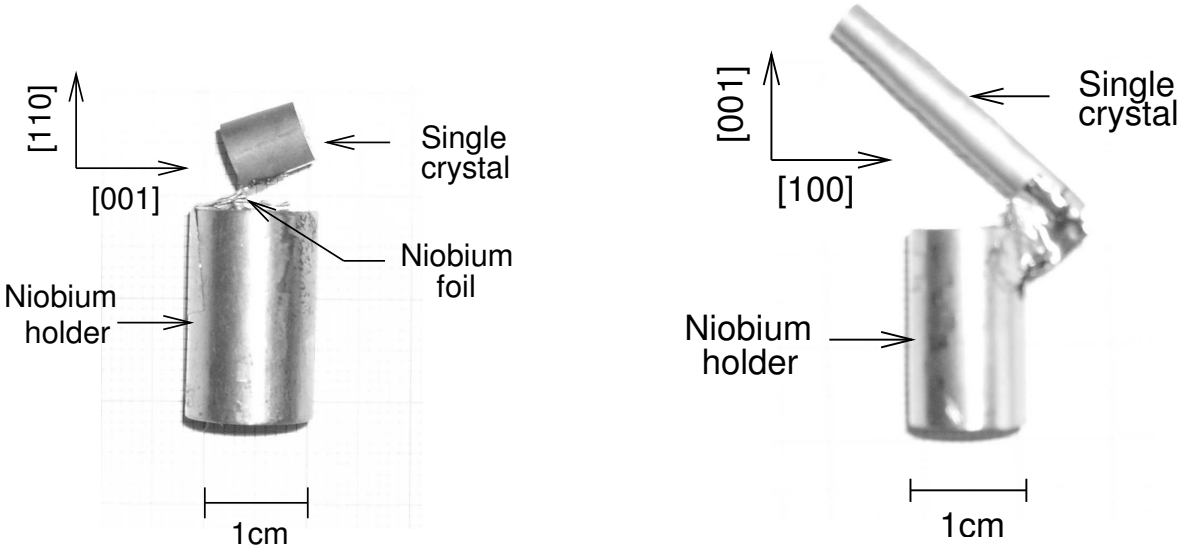

Figure 4.3: Oriented single crystals within the (110) scattering plane, $Ni_{51}Mn_{18}Al_{31}$ (left) and the (001) scattering plane, $Ni_{53}Mn_{22}Al_{25}$ (right). The samples are mounted on a Nb holder.

4.4 Floating-zone technique

The Floating-zone technique is a sample-holder free single crystal growth method. The sample rod is kept by clamps or screws made of Mo at its top and bottom part. The molten zone, which is typically few millimeter long is achieved by RF heating. The coil is moved slowly along the cylindrical shaped sample rod starting from the bottom. Vacuum conditions are those of ultra-high vacuum but depend sensitively on the actual vapour pressure of the sample. In case of strongly evaporating samples, experiments are performed under a slight over pressure of high purity Argon. A key parameter for successful crystal growth using this technique is the surface tension. Contrary to Ni_2MnAl, the surface tension of NiTi is relatively high allowing for a good control of the molten charge.

First, the martensitic transition temperature in NiTi has been characterised using DSC.

Ni_xTi_{100-x} alloys with x =50.2, 50.6 and 50.8 were prepared by arc-melting of pure elements under Argon atmosphere. All samples were solution annealed for 1 hour at 1273 K under Argon atmosphere and subsequently water quenched. The measured Martensitic start temperatures (M_s) are in the range of 190-220 K and slightly sensitive to the thermal cycling as previously reported by Matsumoto [Mat02]. A two-step transformation has been seen in the case of $Ni_{50.2}Ti_{49.8}$, in which case a slight departure of M_s from the expected line reported in the literature [Ots02] is observed.

Based on those results, first attempts to grow $Ni_{50.2}Ti_{49.8}$ and $Ni_{50.8}Ti_{49.2}$ single crystals have been made using the floating-zone technique. Rods of 8-10 mm in diameter have been pulled at different speeds *e.g.* 15-20 mm/h. Transversal cross-sections have been cut, mechanically polished and etched to get optical micrographs. An example is shown in Fig. 4.4. Surprisingly, the micrograph revealed a martensitic texture signature of a martensitic transition occurring well above the indicated temperature from the preliminary measurements. For seek of completeness, DSC measurements have been performed on as-prepared samples of NiTi. They all show a single-step transition above or around the room temperature. In order to avoid the *in-situ* single crystal growth, higher Ni concentrations have been investigated to lower M_s. A transition temperature of 268 K has been found for x =51. $Ni_{51}Ti_{49}$ rods of 8 mm in diameter have been pulled along 5-6 cm at 12 mm/h. Grain-size of 2-3 mm have been obtained. The manual control of the molten zone during the crystal growth makes the growth at lower speeds quite difficult. To avoid this, a part-by-part crystal growth has been tried. The lowest part of the rod is pulled in a first run at 4 mm/h during 6h. The growth is then stopped and carried later on during a second run after moving the coil down to start 5-8 mm below. After 3-4 runs, distancies of 6-7 cm are reached. This procedure did however not sucessfully work.

A NiTi single crystal grown by the Brigdman technique in a graphite crucible has been lent to us by Prof. G. Eggeler (Lehrstuhl Werkstoffwissenschaft an der Ruhr Universität Bochum). Due to the high diffusion of C in the NiTi matrix at high temperature, TiC coherent preciptates are formed during the growth process. TiC has a cubic NaCl-type crystal structure with a well defined orientation relationship with the B2-NiTi matrix (B2[100]//TiC[110], see Fig. 4.4) [Zha06]. Besides the fundamental reflexions are lying very close to each other. Neutron scattering perfomed on such a single crystal revealed systematic peaks of the TiC phase.

The growth of good quality NiTi single crystals is of crucial interest to investigate the lattice dynamics of the most used SMA and address open questions regarding the origin of the precursor effects observed prior to the martensitic transition in Ni-based SMA. It remains up to know an appealing challenge.

4.5 Characterisation

Cross-sections have been cut from the pulled crystals. After polishing and chemical etching an optical microscope was used to check for the presence of grain boundaries. The x-ray Laue back-reflexion technique has been used to check for the orientation of the

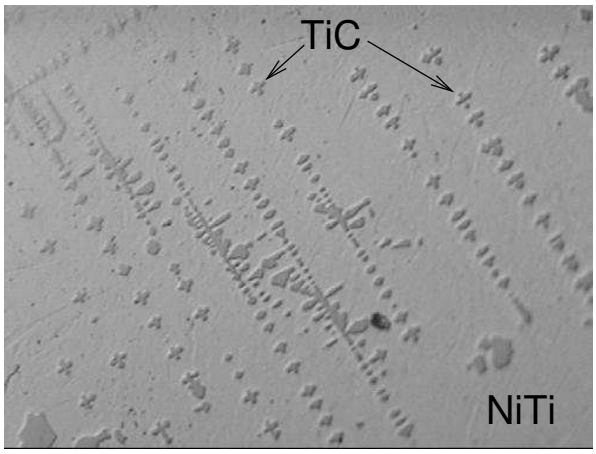

Figure 4.4: Optical micrograph of a NiTi single crystal grown by Bridgman in a graphite crucible showing the coherent TiC precipitates.

grain present at the cross-section. Pictures have been taken at different positions which revealed the same reflexion pattern meaning that a single grain is extending over the whole cross-section. However the as pulled crystals have usually random orientation. The next step consists in their orientation. This procedure involves two basic tasks: determining an unknown orientation and setting a sample in a desired orientation by means of Laue back-reflexion technique.

The experimental setup for the Laue back-reflexion technique is illustrated schematically in Fig. 4.5. The x-ray source used produces a beam of x-rays over a wide range of wavelengths using a Cu anode. The pinhole arrangement yields a well-collimated beam incident on the sample. A flat photographic film is placed perpendicular to the incident beam between the source and the sample to intercept the reflected diffracted beams. The problem is to determine the orientation of the single crystal from the position of the Laue spots on the film. Knowing the sample-to-film distance d_{film} and the distance r of a spot from the center of the film, the Bragg angle θ for the corresponding reflexion can be calculated. But this is no help in identifying the planes producing a particular spot, because the wavelength λ of the diffracted beam is not known a priori, which is required in order to calculate the interplanar distance d from the Bragg's law. The orientation of the normal to the planes producing each spot is known, however, this normal always bisects the angle between the incident and the diffracted beam. A stereographic projection can be constructed from directions of those normals. In a stereographic projection angles between plane normals can be measured and compared with a list of known interplanar angles for the single crystal involved. Stereographic projection have already been published in literature for the low-index planes. Such standard stereographic projections are given in Refs. [Joh69, Lau74]. To compare a stereographic projection constructed from back-reflexion Laue pattern with standard stereographic projections, the stereographic projections are rotated so as to get a low index zone axis in the center. This is done by rotating a zone containing many reflexions until it coincides with the periphery of the stereographic map by means of a Wulff net. It is convenient to mount the sample whose orientation is unknown on a goniometer. Usually a first Laue pattern will not coincide with none of the diagrams reported in literature. Therefore, in general case the next step is to look for a *major spot* which is not only a strong reflexion but one through which

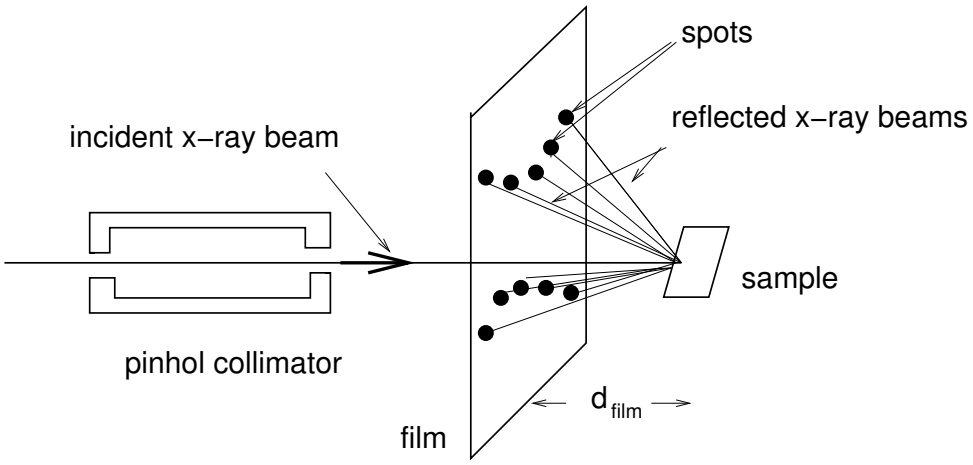

Figure 4.5: Scheme of the experimental setup for Laue back-reflexion patterns.

many zones pass (high symmetry point). In order to identify that reflexion the sample is tilted on the goniometer in such a way that this reflexion occurs in the center on the next Laue pattern. The whole procedure can be very time consuming especially in complex structures.

Ni_2MnAl single crystals have been oriented to have either the (001) or the (110) planes coincide with the scattering plane for neutron measurements and mounted on a Niobium holder (Fig. 4.3). Repositioning of the crystals was, however, necessary during neutron measurements to access different phonon branches in different directions.

The chemical composition of the single crystals has been measured using the Elastic Recoil Detection (ERD) technique on pieces cut out of the pulled rods. Elastic Recoil Detection (ERD) [Ecu76, Doy79] is an ion beam analysis technique for quantitative analysis of chemical elements in solids. The sample which has to be analysed is irradiated with an ion beam (*e.g.* ^{58}Ni, ^{127}I, or ^{197}Au ions) of several MeV energy. Light elements (*e.g.* H, D) from the sample are scattered in forward directions and can be detected with a Si detector. From the measured energy spectrum of the recoils a concentration depth profile can be calculated. The detection of scattered ions from the incident ion beam is normally suppressed in order to avoid background. The easiest and most common method is the use of a foil which stops the scattered ions, but allows the passing of the recoils which have a lower stopping power. The scattering cross-section can be calculated assuming Rutherford scattering. For higher energies experimentally measured cross-section have to be used in most cases. The depth profile calculation can be done directly from the spectrum as described by Doyle [Doy88] or by using spectrum simulation programs such as RUMP [Doo85] or SENRAS [Viz90]. The ERD method provides absolute concentration values and is not affected by matrix effects. Furthermore ERD is non invasive,*e.g.* the sample is not damaged on a macroscopic scale.

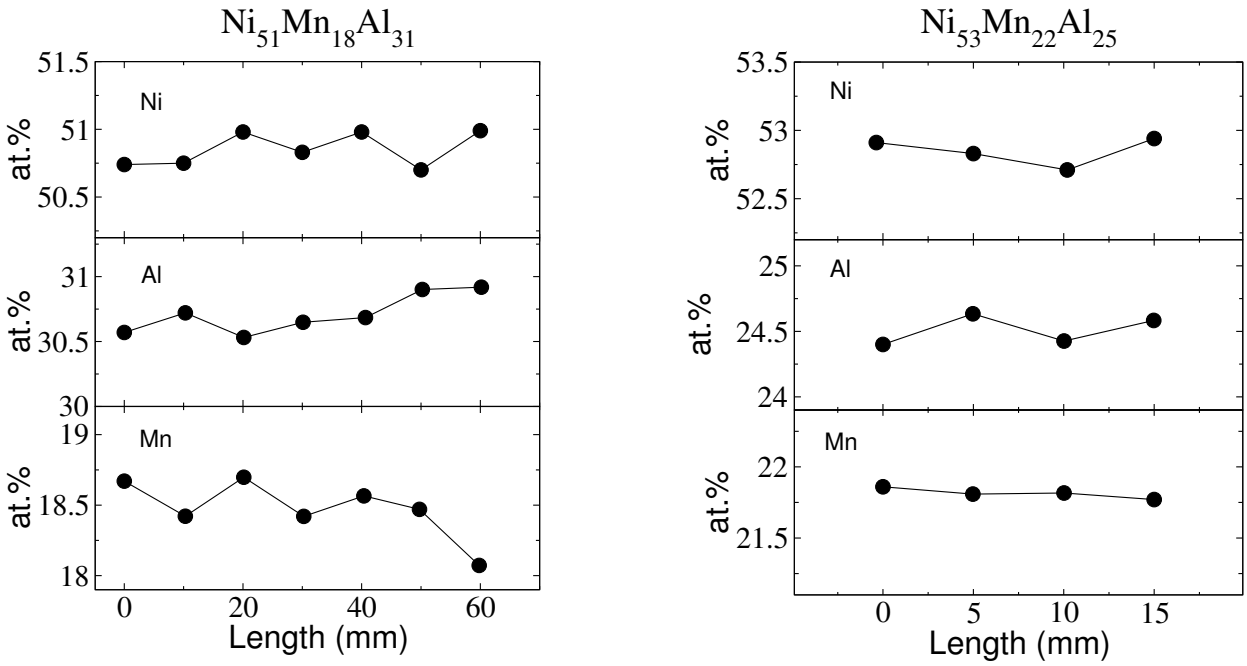

Figure 4.6: Chemical composition along the pulled rods as measured by Elastic Recoil Detection.

Prior to the ERD measurements, the pulled rods have been cut along the growth direction, mechanically polished and etched. Measurements have been performed at different positions of the rods. The measured compositions in the two samples are depicted together on Fig. 4.6. The chemical composition of the two crystals was found to be $Ni_{51}Mn_{18}Al_{31}$ and $Ni_{53}Mn_{22}Al_{25}$ respectively.

To keep the B2 atomic order at low temperature, the samples have been solution annealed in quartz tubes under Argon atmosphere at 1273 K for 3 days and subsequently water quenched. The mosaic spread has been measured at room temperature on the three-axis spectrometer PUMA (Forschungsneutronenquelle Heinz Maier-Leibnitz, Garching), using incident neutrons with a wavevector 2.662 $\AA^{-1}$. The full width at half maximum (FWHM) of the fundamental reflexions was 1.2° and 1.35° for $Ni_{51}Mn_{18}Al_{31}$ and $Ni_{53}Mn_{22}Al_{25}$ respectively (Fig. 4.7).

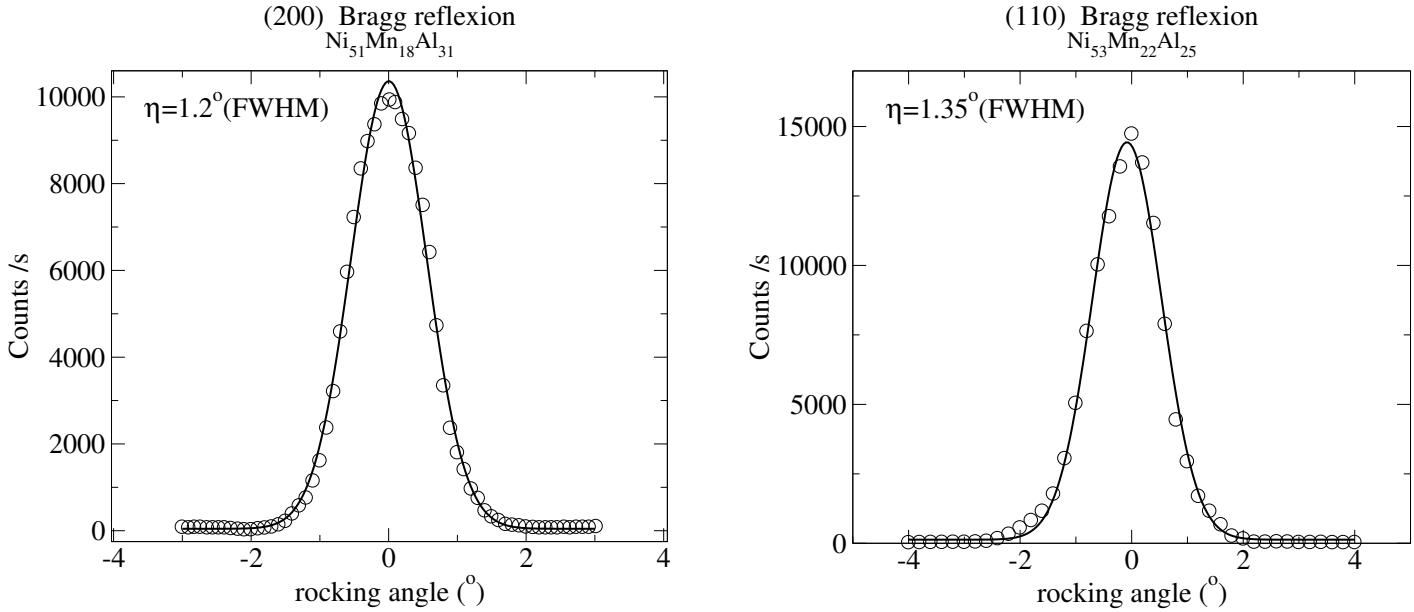

Figure 4.7: Rocking curves measured at the (200) and (110) fundamental reflexions by neutrons ($k_i = k_f = 2.662\mathring{A}^{-1}$) at room temperature on the two single crystals $Ni_{51}Mn_{18}Al_{31}$ (left) and $Ni_{53}Mn_{22}Al_{25}$ (right) showing mosaic spread, η, of 1.2^o and 1.35^o respectively (FWHM).

Chapter 5

Lattice dynamics theory

In this chapter, we present an overview of the theory of lattice vibrations in crystals. We describe first the semi-classical approach of the lattice dynamics for a three dimensional crystal in the harmonic approximation. The concept of the normal modes vibration or phonon is then deduced from the quantum description of the lattice vibrations. Calculations of the related thermodynamic quantities such as phonon density of states and specifc heat are also presented.

5.1 Classical theory

We consider a general three dimensional lattice containing N unit cells and p atoms per unit cell. A unit cell, indexed by l, is situated at position $\mathbf{r}_l = l_1\mathbf{a}_1 + l_2\mathbf{a}_2 + l_3\mathbf{a}_3$, where $\mathbf{a}_1, \mathbf{a}_2, \mathbf{a}_3$ are the primitive translation vectors. The equilibrium position of the k-th atom in the l-th unit cell is given by: $\mathbf{r}_{l,k} = \mathbf{r}_l + \mathbf{r}_k$, where $\mathbf{r}_k$ gives the equilibrium position of the k-th atom in the considered unit cell. If now the atom is vibrating around its equilibrium position, its coordinate will be defined by $\mathbf{R}_{l,k} = \mathbf{r}_{l,k} + \mathbf{u}_{l,k}$ where $\mathbf{u}_{l,k}$ is the relative displacement of the k-th atom in the l-th unit cell around its equilibrium position.

Let us now derive the equation of motion of the considered atom. If we assume that the total potential energy $\mathcal{U}$ of the crystal is a function of the instantaneous positions of all atoms, we can expand the potential energy in a Taylor series in powers of small displacements around its minimum $\mathcal{U}_0$ [Sri90]:

$$\begin{aligned} \mathcal{U} &= \mathcal{U}_0 + \sum_{lk\alpha} \frac{\partial \mathcal{U}}{\partial u_\alpha(lk)}\Big|_0 u_\alpha(lk) + \frac{1}{2}\sum_{lk,l'k'}\sum_{\alpha\beta} \Phi_{\alpha\beta}(lk, l'k')u_\alpha(lk)u_\beta(l'k') + \cdots \\ &= \mathcal{U}_0 + \mathcal{U}_1 + \mathcal{U}_2 + \cdots \end{aligned} \tag{5.1}$$

where the indices α and β stand for the Cartesian coordinates x, y and z. The equilibrium value, $\mathcal{U}_0$, is a constant and is unimportant for the dynamical problems. The second term of the expansion vanishes in the equilibrium configuration and

$$\Phi_{\alpha\beta}(lk, l'k') = \frac{\partial^2 \mathcal{U}}{\partial u_\alpha(lk)\partial u_\beta(l'k')}\Big|_0. \tag{5.2}$$

If the atomic displacements are now assumed to be small, so that the forces may be regarded as essentially linear functions of the atomic displacements (Hooke's law), the

higher orders in equation (5.1) can be neglected. The consideration of only the quadratic term in the above expansion is known as the *harmonic approximation*. In this picture, the lattice is treated as a collection of coupled simple harmonic oscillators and the potential energy of the crystal reduces to

$$\mathcal{U} = \frac{1}{2} \sum_{lk,l'k'} \sum_{\alpha\beta} \Phi_{\alpha\beta}(lk, l'k') u_\alpha(lk) u_\beta(l'k'). \tag{5.3}$$

The force constant matrix elements $\Phi_{\alpha\beta}(lk, l'k')$ have to obey a number of symmetry requirements. First of all, the infinitesimal translational invariance of the crystal (*i.e.* when all the atoms are equally displaced, there is no force on any atom) leads to

$$\sum_{lk} \Phi_{\alpha\beta}(lk, l'k') = 0. \tag{5.4}$$

The invariance of the potential energy $\mathcal{U}$ and its derivatives against symmetry operations, such as translations, ensures $\Phi_{\alpha\beta}(lk, l'k') = \Phi_{\alpha\beta}(0k, l - l'k')$. The symmetry operations do not only leave the potential and its derivatives invariant but also the undistorted lattice. Under these symmetry operations, therefore, not only the numerical value of the potential energy but also the form of the expression for it, equation (5.3), is invariant. This invariance implies that the force constants of the ideal lattice do not depend on the absolute positions of the primitive cells but only on their distance vectors. The symmetry of the force constants are technically very important because they reduce significantly the calculation efforts.

If we take the derivative of $\mathcal{U}$ with respect to the relative atomic displacement $u_\alpha(lk)$, we get the force $F_{lk\alpha}$ acting on the atom (lk) in the direction α. In absence of any external applied field (stress, electric or magnetic field) the equation of motion reads

$$F_{lk\alpha} = m_k \ddot{u}_\alpha(lk) = -\frac{\partial \mathcal{U}}{\partial u_\alpha(lk)} = -\sum_{l'k'\beta} \Phi_{\alpha\beta}(lk, l'k') u_\beta(l'k') \tag{5.5}$$

where m_k is the mass of the k-th atom and Φ is the interatomic force constant matrix, also called *matrix of coupling parameters*, defined in equation (5.2). In fact, $\Phi_{\alpha\beta}(lk, l'k')$ represents the force, in the direction α, acting on the k-th atom of the l-th unit cell due to a unit displacement of the k'-th atom in the l'-th unit cell with all other atoms in their equilibrium positions.

The equation of motion (5.5) can be written in a symmetrised form as

$$\ddot{w}_\alpha(lk) = -\sum_{l'k'\beta} \mathcal{D}_{lk\alpha}^{l'k'\beta} w_\beta(k'l') \tag{5.6}$$

where $w_\alpha(lk) = \sqrt{m_k} u_\alpha(lk)$ and the matrix

$$\mathcal{D}_{lk\alpha}^{l'k'\beta} = \frac{1}{\sqrt{m_k m_{k'}}} \frac{\partial^2 \mathcal{U}}{\partial u_\alpha(kl) \partial u_\beta(k'l')} \tag{5.7}$$

is called the *dynamical matrix*. The matrix $\mathcal{D}$ is real and symmetric. For the same symmetry reasons as for the force constant matrix, the matrix elements $D_{lk\alpha}^{l'k'\beta}$ do not

depend on the absolute position of the primitive cell but on their relative distance. Thus $\mathcal{D}_{lk\alpha}^{l'k'\beta} = \mathcal{D}_{k\alpha}^{k'\beta}(\mathbf{r}_{l'} - \mathbf{r}_l) = \mathcal{D}_{k\alpha}^{k'\beta}(l' - l)$.

To solve the system of equations (5.6), we try a solution in the form of plane waves:

$$w_\alpha(lk) = e_{k\alpha}(\mathbf{q})\ exp[i(\mathbf{q}\mathbf{r}_l - \omega t)]. \tag{5.8}$$

Inserting equation (5.8) in equation (5.6), we get

$$\omega^2 e_{k\alpha}(\mathbf{q}) = \sum_{l'k'\beta} \mathcal{D}_{k\alpha}^{k'\beta}(l' - l)\ exp[i\mathbf{q}(\mathbf{r}_{l'} - \mathbf{r}_l)]. \tag{5.9}$$

As we can see, the plane waves allow to simplify the problem from a coupled system of $3pN$ differential equations to N systems of $3p$ linear equations. For a crystal with p atoms per unit cell and for each value of $\mathbf{q}$, there are $3p$ solutions with eigenvalues $\omega_j^2(\mathbf{q})$ and eigenvectors $\mathbf{e}_k(j, \mathbf{q})$ to this problem. A complete solution of the eigenproblem of equation (5.9) is thought in terms of $\omega = \omega_j(\mathbf{q})$, called the phonon dispersion relation for eigenvalues, and $\mathbf{e} = \mathbf{e}_j(\mathbf{q})$ (also noted $\mathbf{e} = \mathbf{e}(j, \mathbf{q})$), called the dispersion relation for eigenvectors. An eigenmode with frequency ω_j and eigenvector $\mathbf{e}_k(j, \mathbf{q})$ is called the j-th *normal mode* or *phonon* of the system. The graphical representation of the $3p$ functions $\omega_j(\mathbf{q})$ as a function of $\mathbf{q}$ is called the *vibrational dispersion spectrum* of the system. The index $j = 1, 2, 3, \cdots, 3p$ stands for the phonon branch. Since the *dynamical matrix* is real and symmetric, the eigenvalues are real. The harmonic system is stable if all eigenvalues are positive. It is sometimes convenient to use, instead of real eigenvectors, complex ones. E.g., in a translationally invariant lattice, the normal modes are plane waves which are mostly characterised by eigenvectors of the form $exp(i\mathbf{q}.\mathbf{r})$. The fact that the atomic displacement is real requires the condition:

$$\mathbf{e}_k^*(j, \mathbf{q}) = \mathbf{e}_k(-j, \mathbf{q}); \quad \omega_j(\mathbf{q}) = \omega_j(-\mathbf{q}). \tag{5.10}$$

The eigenvectors can be chosen orthogonal:

$$\sum_{k\alpha} \mathbf{e}_{k\alpha}^*(j, \mathbf{q}).\mathbf{e}_{k\alpha}(j', \mathbf{q}) = \delta_{jj'} \tag{5.11}$$

and

$$\sum_{j} \mathbf{e}_{k\alpha}^*(j, \mathbf{q}).\mathbf{e}_{k'\alpha'}(j, \mathbf{q}) = \delta_{kk'}\delta_{\alpha\alpha'}. \tag{5.12}$$

Out of the $3p$ phonon branches, there will be 3 *acoustic* branches such that $\omega(\mathbf{q}) \to 0$ when $\mathbf{q} \to 0$ and $3p - 3$ *optical* branches such that $\omega(\mathbf{q}) \to$ constant $\neq 0$ when $\mathbf{q} \to 0$. Atomic vibrations corresponding to any of the branches, acoustic or optical, can either be longitudinal such that $\mathbf{e} \parallel \mathbf{q}$ or transverse such that $\mathbf{e} \perp \mathbf{q}$, or a mixture of longitudinal and transverse. The elastic continuum theory shows that in an isotropic crystal, it is always possible to construct three mutually independent polarisation modes for a given $\mathbf{q}$: $\mathbf{e} \parallel \mathbf{q}$ and $\mathbf{e_{T_1}} \perp \mathbf{e_{T_2}} \perp \mathbf{q}$. In an anisotropic crystal, a clear relationship between $\mathbf{e}$ and $\mathbf{q}$ does not exist, except when $\mathbf{q}$ is along a high symmetry direction. For example, in cubic crystals the concept of pure longitudinal and transverse polarisation modes is only defined when $\mathbf{q}$ is along the symmetry directions [100], [110] and [111]. In tetragonal crystals even the [111] branches become mixed.

5.2 Quantum theory

So far we have treated the atomic vibrations within classical mechanics. For many applications, however, quantum properties are needed. In this case, the energy function (5.3) is the potential part of the Hamiltonian of the system, $\mathcal{H}$. The vibrational wavefunctions can then be derived by the standard methods to treat the harmonic oscillator. The Hamiltonian of the system reads in the harmonic approximation

$$\mathcal{H} = \sum_{lk} \frac{\mathbf{p}^2(lk)}{2m_k} + \frac{1}{2} \sum_{lk,l'k'} \sum_{\alpha\beta} \Phi_{\alpha\beta}(lk, l'k') u_\alpha(lk) u_\beta(l'k') \tag{5.13}$$

where $\mathbf{p}(kl)$ is the momentum operator of the k-th atom in the l-th unit cell. The form (5.13) of the Hamiltonian is quite complicated, it can be simplified by introducing normal coordinate operators $\mathbf{X}(\mathbf{q})$ and $\mathbf{P}(\mathbf{q})$, Fourier transforms of the coordinate $\mathbf{u}$ and $\mathbf{p}$:

$$\mathbf{u}(lk) = \frac{1}{\sqrt{V}} \sum_{\mathbf{q}} \mathbf{X}(\mathbf{q}, k)\ exp(i\mathbf{q}.\mathbf{r}_l) \tag{5.14}$$

$$\mathbf{p}(lk) = \frac{1}{\sqrt{V}} \sum_{\mathbf{q}} \mathbf{P}(\mathbf{q}, k)\ exp(-i\mathbf{q}.\mathbf{r}_l) \tag{5.15}$$

where V is the volume of the crystal. Since $\mathbf{u}(lk)$ and $\mathbf{p}(lk)$ are Hermitian, we have

$$\mathbf{X}^\dagger(\mathbf{q}, k) = \mathbf{X}(-\mathbf{q}, k) = \frac{1}{\sqrt{V}} \sum_{l} \mathbf{u}(lk)\ exp(i\mathbf{q}.\mathbf{r}_l) \tag{5.16}$$

$$\mathbf{P}^\dagger(\mathbf{q}, k) = \mathbf{P}(-\mathbf{q}, k) = \frac{1}{\sqrt{V}} \sum_{l} \mathbf{p}(lk)\ exp(-i\mathbf{q}.\mathbf{r}_l) \tag{5.17}$$

i.e. the new coordinate operators are non Hermitian. These operators satisfy the commutation relations:

$$[\mathbf{X}(\mathbf{q}, k), \mathbf{P}(\mathbf{q}', k')] = \ i\hbar\delta_{\mathbf{q}\mathbf{q}'}\delta_{kk'}\ \mathbf{I} \tag{5.18}$$

where $\mathbf{I}$ is the identity operator and $\hbar$ the reduced Planck constant. The substitution of equations (5.14) into equation (5.13) gives

$$\begin{aligned} \mathcal{H} \ = \ & \frac{1}{V} \sum_{lk\mathbf{q}\mathbf{q}'} \frac{\mathbf{P}(\mathbf{q}, k)\ .\ \mathbf{P}(\mathbf{q}', k)}{2m_k}\ exp[-i(\mathbf{q} + \mathbf{q}')\mathbf{r}_l] + \frac{1}{2}\frac{1}{V} \sum_{lk,l'k'\mathbf{q}\mathbf{q}'} \\ & \sum_{\alpha\beta} \Phi_{\alpha\beta}(lk, l'k') X_\alpha(\mathbf{q}, k) X_\beta(\mathbf{q}', k')\ exp[i(\mathbf{q}.\mathbf{l} + \mathbf{q}'.\mathbf{l}')] \end{aligned} \tag{5.19}$$

The Hamiltonian (5.19) can be simplified by performing the summation over l in the first term and introducing $h = l - l'$ and defining in the second term $\Phi_{\alpha\beta}(kk', \mathbf{q})$:

$$\begin{aligned} \Phi_{\alpha\beta}(kk', \mathbf{q}) \ &= \ \sqrt{m_k m_{k'}}\mathcal{D}_{\alpha\beta}(kk', -\mathbf{q}) \\ &= \ \sum_{h} \Phi_{\alpha\beta}(0k, hk')\ exp(-i\mathbf{q}.\mathbf{r}_h) \end{aligned} \tag{5.20}$$

The Hamiltonian can be then written

$$\mathcal{H} = \sum_{\mathbf{q}k} \frac{\mathbf{P}(\mathbf{q},k)\ .\ \mathbf{P}^{\dagger}(\mathbf{q},k)}{2m_k} + \frac{1}{2}\sum_{\mathbf{q},k,k'\alpha\beta} \Phi_{\alpha\beta}(kk^{'},\mathbf{q})X_{\alpha}(\mathbf{q},k)X^{\dagger}_{\beta}(\mathbf{q},k^{'}) \tag{5.21}$$

At this stage, the crystal Hamiltonian is viewed in terms of the coordinates $\mathbf{X}(k\mathbf{q})$ and the momenta $\mathbf{P}(k\mathbf{q})$ of pN atoms, coupled by a set of harmonic force constants $\Phi(kk^{'},\mathbf{q})$. Thus for each value of $\mathbf{q}$ the problem of finding the normal modes of the system is equivalent to finding the eigenstates of the Hamiltonian. For this purpose, following section 5.1 we introduce the polarisation vector $\mathbf{e}_k(j,\mathbf{q})$ to represent the magnitude and direction of vibration mode $(j,\mathbf{q})$, where j denotes the polarisation branch. The $\mathbf{e}_k(j,\mathbf{q})$ obey the orthogonality relation (5.11). With the introduction of $\mathbf{e}_k(j,\mathbf{q})$, we do another set of normal coordinate transformations

$$X(j,\mathbf{q}) = \sum_k \sqrt{m_k}\mathbf{e}^*{}_k(j,\mathbf{q}).\mathbf{X}(\mathbf{q},k) \tag{5.22}$$

$$P(j,\mathbf{q}) = \sum_k \frac{1}{\sqrt{m_k}}\mathbf{e}_k(j,\mathbf{q}).\mathbf{P}(\mathbf{q},k). \tag{5.23}$$

We introduce the phonon annihilation and creation operators defined respectively by

$$b_{j,\mathbf{q}} = \frac{1}{\sqrt{2\hbar\omega_j(\mathbf{q})}}\mathbf{P}(j,\mathbf{q}) - i\sqrt{\frac{\omega_j(\mathbf{q})}{2\hbar}}\mathbf{X}^{\dagger}(j,\mathbf{q}) \tag{5.24}$$

$$b^{\dagger}_{j,\mathbf{q}} = \frac{1}{\sqrt{2\hbar\omega_j(\mathbf{q})}}\mathbf{P}^{\dagger}(j,\mathbf{q}) + i\sqrt{\frac{\omega_j(\mathbf{q})}{2\hbar}}\mathbf{X}(j,\mathbf{q}). \tag{5.25}$$

It can be verified that these operators obey the commutation relations $[b_{j,\mathbf{q}}, b^{\dagger}_{j^{'},\mathbf{q}^{'}}] = \delta_{\mathbf{q}\mathbf{q}^{'}}\delta_{j,j^{'}}$. Equations (5.24) can be inverted. Using $\omega_j(\mathbf{q}) = \omega_j(-\mathbf{q})$, (5.17) and (5.22), we have:

$$\mathbf{X}(k\mathbf{q}) = -i\sum_j \sqrt{\frac{\hbar}{2m_k\omega_j(\mathbf{q})}}\mathbf{e}_j(\mathbf{q},l)(b^{\dagger}_{j,\mathbf{q}} - b_{j,-\mathbf{q}}) \tag{5.26}$$

$$\mathbf{P}(k\mathbf{q}) = \sum_j \sqrt{\frac{m_k\hbar\omega_j(\mathbf{q})}{2}}\mathbf{e}^*_j(\mathbf{q},l)(b^{\dagger}_{j,\mathbf{q}} - b_{j,-\mathbf{q}}) \tag{5.27}$$

We now have expressions of the coordinate and the momenta vector $\mathbf{X}(k\mathbf{q})$ and $\mathbf{P}(k\mathbf{q})$ in terms of the phonon creation and annihilation operators and the polarisation vectors. If we substitute equations (5.26) in equation (5.21), we get a simple expression of the Hamiltonian

$$\mathcal{H} = \sum_{\mathbf{q}j} \hbar\omega_j(\mathbf{q})(b^{\dagger}_{j,\mathbf{q}}b_{j,\mathbf{q}} + \frac{1}{2}) \tag{5.28}$$

At this stage we expressed the Hamiltonian of the system as a sum of $3pN$ Hamiltonians of independent Harmonic oscillators. The eigenvalues of $\mathcal{H}$ are well known from the quantum treatment of the harmonic oscillator which can be found in many text books [Tan77]. Let

us denote by $|n_{j\mathbf{q}}>$ an eigenstate which has n phonons of wave vector $\mathbf{q}$ and polarisation j. The effect of the operators $b_{j,\mathbf{q}}$, $b^{\dagger}_{j,\mathbf{q}}$ and $b^{\dagger}_{j,\mathbf{q}}b_{j,\mathbf{q}}$ on the state $|n_{\mathbf{q}j}>$ are given as follows

$$\begin{aligned} b^{\dagger}_{j,\mathbf{q}}|n_{j\mathbf{q}}> &= \sqrt{n_{j\mathbf{q}}+1}|n_{j\mathbf{q}}+1> \\ b_{j,\mathbf{q}}|n_{j\mathbf{q}}> &= \sqrt{n_{j\mathbf{q}}}|n_{j\mathbf{q}}-1> \\ b^{\dagger}_{j,\mathbf{q}}b_{j,\mathbf{q}}|n_{j\mathbf{q}}> &= n_{j\mathbf{q}}|n_{j\mathbf{q}}> \end{aligned} \tag{5.29}$$

$b^{\dagger}_{j,\mathbf{q}}b_{j,\mathbf{q}}$ is a phonon number operator which gives the number of phonons in the $(j,\mathbf{q})$ state. Using equations (5.28) and (5.29) we get

$$\mathcal{H}|n_{\mathbf{q}j}>=\sum_{j\mathbf{q}}\hbar\omega_j(\mathbf{q})(n_{j\mathbf{q}}+\frac{1}{2})|n_{j\mathbf{q}}>=\sum_{j\mathbf{q}}\epsilon_{j\mathbf{q}}|n_{j\mathbf{q}}> \tag{5.30}$$

and the average energy of the phonons in the mode $(j,\mathbf{q})$: $\bar{\varepsilon}_{j\mathbf{q}}=\hbar\omega_j(\mathbf{q})\bar{n}_{j\mathbf{q}}$ where the thermal average $\bar{n}_{j\mathbf{q}}$ is the Bose-Einstein distribution function. The term due to $\frac{1}{2}$ in equation (5.30) is the zero-point energy.

5.3 Phonon density of states

In the following sections, we will perform sums or integrals of functions of the dispersion over the crystal momentum state $\mathbf{q}$ within the reciprocal lattice. However, the translational symmetry of the crystal often greatly reduces the set of points for the summation. Let us once more consider a three-dimensional crystal with $N=L^3$ unit cells, where L is the linear size of the crystal along x, y and z. If we apply the periodic boundary conditions along the three directions, we seek phonon states of the type $\psi(\mathbf{r})=A\ exp[i(\mathbf{q}.\mathbf{r}-\omega t)]$ obeying $\psi(\mathbf{r})=\psi(\mathbf{r}+\mathbf{r}_L)$ where $\mathbf{r}_l=L\mathbf{a}_1$. Thus

$$q_x,q_y,q_z=0;\pm\frac{2\pi}{L};\pm\frac{4\pi}{L};\cdots;\pm\frac{N\pi}{L} \tag{5.31}$$

i.e. the allowed $\mathbf{q}$ values form a cubic mesh in $\mathbf{q}$-space, with one $\mathbf{q}$ confined to a volume $(2\pi/L)^3$. Therefore, for each phonon polarisation index, a unit volume in the $\mathbf{q}$-space contains $(L/2\pi)^3$ values of $\mathbf{q}$. $(L/2\pi)^3$ is called the *phonon density of states*, noted DOS, in the $\mathbf{q}$-space and gives the number of vibrational states or normal modes between wave vectors $\mathbf{q}$ and $\mathbf{q}+d\mathbf{q}$

$$g(\mathbf{q})d\mathbf{q}=\frac{V}{(2\pi)^3}d\mathbf{q} \tag{5.32}$$

where $V=L^3$ is the volume of the crystal. Equivalently, we can define $g(\omega)$, the number of normal modes which have a frequency between ω and $\omega+d\omega$. The partial phonon density of states of the branch j is $g(\omega_j)=\frac{V}{(2\pi)^3}\int\frac{dS_\omega}{|\nabla_{\mathbf{q}}\omega_j|}$ To get the total density of states, we sum over all branches

$$g(\omega)=\sum_j g(\omega_j)=\sum_j\frac{V}{(2\pi)^3}\int\frac{dS_\omega}{|\nabla_{\mathbf{q}}\omega_j|} \tag{5.33}$$

$v_g = \nabla_{\mathbf{q}}\omega_j$ is the *group velocity*. For some $\mathbf{q}$-values, v_g approaches zero and leads to $g(\omega) \to \infty$. Such points in the $\mathbf{q}$-space are called *critical points* and the singularities in the density of states are known as *van Hove singularities*.

The phonon density of states is one of the most important quantities in the lattice dynamical studies. Its determination however requires the calculation of the integral which appears in (5.33) over the whole Brillouin zone. In general such an integration requires the knowledge of phonon frequencies of wave vectors $\mathbf{q}$ in the entire Brillouin zone. However, in most experimental determinations of the normal mode of vibration such a task is not feasible with regard to the time and to the experimental effort required. In practice we proceed by an interpolation of the normal modes of vibration using some phenomenological models. Furthermore the point symmetry of the system is taken into account to reduce the phonon frequency calculation to wave vectors within the irreducible part of the Brillouin zone.

5.4 Lattice specific heat

The heat capacity at constant volume is an important quantity when dealing with the thermal properties of alloys. It defines the change in the internal energy E of the system when the temperature T is increased by an infinitesimal amount:

$$C_V = \Big(\frac{\partial \mathcal{U}}{\partial T}\Big)_V \tag{5.34}$$

At this stage, we should keep in mind that not only the phonons contribute to the internal energy $\mathcal{U}$. The electrons, as well as the magnetic moments, have a contribution to $\mathcal{U}$ but their dependence on T is different. In the following, we derive an expression of the phonon contribution to C_V.

We consider first the high temperature limit. According to the equipartition theorem, which holds at high temperature, the thermal energy of a given system is simply given by k_BT per quadratic term in the Hamiltonian ($\frac{1}{2}k_BT$ for both kinetic and potential energies). In the case of a crystal, with pN atoms, each of them are free to move in the three directions of space, we get $\mathcal{U} = 3pNk_BT$ and $C_V = 3Npk_B$. The molar specific heat of any solid at high temperature is thus $C_V^m = 3\mathcal{N}_Ak_B = 3R$, which is constant and independent on T. $\mathcal{N}_A$ is the Avogadro's number and R is the perfect gas constant. This is known as the law of Dulong and Petit.

To derive an expression for C_V at low temperatures, where the classical theory does not hold any more, we consider the phonons like a set a undiscernable particles that *a priori* can occupy any possible $(j, \mathbf{q})$ state with energy $\hbar\omega_j(\mathbf{q})$. The partition function of such a system is $\mathcal{Z} = \sum_s exp(-\beta\, \mathcal{U}_s)$ where $\beta = (k_BT)^{-1}$ and the index s stands for the different states. The energy $\mathcal{U}_s$ of the phonon gas is given by equation (5.28); we have

$$\mathcal{Z} = \prod_{j\mathbf{q}} \sum_{n_{j\mathbf{q}}} exp\Big[-\beta\,\Big(n_{j\mathbf{q}} + \frac{1}{2}\Big)\hbar\omega_j(\mathbf{q})\Big] = \prod_{j\mathbf{q}} \frac{exp\Big(-\beta\hbar\omega_j(\mathbf{q})/2\Big)}{1 - exp\Big(-\beta\hbar\omega_j(\mathbf{q})\Big)} \tag{5.35}$$

From mechanical statistics [Hil56] we know that the internal energy can be deduced

from the partition function as

$$\mathcal{U} = -\frac{\partial}{\partial\beta} ln\mathcal{Z} = \sum_{j\mathbf{q}} \frac{\hbar\omega_j(\mathbf{q})}{2} + \sum_{j\mathbf{q}} \overline{n}_{j\mathbf{q}} \hbar\omega_j(\mathbf{q}) \tag{5.36}$$

where the thermal average $\bar{n}_{\mathbf{q}j}$ is the Bose-Einstein distribution function and represents the average number of phonons in the state $(j, \omega_j(\mathbf{q}))$:

$$\bar{n}_{\mathbf{q}j} = \frac{1}{exp(\beta\hbar\omega_j(\mathbf{q})) - 1} \tag{5.37}$$

From equation (5.34), we can deduce C_V

$$C_V = \Big(\frac{\partial\mathcal{U}}{\partial T}\Big)_V = \sum_{j\mathbf{q}} \frac{(\hbar\omega_j(\mathbf{q}))^2}{k_B T^2} \frac{exp(\beta\hbar\omega_j(\mathbf{q}))}{\Big(exp(\beta\hbar\omega_j(\mathbf{q})) - 1\Big)^2} \tag{5.38}$$

In the previous derivations, we have assumed a finite model crystal. For an infinite periodic lattice, the allowed $\mathbf{q}$-values become dense and $\mathbf{q}$ a continuous variable. The summations over $\mathbf{q}$ are replaced by integrals

$$\sum_{\mathbf{q}} \rightarrow \int g(\mathbf{q}) d^3\mathbf{q} \rightarrow \int g(\omega) d\omega \tag{5.39}$$

The final expression for C_V is

$$C_V = \int_0^{\omega_{max}} g(\omega) \frac{(\hbar\omega)^2}{k_B T^2} \frac{exp(\beta\hbar\omega)}{(exp(\beta\hbar\omega) - 1)^2} d\omega. \tag{5.40}$$

If we consider now the high temperature limit, we can derive the Dulong and Petit law obtained using the classical theory.

$$C_V = k_B \int_0^{\omega_{max}} g(\omega) d\omega = 3pNk_B \tag{5.41}$$

The integral in equation (5.41) gives the total number of normal modes of vibration which is equal to the total number of degrees of freedom of the crystal.

Beside the specific heat, the phonon density of states allows the computation of the vibrational entropy S_{vib}, which is given in the harmonic approximation by:

$$S_{vib} = -3k_B \int g(\omega)[\overline{n}_{j\mathbf{q}}(\omega) ln(\overline{n}_{j\mathbf{q}}(\omega)) - (1 + \overline{n}_{j\mathbf{q}}(\omega)) ln(1 + \overline{n}_{j\mathbf{q}}(\omega))] d\omega \tag{5.42}$$

where $\overline{n}_{j\mathbf{q}}(\omega)$ is Bose-Einstein distribution given in equation (5.37).

The mean square atomic displacement can also be dedcued from the phonon density of states:

$$< u^2 >= \frac{\hbar}{4\pi M} \int coth\Big(\frac{\hbar\omega}{2k_B T}\Big) \frac{g(\omega)}{\omega} d\omega \tag{5.43}$$

5.5 Debye's model

The Dulong and Petit law has been corroborated by many experimental observations performed on metals, insulators as well as on semiconductors at high temperature. In the low temperature limit, the experimental observations show that C_V varies with T^3 in insulators and with T in metals. The behaviour in metals is dominated by the electronic contribution. A satisfactory explanation of the experimental results, for both high- and low-temperature variations of C_V in insulators emerged from the model of Debye for the phonon density of states.

In 1912, Debye used the isotropic continuum approximation of the phonon dispersion and considered the contributions from acoustic phonons in all polarisation branches with a frequency lower than a cut-off frequency ω_D called the Debye frequency [Deb12]. In this approximation, the velocity of sound is taken as constant and equal for all polarisation types, as it would be for a classical elastic continuum. Thus the dispersion relation reduces to

$$\omega = vq \tag{5.44}$$

where v is the constant velocity of sound. In the Debye model, considering a uniform density in the reciprocal space and taking relation (5.44) as valid, the phonon density of states reads

$$g_D(\omega) = \begin{cases} f\omega^2 & : \quad \omega \leq \omega_D \\ 0 & : \quad \omega \geq \omega_D \end{cases} \tag{5.45}$$

where f is a constant. The singularities in the real density of states are smeared out. The value of the constant f is chosen in the way that the integration in ω gives the total number of normal modes: we get $f = \frac{9pN}{\omega_D^3}$.

If we replace the expression of the Debye density of states (5.45) in equation (5.40), we get the specific heat in the Debye model

$$C_V = 9pNk_B\Big(\frac{T}{\theta_D}\Big)^3 \int_0^{\theta_D/T} \frac{x^4 e^x}{(e^x-1)^2} dx = 9pNk_B\Big(\frac{T}{\theta_D}\Big)^3 (\theta_D/T) \tag{5.46}$$

where $x = \hbar\omega/k_BT$, $\theta_D = \hbar\omega_D/k_B$ is called the Debye temperature and is the Riemann ζ function. At high temperature, $x \ll 1$, we get $C_V = 3pNk_B$, in agreement with Dulong and Petit law. At low temperature, $x \gg 1$, $\theta_D/T \approx \infty$ and $\zeta(\infty) = \frac{4\pi^4}{15}$ give $C_V = \frac{36\pi^4}{15}\ pNk_B\Big(\frac{T}{\theta_D}\Big)^3$.

The Debye model successfully explains both low- and high-temperature dependence of the lattice specific heat of insulating crystals. It should be emphasised that real crystals cannot be adequately treated as an elastic continuum and that their atomic nature must be considered. This requires an accurate evaluation of C_V from $g(\omega)$ using a realistic lattice dynamical model. The Debye formula of C_V can be nevertheless used; θ_D is then treated as an empirical parameter in equation (5.46). A usual way to choose the Debye temperature as a temperature-dependent parameter $\theta_D(T)$ is to adjust the measured heat capacity with equation (5.46).

5.6 Born-von Kármán model

In applications one is normally not interested in a specific phonon, but wants to know the influence of all phonons or of the lattice, e.g., specific heat, heat conductivity or thermal atomic displacements. What is needed, therefore, is a fast means to calculate the dynamical matrix. First principle calculations are at present much too time consuming, thus it is necessary to resort to phenomenological models. The parameters of these models are fitted to experimentally determined phonon frequencies, elastic constants and electric polarisabilities. The models serve to extrapolate from these properties to the whole dispersion curves. This extrapolation will be more reliable the more information on the nature of the material is built into it. Depending on the kind of interatomic bounding, preference is given to models with short-range interaction, screened electronic interaction, and models taking Coulomb and electric dipole interactions explicitly into account. In the following, we discuss one of the most used model, the Born-von Kármán model.

In principle the Born-Oppenheimer approximation allows the dynamic matrix of any system to be expressed by force constants which only have to obey the symmetry requirements discussed before. To describe a general nearest-neigbhour interaction in an fcc lattice, 3 independent force constants are needed. An extension to twice the range (4th neighbours) already needs 12 parameters. If there are two nonequivalent atoms in the unit cell, these numbers are doubled. On the other hand, the shape of the dispersion curves often necessitates fits by long range interactions, giving high Fourier coefficients. In order to reduce the number of parameters additional restrictions are introduced, e.g. axial symmetry forces, which can often be justified from first principle calculations.

In the axially symmetric model, one assumes that between a pair of atoms there is only one radial (longitudinal) and one transversal force constants, f_r and f_t respectively. Such a model can be thought of as derived from central pair potential $\mathcal{U}(r)$ and the two force constants are related to the derivative of $\mathcal{U}$

$$f_r = \frac{\partial^2 \mathcal{U}(r)}{\partial r^2} \quad and \quad f_t = \frac{1}{r}\frac{\partial \mathcal{U}(r)}{\partial r} \tag{5.47}$$

The coupling matrix then takes the form

$$\Phi_{\alpha\beta} = -(f_r - f_t)\frac{r_\alpha r_\beta}{r^2} - f_t \delta_{\alpha\beta} \tag{5.48}$$

where $\delta_{\alpha\beta}$ is the Kronecker symbol.

Fits with models of different range show that in general only the first few force constants are reasonably stable against the cutoff. Force constants for the interaction with the more distant neighbours fluctuate in sign and magnitude and are purely fit parameters without any physical meaning.

Chapter 6

Experimental investigation of the normal modes of vibration

In this chapter, we present a brief overview of the inelastic neutron scattering in crystals. The reader is referred to several references and text books for more detail.

6.1 Inelastic neutron scattering

The energy of thermal neutrons is in the same order of magnitude as that of the dynamical excitations in solids. So when the neutron is inelastically scattered by the creation or the annihilation of a phonon, the change in the energy of the neutron is a large part of its initial energy. A measurement of the neutron energy thus provides accurate information on energies of phonons and hence on interatomic forces. Thermal inelastic neutron scattering is one of the major tools to measure the phonon dispersion relation, that is the frequency ω_j as a function of $\mathbf{q}$ and polarization index j.

Consider a neutron, of momentum $\mathbf{k}_i$ and energy $E_i = \hbar^2 k_i^2/2m$, that is incident upon a crystal. After the interaction, the neutron emerges with momentum $\mathbf{k}_f$ and energy $E_f = \hbar^2 k_f^2/2m$. During the neutron-crystal interaction, a dynamical excitation of wave vector $\mathbf{q}$ and energy $\hbar\omega_j(\mathbf{q})$ is created or annihilated. The conservation laws of energy and momentum imply that the scattering process, in the case of phonon annihilation, obeys the conditions

$$E_f - E_i = \hbar\omega_j(\mathbf{q}) \tag{6.1}$$

and

$$\mathbf{k}_f - \mathbf{k}_i = \mathbf{q} + \mathbf{G} \tag{6.2}$$

where $\mathbf{G}$ is a reciprocal lattice vector. These conditions are so restrictive that for given scattering angles only few phonons of particular $\mathbf{q}$ and $\omega_j(\mathbf{q})$ can be involved in the scattering process. We can make use of this to determine the phonon dispersion $\omega_j(\mathbf{q})$. Generally a monochromatic beam arrives on the crystal and the energy of the neutrons scattered through a given angle is measured (by using a time-of-flight apparatus or another crystal as analyser). When a phonon is detected, the scattered energy gives access to $\mathbf{k}_f$ and equation (6.2) to the change in wave vector. As $\mathbf{q}$ has to lie on the first Brillouin zone, both $\mathbf{q}$ and $\mathbf{G}$ are obtained. One point on the phonon dispersion curve is determined.

In an inelastic neutron scattering experiment, the measured quantity is the partial differential cross section which gives the fraction of neutrons of incident energy E scattered into an element of solid angle $d\Omega$ with an energy between E and $E + dE$ [Squ78, Lov84]:

$$\Big(\frac{d^2\sigma}{d\Omega dE}\Big)(\mathbf{q},\omega) = \frac{(2\pi)^3}{2v_0}\frac{|\mathbf{k}_f|}{|\mathbf{k}_i|}\sum_{j,\mathbf{G}}\frac{|F_j(\mathbf{Q},\mathbf{q})|^2}{\omega_j(\mathbf{q})}(\Delta_- + \Delta_+) \tag{6.3}$$

where [Squ78, Lov84]

$$\Delta_- = \big(\overline{n}_{j\mathbf{q}} + 1\big)\delta\big(\omega - \omega_j(\mathbf{q})\big)\delta(\mathbf{Q} - \mathbf{q} - \mathbf{G}), \tag{6.4}$$

$$\Delta_+ = \overline{n}_{j\mathbf{q}}\delta\big(\omega + \omega_j(\mathbf{q})\big)\delta(\mathbf{Q} + \mathbf{q} - \mathbf{G}) \tag{6.5}$$

and v_0 is the volume of the unit cell, $\mathbf{Q} = \mathbf{k}_i - \mathbf{k}_f$ the scattering vector. $F_j(\mathbf{Q},\mathbf{q})$ is the *dynamical structure factor* given by:

$$F_j(\mathbf{Q},\mathbf{q}) = \sum_{k=1}^{p}\frac{b_k}{\sqrt{m_k}}exp(-W_k\mathbf{Q}^2)exp(i\mathbf{Q}.\mathbf{r}_k)\times(\mathbf{Q}.\mathbf{e}_k(j,\mathbf{q})) \tag{6.6}$$

b_k is the coherent scattering length of the k-th atom in the unit cell. $W_k = \langle u(k)^2\rangle/2$ where $\langle u(k)^2\rangle$ is the mean square displacement of atom k. $\overline{n}_{j\mathbf{q}}$ is the Bose-Einstein distribution. The delta functions in equations (6.4) and (6.5) express the conservation laws. Equation (6.4) describes a scattering process in which a phonon is created. The neutron energy decreases by an amount equal to the energy of a phonon of type j with a wave vector $\mathbf{q}$. Similarly equation (6.5) describes a phonon annihilation process where the energy of the neutron is increased.

In real systems, phonon-phonon and phonon-electron interactions tend to give single phonons a finite lifetime. A natural way to take account of this dissipation is to use the damped harmonic-oscillator model. In brief, the effect of damping is accomodated by replacing the delta function in equations (6.4) and (6.5) with Lorentzians. Equation (6.3) still applies if we make the substitution

$$\delta\big(\omega - \omega_j(\mathbf{q})\big) \rightarrow \frac{\Gamma_j(\mathbf{q})}{\big(\omega^2 - \omega_j^2(\mathbf{q})\big)^2 + \omega^2.\Gamma_j^2(\mathbf{q})} \tag{6.7}$$

where $\Gamma_j(\mathbf{q})$ is the peak half-width at half-maximum (HWHM) of the phonon spectra.

The intensity of the phonon observation by neutron scattering is determined by different factors. The term $1/\omega_j(\mathbf{q})$ in (6.3) indicates, independently of all other terms, that the intensity is inversely proportional to the frequency of the mode. This attenuation of the intensity results from the quantum mechanics of the harmonic oscillator. High energy modes are thus always more difficult to observe than the low-energy ones. Since neutron experiments suffer from the low flux of the existing sources, this effect frequently prohibits the study of the high frequency part of the phonon dispersion curves. The term $\overline{n}_{j\mathbf{q}}$ results from the Bose-Einstein statistics of a given mode with frequency $\omega_j(\mathbf{q})$, the occupation number is given by equation (5.37) and tends towards zero for $T \rightarrow 0$. For $T \rightarrow \infty$, $\overline{n}_{j\mathbf{q}}$ approaches $\hbar\omega_j(\mathbf{q})/k_BT$, *i.e.* the classical relation. Equation (6.4) indicates that the

Bose-Einstein function is increased by +1 in case of a phonon creation. At low temperature, where $\overline{n}_{j\mathbf{q}}$ is close to zero, the phonon can be observed only in the creation mode, the cross section for the annihilation process becomes vanishing since the phonon states are no longer occupied. At finite temperature, the Bose-Einstein distribution further simplifies the observation of phonons with low frequencies. One more factor in expression (6.6) is the scalar product $\mathbf{Q}.\mathbf{e}_k(j,\mathbf{q})$ which means that by measuring the intensity of the scattered signal, it is possible, in principle, to deduce the polarisation vectors $\mathbf{e}_k(j,\mathbf{q})$. In general the polarisation vectors corresponding to a given wave vector $\mathbf{q}$ are not related in a simple way to the direction of $\mathbf{q}$. But in certain cases there is a simple relation. For example, if $\mathbf{q}$ lies in the (001) plane of a cubic crystal, one of the $\mathbf{e}_k(j,\mathbf{q})$ is along the [001] axis. If the scattering vector $\mathbf{Q}$ is arranged so that $\mathbf{Q}$ is in the (001) plane, $\mathbf{Q}.\mathbf{e}_k(j,\mathbf{q})$ is zero for this mode. This can be used to extinguish one polarisation branch.

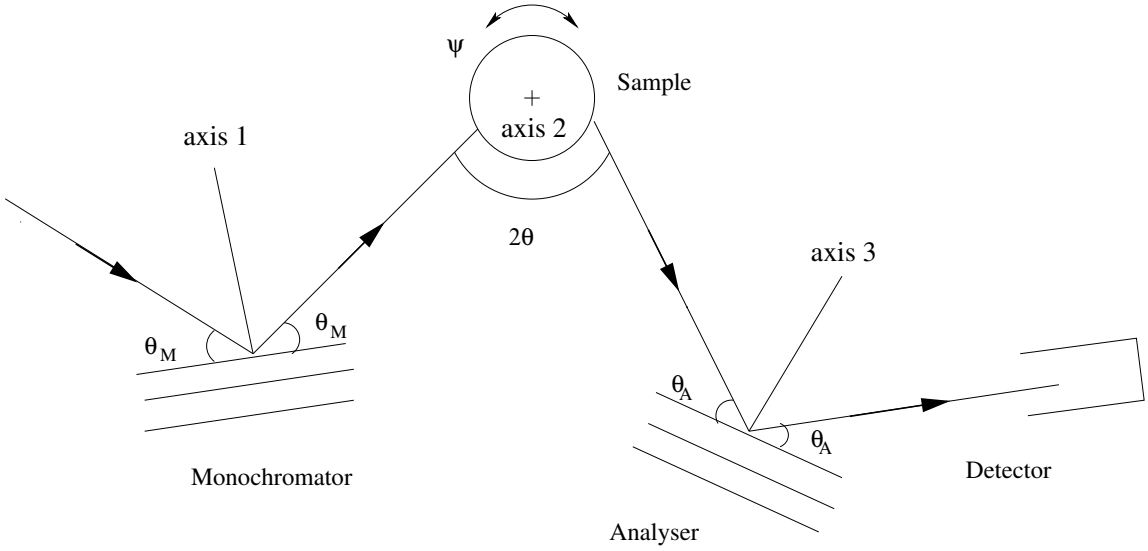

Figure 6.1: Three-axis spectrometer scheme with the different angles.

6.2 Three-axis spectrometer

Inelastic neutron scattering experiments are usually performed using either a time-of-flight setup or a three axis spectrometer. In the time-of-flight setup, the energy transfer of the inelastically scattered neutrons is deduced from the time the neutrons spend to fly over the distance chopper-sample-detector. The shift in time-of-flight, compared to that of the elastically scattered neutrons, can then be converted into a gain or a loss in energy. The time-of-flight method to measure phonon frequencies suffers from the disadvantage that for a given crystal orientation no acess to a scattering intensity as function of energy I(ω) at fixed $\mathbf{Q}$ or I($\mathbf{Q}$) at fixed ω is given.

The use of three-axis spectrometers, developed originally by Brockhouse [Bro60], overcomes this disadvantage. On a three-axis spectrometer, the energy and wave vector of the incident neutron are selected from the white beam by a first Bragg reflection on a

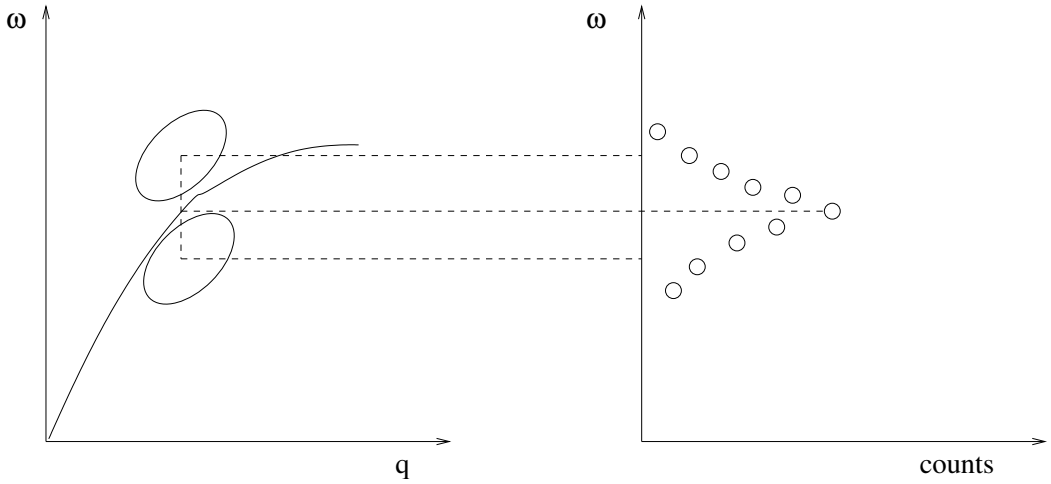

Figure 6.2: Measurement of a phonon $(\mathbf{q}, \omega)$ in a $\mathbf{q}$-constant mode. The ellipse shows the resolution function of the spectrometer.

monochromator (first axis, angle θ_M; see Figure (6.1)). They will then interact with the sample and will be scattered in a direction (second axis, angle ψ, defining the wave vector direction of the scattered neutrons) along which a second crystal, called the analyser, is placed to select the energy by another Bragg reflection (third axis, angle θ_A). Finally the neutrons are detected by a detector. The momentum transfer is chosen by rotating the sample and the analyser to get the good exit wave vector direction and length. One point in the $(\mathbf{q}, \omega)$ space corresponds to each configuration of the spectrometer, that is the angles θ_M, θ_A and ψ of the three axes. The idea is to scan the $(\mathbf{q}, \omega)$ space using different configurations of the spectrometer; when a given point $(\mathbf{q}, \omega_j)$ verifies the dispersion relation $\omega = \omega_j(\mathbf{q})$ of the crystal, the number of counted neutrons will substantially increase.

Either $\mathbf{Q}$-constant or ω-constant scans are made depending on the slope of the dispersion curve at the measured point (Figure 6.2). Strictly speaking, because of the mosaicity spreads of the sample itself, the monochromator and the analyser, the scattering won't occur at a point but rather on a volume centred on $(\mathbf{q}, \omega_j)$. If a neutron is detected, it has a probability $R(d\mathbf{q}, d\omega)$ to have in reality a transfer $(\mathbf{q} + d\mathbf{q}, \omega_j + d\omega)$. $R(d\mathbf{q}, d\omega)$ is called the *resolution function* of the spectrometer. The measured signal is the convolution of the inelastic scattering cross section by the resolution function of the spectrometer. See [Shi06] for further details.

Chapter 7

Lattice dynamics in Ni_2MnAl

This chapter is devoted to normal modes of vibration in Ni_2MnAl. Experimental details of the inelastic neutron scattering measurements are first reported. Phonon dispersions of two different crystals and their temperature dependence are discussed together with the from literature reported ab-initio phonon calculations. Finally, we focus on the temperature and composition dependence of the anomalous phonon softening observed in the $TA_2[\xi\xi 0]$ phonon branch. The measured data are discussed and compared to the data of other Ni-based systems reported in literature.

7.1 Experiment

Normal modes of vibration in Ni_2MnAl have been measured by inelastic neutron scattering using different three-axis spectrometers: 2T1 at the Orphée reactor of the Laboratoire Léon Brillouin (LLB), IN3 at the Institut Laue Langevin in Grenoble and PUMA at the Forschungsneutronenquelle Heinz Maier-Leibnitz in Garching.
Two crystals of different compositions, $Ni_{51}Mn_{18}Al_{31}$ and $Ni_{53}Mn_{22}Al_{25}$, have been measured. To retain the B2 atomic ordering at low temperature, the samples have been solution annealed in fused quartz tubes with argon atmosphere at 1273 K during three days and subsequently water quenched. To check for the effect of long-time aging on lattice dynamics, a third sample with the composition $Ni_{51}Mn_{18}Al_{31}$ which has been annealed for 45 days at 670 K, has been measured.
To access the $TA_2[\xi\xi 0]$ acoustic phonon branch with the polarisation $\{1\bar{1}0\}$, the samples have been oriented to have the (001) plane coincide with the scattering plane (Fig. 7.1). However a repositioning of the $Ni_{51}Mn_{18}Al_{31}$ sample within the (110) scattering plane was necessary to measure the phonon dispersions in the $[\xi\xi\xi]$ direction. The crystals were aligned by tilting using a two-axis goniometer. Phonon measurements have been mainly performed in the constant-k_f mode using a pyrolytic graphite Pg(002) or Pg(006) analyser when a better resolution was required. However a part of the measurement has been performed in the constant-k_i mode using a Pg(002) or Cu(220) monochromator which was used successfully for the first-time on PUMA during one of these measurements. Scans have been performed either in the constant-$\hbar\omega$ mode or constant-$\mathbf{Q}$ mode depending on the position of the resolution ellipsoid on the dispersion curve at the measured ($\mathbf{Q}$, ω) point.

The high temperature measurements have been performed with the samples mounted on a niobium holder in a vacuum furnace. Measurements below room temperature have been performed with the sample mounted in an aluminum container under helium atmosphere attached to the cold head of a closed-cycle cryostat. The temperature value was stable within $\pm 1K$ during the measurements.

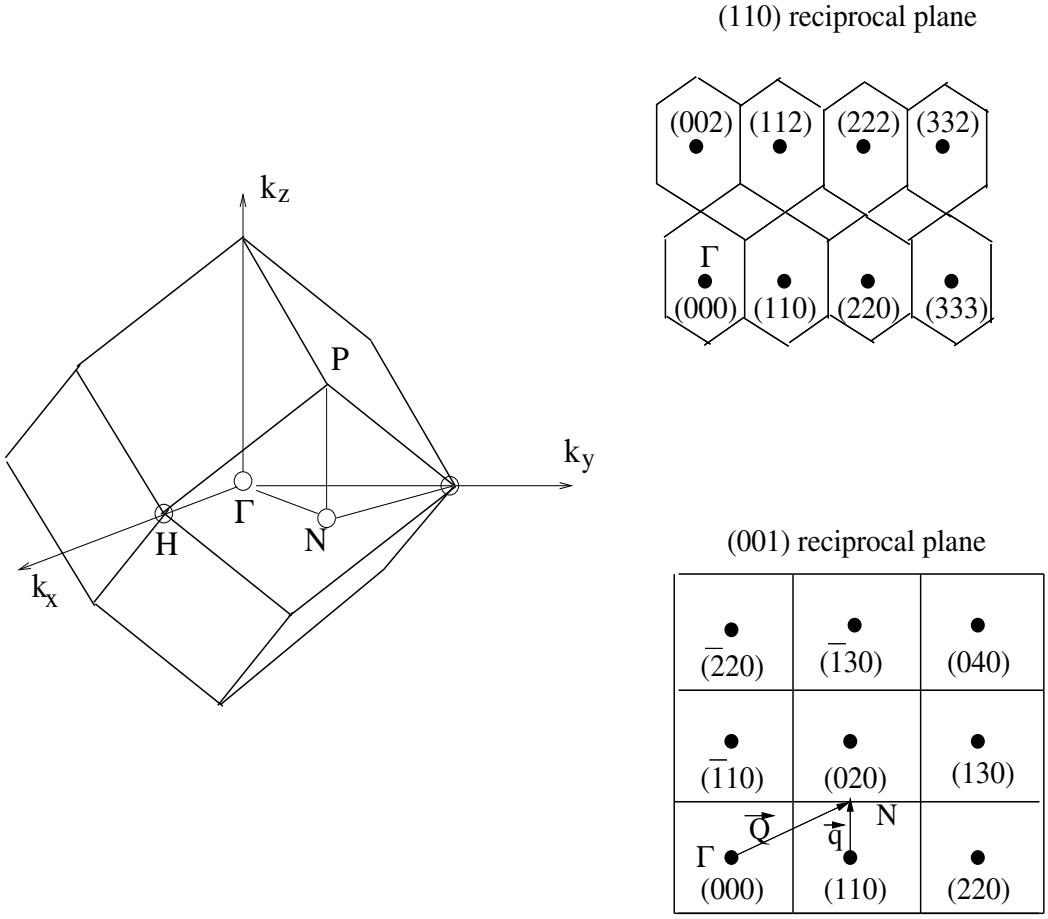

Figure 7.1: Brillouin zone for bcc structure along with the (110) and (001) scattering planes investigated during the neutron measurements.

7.2 Phonon dispersions in Ni_2MnAl

Phonon frequencies in $Ni_{51}Mn_{18}Al_{31}$ have been measured along the high symmetry directions: $[\xi 00]$, $[\xi\xi 0]$ and $[\xi\xi\xi]$ in the B2 ordered phase at 298 K. Dispersion curves have been fitted to the measured phonon frequencies ($\omega(\mathbf{q})$) using the program *Genax* based on the harmonic approximation within the Born–von Kármán (BVK) model [Leh62]. This force constant model assumes that the potential energy of the crystal is a sum of spherical two-body potentials taken over all the pairs of atoms. In the axial force model, the interaction between any two atoms at any distance from each other is reduced to two force constants, one longitudinal and one isotropic transverse. The appropriate number of neighbour shells

is found by trial: the maximum radius of considered neighbors is increased until the fit quality converges. In order do describe the phonon dispersion of $Ni_{51}Mn_{18}Al_{31}$ adequately, five nearest-neighbour shells have been taken into account.
The phonon dispersion curves are depicted in Fig. 7.2. As the unit cell of the B2 structure contains two atoms, there are six phonon branches, three acoustic and three optical. The acoustic and optical branches are separated by a gap between 5.6 and 6.5 THz. The transverse branches are doubly degenerated along the [ξ00] and [$\xi\xi\xi$] directions, a common point to cubic systems. The most important features of the dispersion are the kink observed in the TA_2[$\xi\xi$0] phonon branch in the q-range 0.1–0.25 r.l.u and the small dip in the LA[$\xi\xi\xi$]. The latter is related to the bcc structure and has already been revealed especially in group III and IV bcc metals and Cu-based shape memory alloys [Pet91a, Pet91b, Nic00, Man99]. However, the temperature dependence of this branch did not reveal any anomalous behaviour. A normal softening with increasing temperatures has been observed (Fig. 7.3).

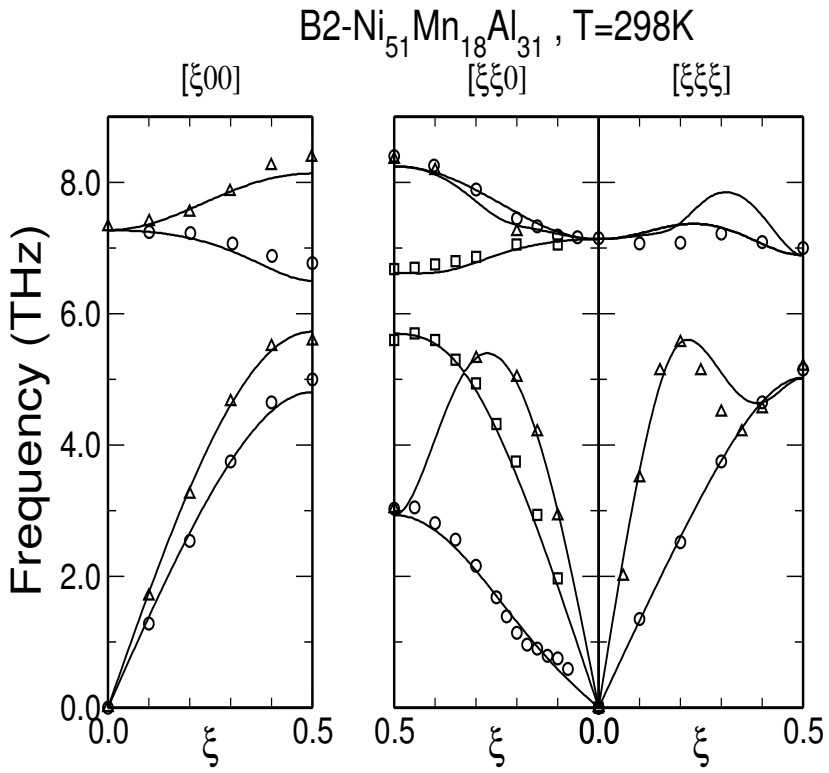

Figure 7.2: Phonon dispersion curves of B2-$Ni_{51}Mn_{18}Al_{31}$ in [ξ00],[$\xi\xi$0] and [$\xi\xi\xi$] directions at 298 K. The solid lines indicate dispersion curves determined by fitting the force constants from the Born-von Kármán model to the experimental data.

shell	pairs	f_l	f_t
1	Ni-Mn/Al[1]	31046.60	743.26
2	Ni-Ni[2]	1036.14	1352.89
3	Al-Al[2]	11187.00	-1414.67
4	Ni-Ni[3]	5327.01	-1782.01
5	Al-Al[3]	550.97	0.00
6	Ni-Al/Mn[4]	-382.83	-200.00
7	Ni-Ni[5]	310.39	0.00
8	Al-Al[5]	2546.28	0.00

Table 7.1: Longitudinal (f_l) and transverse (f_t) force constants (in dyn/cm) determined by fitting the BVK model to measured phonon frequencies in B2-$Ni_{51}Mn_{18}Al_{31}$ at 298 K. The notation A-B^n indicates nth neighbour A-B pairs.

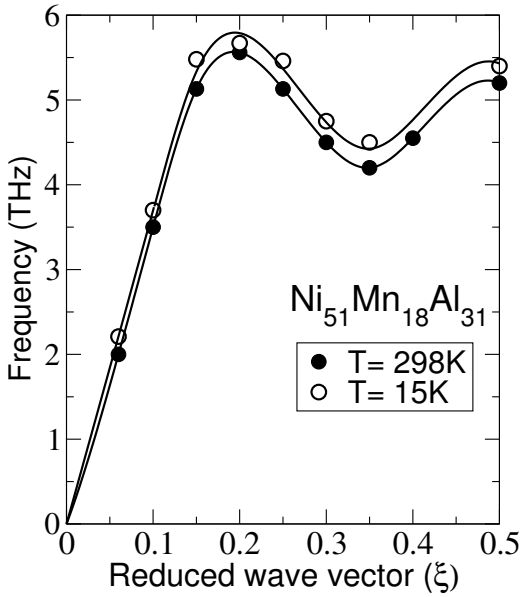

Figure 7.3: Temperature dependence of the LA[ξξξ] measured in $Ni_{51}Mn_{18}Al_{31}$ at 298 K and at 15 K. The solid lines are guide for eyes. Note the normal softening with increasing temperature.

Phonon frequencies in $Ni_{53}Mn_{22}Al_{25}$ have been measured along the high symmetry directions: [ξ00] and [ξξ0] in the B2 ordered phase at 298 K. The sample was oriented to have the (001) plane coincide with the scattering plane. Thus neither the TA_1[ξξ0] nor dispersion curves along the [ξξξ] direction could be measured. The measured phonon dispersions in $Ni_{53}Mn_{22}Al_{25}$ look very similar to those of $Ni_{51}Al_{31}Mn_{18}$. The kink in the TA_2[ξξ0] phonon branch in the q-range 0.1–0.25 r.l.u is also seen.
Using the atomic force constants obtained from the BVK fits, the total and the partial phonon DOS $g(\omega)$ in $Ni_{51}Al_{31}Mn_{18}$ are obtained from the dispersion relations $\omega_s(\mathbf{q})$ by integration over the first Brillouin zone using the method first proposed by Gilat and Raubenheimer [Gil66]. The phonon DOS plot (Fig. 7.5) reflects the typical features of the phonon dispersion curves with a gap between 5.6 and 6.5 THz showing a clear separation between the acoustic and optical modes as well as a cut-off frequency of 8.4 THz. The low frequency part of the density of states consists mostly of the contribution of the

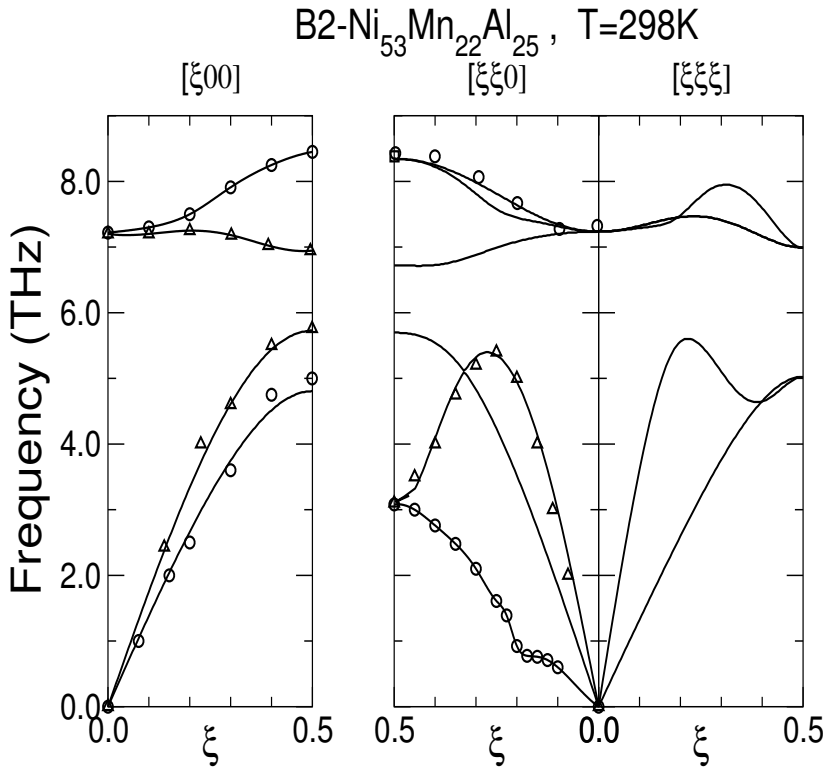

Figure 7.4: Phonon dispersion curves of B2- $Ni_{53}Mn_{22}Al_{25}$ in [ξ00] and [ξξ0] directions at 298 K. The solid lines are guide for eyes. The phonons in [ξξξ] have not been measured. The lines display the result of the Born-von Kármán fit in $Ni_{51}Mn_{18}Al_{31}$ for comparison.

heavier atoms (Ni, dashed curve), while the contribution of the lighter atoms (Al/Mn, dotted curve) appears dominantly at the uppermost frequency range above 6.5 THz. This sustains a normal behaviour of the different atomic species contributing to the total DOS contrary to the predictions of first-principle calculations in Ni-based unstable Heusler systems [Ent06b]. No inversion of optical modes is seen.

From the phonon DOS, we have calculated the specific heat per atom, the average vibration entropy per atom and the Debye temperature within the harmonic approximation using Eq. 5.40, Eq. 5.42 and 5.46 respectively [Kri69, Kit76]. These values are summarised together in Table 7.2. Note that the vibrational entropy in Ni_2MnAl is twice smaller than in Cu-based systems such as CuMnAl. This comes mainly from the low-lying TA_2[ξξ0] phonons in CuMnAl in which the phonon frequency is in the order of 1 THz at the zone boundary in comparison to 3 THz in Ni_2MnAl [Nic00].

The slopes of the phonon branches in the [ξξ0] direction at the center of the Brillouin zone give access to the sound velocities and some elastic constants. The relations between

$C_V(k_B)$	θ_D (K)	$S_v(k_B)$	$\langle u^2\rangle_{Mn/Al}(\mathring{A}^2)$	$\langle u^2\rangle_{Ni}(\mathring{A}^2)$
2.78	372	3.55	0.0070	0.0024

Table 7.2: Thermodynamic properties calculated from the phonon density of states of $Ni_{51}Mn_{18}Al_{31}$at room temperature. S_V refers to the vibrational entropy per atom, θ_D to Debye temperature, C_V to specific heat per atom and $\langle u^2\rangle$ to the mean square displacements.

sample	Method	C_{44}	C_L	$C^{'}$
$Ni_{51}Al_{31}Mn_{18}$	INS	105±8	265±8	15±8
$Ni_{53}Al_{25}Mn_{22}$	INS	-	258±8	10±8
$Ni_{54}Al_{23}Mn_{23}$	INS	103±5	259±5	16±5
$Ni_{54}Al_{23}Mn_{23}$	UM	111±2	253±3	21±4
$Ni_{50}Al_{25}Mn_{25}$	*ab-initio*	102	263	32

Table 7.3: Elastic constants in Ni_2MnAl obtained from different methods: from the initial slopes of the acoustic phonon branches at $\xi \rightarrow 0$ at room temperature (INS), from ultrasonic measurements (UM) and from first-principle calculations (*ab-initio*) [Bue04]. The data for $Ni_{54}Mn_{23}Al_{23}$ are taken from [Moy06a].

the sound velocities and elastic constants for cubic crystals are:

$$C^{'} = \frac{1}{2}(C_{11} - C_{12}) = \rho v_{TA_2}^2 \tag{7.1}$$

$$C_L = \frac{1}{2}(C_{11} + C_{12} + 2C_{44}) = \rho v_L^2 \tag{7.2}$$

$$C_{44} = \rho v_{TA_1}^2 \tag{7.3}$$

The elastic constants at room temperature obtained from the initial slopes of the acoustic phonon branches at $\xi \rightarrow 0$ are summarized in Table 7.3. The measured values in $Ni_{51}Mn_{18}Al_{31}$ and $Ni_{53}Mn_{22}Al_{25}$ are compared to elastic constants of $Ni_{54}Mn_{23}Al_{23}$ deduced from inelastic neutron scattering as well [Moy06a]. First principle calculations of lattice dynamics have provided theoretical values at 0 K for the elastic constants of the stoichiometric $Ni_{50}Mn_{25}Al_{25}$ compound [Bue04]. The measured and the calculated values in different samples are in good agreement, except for $C^{'}$ which corresponds to the initial slope of the $TA_2[\xi\xi 0]$ branch. While it is not expected that C_L and C_{44} strongly depend on composition, $C^{'}$ may change from one composition to another. In addition, it is worth noticing that the values extracted from the phonon dispersion curves are affected by a large error bar due to difficulty in defining the initial slope of the curve.

Recently Moya *et al.* [Moy06b] have used ultrasonic methods to determine the elastic constants of a Ni-Mn-Al Heusler alloy over a broad temperature range. The room temperature values are in excellent agreement with the values obtained from the slopes of the phonon dispersion curves. The low temperature bulk modulus agrees well with the reported value for antiferromagnetic $Ni_{50}Al_{25}Mn_{25}$ from *ab-initio* calculations. Anomalous softening of $C^{'}$ has been observed [Moy06b]. Besides, a deviation from Debye behaviour

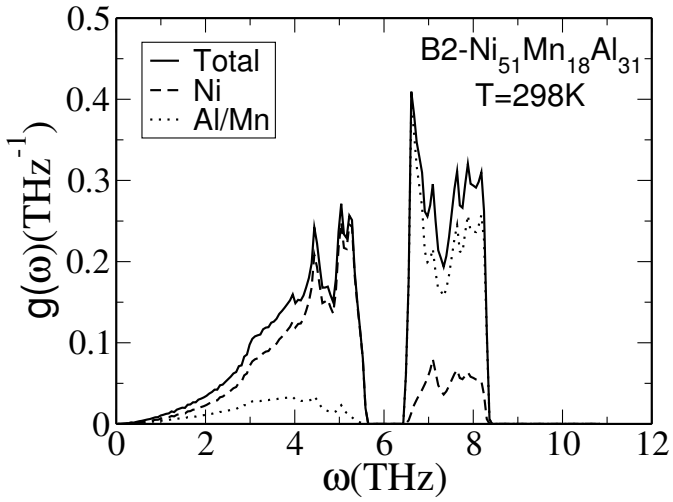

Figure 7.5: Total and partial phonon densities of states in $Ni_{51}Mn_{18}Al_{31}$ calculated from the Born–von Kármán force constants. Note the normal contribution of the different atomic species. Namely, the low frequency part of the density of states consists mostly of the contribution of the heavier atoms (Ni, dashed curve), while the contribution of the lighter atoms (Al/Mn, dotted curve) appears dominantly at the uppermost frequency range above 6.5 THz.

has been observed below the magnetic transition for all modes. Such a softening of the lattice is a result of magneto-elastic coupling. Elastic constant measurements under magnetic field indicate the existence of an anisotropic magneto-elastic coupling. Such a coupling saturates at about 5 kOe for all modes, and is associated with the non-linear behaviour at low fields exhibited by the magnetic field dependence of the magnetisation.

7.3 *ab-initio* phonons in Heusler Ni_2MnAl

Particular effort has been devoted to calculate the lattice dynamics by *ab-initio* methods of the Ni-Mn-Al system over a broad range of composition [Bue04]. Büsgen *et al.* have used the Vienna *ab-initio* simulation package [Kre96, Kre99] (VASP) to perform the first-principle calculations of the phonon dispersions along the [$\xi\xi$0] direction. The projector-augmented wave formalism implemented in this package [Kre99, Blo94] leads to very accurate results comparable to other all-electron methods. The electronic exchange and correlation are treated within density functional theory by using the generalised gradient approximation [Per96].

Phonon dispersions along [$\xi\xi$0] were calculated from first principles for Ni_2MnAl in the $L2_1$ structure with the lattice constant a=5.7 $\mathring{A}$. The supercell was a 1×5×1 periodic supercell based on the conventional tetragonal cell with lattice parameters $a_t = b_t = a/\sqrt{2}$, $c_t = a$. This is an orthorhombic supercell with the long axis along [$\xi\xi$0], containing ten consecutive (110) atomic planes along the [$\xi\xi$0] direction. The forces acting on the atoms within the supercell using the Hellmann-Feynman theorem. From these results, the force constant matrix within the harmonic approximation is constructed. The phonon frequencies and corresponding eigenvectors were obtained by diagonalising the corresponding dynamical matrix.

The calculated phonon dispersions of Ni_2MnAl in the theoretical cubic $L2_1$ structures are shown in Fig. 7.6. The [$\xi\xi$0] dispersions of the $L2_1$ structure have one set of non-degenerate acoustic branches LA, TA_1, and TA_2 and three optical branches that can be easily recognised in Fig. 7.6. The TA_2 branch is unstable in the ξ range 0.2–0.4. The optical modes are split into three well-separated groups which are triply degenerate at the Γ point, but become more mixed with increasing wave vector. In each of these three groups one finds dominating vibrations of a particular kind of atom. Mostly, this is due to the differences in the atomic masses and it can nicely be established by computing the partial phonon density of states.

These first-principle phonon calculations have been extended to other Heusler compounds with different magnetic order [Zay05]. The results show that the TA_2[$\xi\xi$0] phonon branch is unstable for some range of ξ in many systems such as Ni_2Mn(Ga,In,Ge) and Ni_2TiGa. In addition, for Ni_2MnGe the TA_2[$\xi\xi$0] phonon branch has a negative slope at the Γ point, indicating a pure elastic instability. The instability of the $L2_1$ structure in the non-magnetic Ni_2TiGa shows that magnetic order is not a necessary condition for phonon softening. The calculated phonon density of states is depicted in Fig. 7.7 for two selected systems: unstable Ni_2MnGa (with the TA_2 anomaly) and the stable Co_2MnGe (without any phonon anomaly). Comparison of these two plots shows that the position of the Ni peak in the case of the unstable compound Ni_2MnGa is different from the position of the Co peak in the stable system Co_2MnGe. This was unexpected, because atoms of Ni and Co, in both compounds occupy the same sites in the structure and their masses are close to each other. Thus, the sequence of the optical modes should be similar. However, while in case of the stable compound Co_2MnGe the sequence of the optical modes is normal,

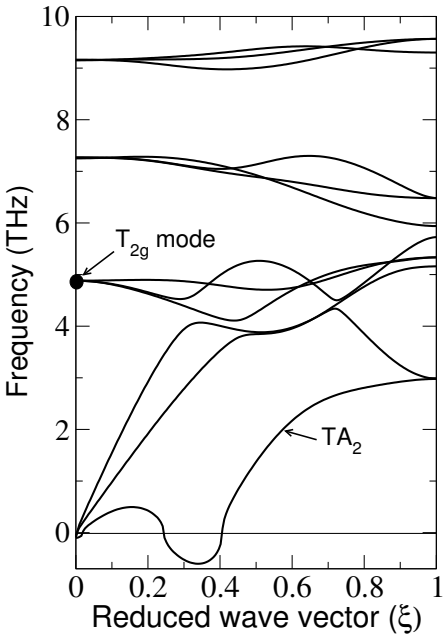

Figure 7.6: *ab-initio* phonon dispersion in [ξξ0] direction of Heusler Ni_2AlMn in the $L2_1$ structure [Bue04]. Imaginary frequencies of unstable $TA_2[\xi\xi0]$ modes are shown in the real negative frequency range. The frequency of the optical mode T_{2g} at the Γ-point is marked with a black dot.

for the case of Ni_2MnGa we observe an inversion of the optical modes.

Furthermore, a systematic review of the phonon dispersions revealed a characteristic behaviour of the optical T_{2g} mode at the Γ point Fig. 7.6. It was found in all Ni-based systems that this mode appears at much lower energies as compared to the Co-based stable compounds. Based on this results it was stated that the role of this anomaly might be as important as the instability of the TA_2 mode, or in other words, these two features have to be considered together in order to explain the structural instabilities in Heusler alloys. In fact, we must keep in mind that phonon modes of the same symmetry must repel each other. This is what must happen in the case of the TA_2 and the T_{2g} modes. At finite wave vectors only one optical mode which has $\{1\bar{1}0\}$ polarisation will repel the TA_2 mode. The main point is that there are two instabilities in the system. One of them is that the 110 planes in the Heusler structure can slide in the $[1\bar{1}0]$ direction; this is the TA_2 mode. But at the same time the (111) planes of Ni slide against each other also along the same $[1\bar{1}0]$ direction, and this is the T_{2g} mode. These vibrations are destructive for each other and have to repel. Thus, the TA_2 mode is unstable because it is pushed down by the from symmetry corresponding optical T_{2g} mode of Ni. The Fermi surface nesting determines at which wave vector the TA_2 mode is most sensitive to the influence of the optical mode.

According to these *ab-initio* calculations, it was thought that this acoustic-optical interaction might be of more general interest then just for the Heusler compounds. Its role in the martensitic transformation has to be investigated in more detail, including those in binary alloys. However, we will show in the next sections that no experimental evidence of such acoustic-optical interaction is seen in B2-Ni_2MnAl. Indeed opposite temperature dependences have been observed for the acoustic $TA_2[\xi\xi0]$ and for the from symmetry corresponding $TO_2[\xi\xi0]$ phonon branches.

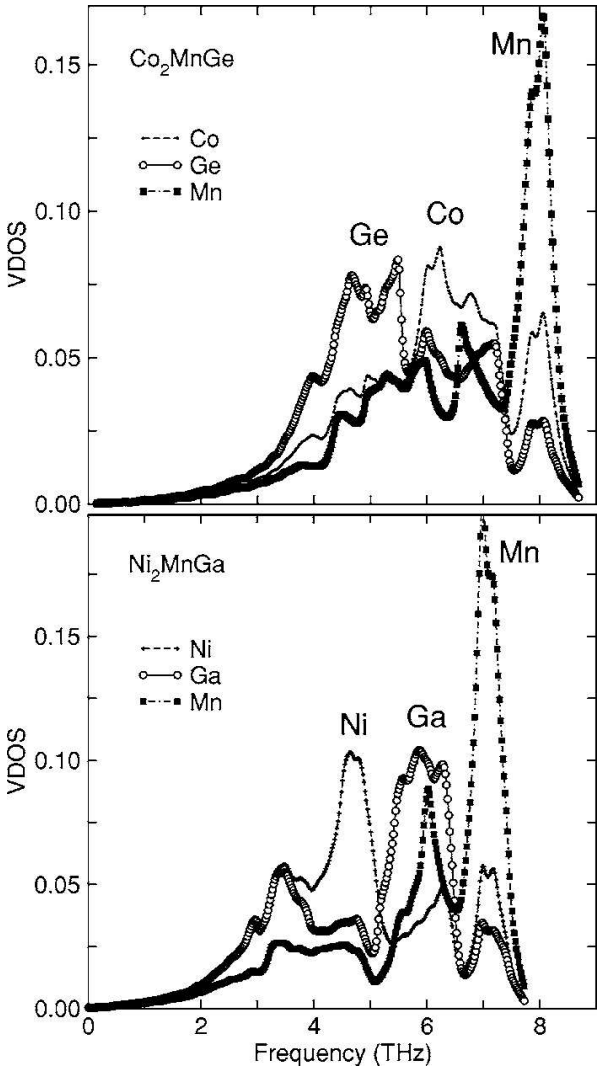

Figure 7.7: Partial phonon density of states taken from [Ent06b] showing the distribution of amplitudes of the atoms over the frequency range. This information shows which atom dominates in the vibrations of a given frequency range. In particular, the anomalous behaviour of optical vibrations of Ni lying at frequencies below those of the heavier Ga atom in unstable Ni_2MnGa is clearly visible. In the case of the stable system Co_2MnGe, the sequence of the optical modes is regular, *i.e.* increasing as the mass of the atom decreases.

7.4 Anomalous $TA_2[\xi\xi 0]$ phonon softening

Examples of $TA_2[\xi\xi 0]$ phonon spectra measured at room temperature in $Ni_{51}Mn_{18}Al_{31}$ are depicted in Fig. 7.8. The measured data are fitted with a damped harmonic oscillator (Eq. 6.7) yielding a damping Γ (FWHM) which does not show any anomalous behaviour in particular when compared to the damping observed in the bcc phase of the elementary systems Ti, Zr and Hf. The phonons are well defined over the whole ξ range. Fig. 7.9 shows the temperature dependence of Γ deduced from the fit of the $TA_2[\xi\xi 0]$ phonon measured in $Ni_{51}Mn_{18}Al_{31}$ at room temperature. An increase of the linewidth of the phonons is observed near the zone boundary presumably due to the superposition to the phonon signal to the incoherent scattering from the Ni arising from the peak of the DOS.

Acoustic phonons measured in $Ni_{51}Mn_{18}Al_{31}$ and in $Ni_{53}Mn_{22}Al_{25}$ at different temperatures are depicted in Fig. 7.10. Overall, the phonon frequencies of acoustic branches are comparable to those reported in an other Ni_2MnAl alloy with composition close to those of the crystals investigated here [Moy06a]. The phonon frequencies of the $TA_2[\xi\xi 0]$ branch measured in Ni_2MnAl show higher values compared to those in NiMnGa. This is consistent with the fact that the studied crystals do not transform martensitically within the studied temperature range. A general trend found from the phonon spectra is an overall lowering of the frequencies with increasing temperature presumably due to increasing anharmonicity. Contrary to the overall behaviour, the $TA_2[\xi\xi 0]$ phonon branch with the polarisation $\{1\bar{1}0\}$ shows an anomalous softening with decreasing temperature, associated with a wiggle in the q-range 0.1–0.25 r.l.u. This behaviour indicates low-restoring forces against the sliding of the (110) atomic planes in the $\langle 1\bar{1}0\rangle$ direction. Such displacements associated with atomic shuffles in the (110) planes constitute basal planes of the close-packed martensite low-temperature phase. In both samples, the wiggle deepens with decreasing temperature but does not result in any clear minimum down to 10 K as measured in the Heusler Ni_2MnGa [Zhe95]. The measured phonon behaviour agrees quite well with the prediction of recent *ab-initio* calculations [Bue04]. Based on density functional theory, Büsgen *et al.* calculated the phonon dispersion curves in Heusler $L2_1$-Ni_2MnAl in the $[\xi\xi 0]$ direction. They predicted a complete softening of the $TA_2[\xi\xi 0]$ branch in the range 0.25–0.4 r.l.u.. The extension of the phonon anomaly in q-space compares quite good considering that the lattice parameter of the $L2_1$ phase is twice higher than that of the B2 phase. As argued for Ni-Al [Sha91], the phonon dip for samples transforming to 3R never gets deep enough and the strain energy associated with this wave vector is not sufficiently large to induce a modulation in the low temperature martensite. Whether this argument holds for Ni_2MnAl can not be concluded here because both samples $Ni_{51}Mn_{18}Al_{31}$ and $Ni_{53}Mn_{25}Al_{22}$ did not transform martensitically down to 4 K.

The effect of the chemical composition on the phonon anomaly is seen on Fig. 7.11 where phonon frequencies of the $TA_2[\xi\xi 0]$ normalised to the zone boundary phonons are depicted. The phonon frequencies are smaller in $Ni_{53}Mn_{22}Al_{25}$ in comparison to $Ni_{51}Mn_{18}Al_{31}$. The difference is enhanced up to 15-20% in the q-range where the phonon anomaly is seen. This tendency has been predicted from *ab-initio* calculations in a similar Heusler compound Ni_2MnGa [Zay06].

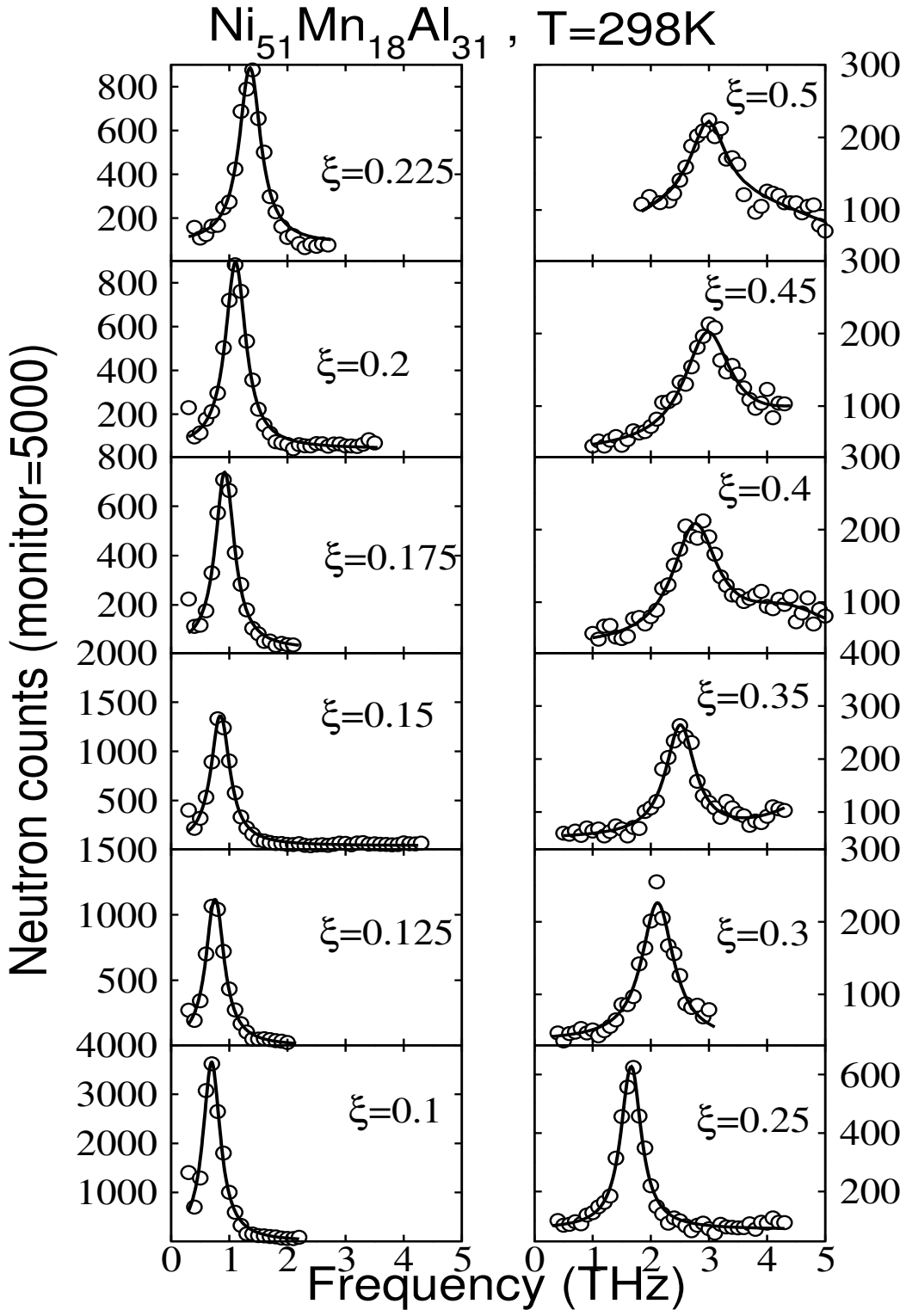

Figure 7.8: Phonon spectra of the $TA_2[\xi\xi 0]$ branch in $Ni_{51}Mn_{18}Al_{31}$ measured at 298 K. The spectra are normalised to the monitor count rate and fitted with a damped harmonic oscillator (solid lines). 5000 monitor counts correspond to about 45 seconds of counting time.

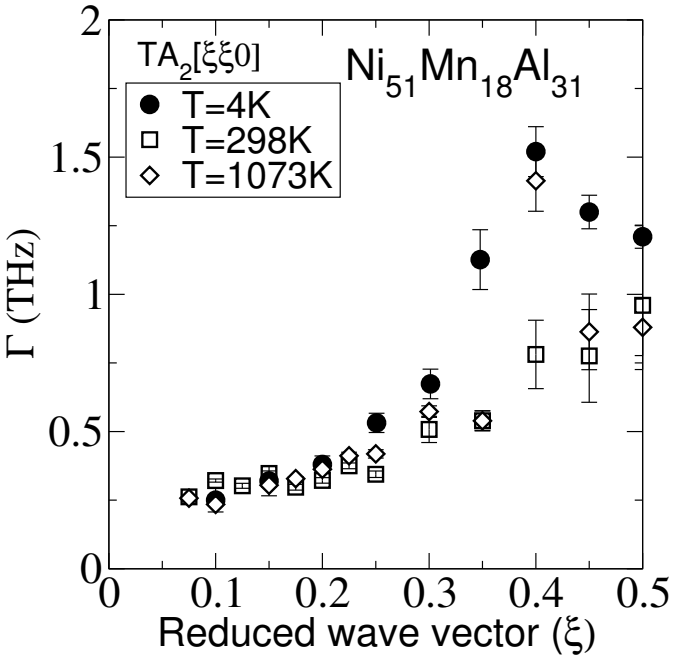

Figure 7.9: Temperature dependence of the damping Γ of the $TA_2[\xi\xi 0]$ phonon branch as measured in $Ni_{51}Mn_{18}Al_{31}$.

In fact, the first-principle calculations predict an increasing instability with increasing the valence electron number per atom (e/a) which is clearly evidenced by our measurements on $Ni_{51}Mn_{18}Al_{31}$ ($e/a = 7.29$) and $Ni_{53}Mn_{22}Al_{25}$ ($e/a = 7.59$). The composition dependence of the phonon anomaly in Ni_2MnAl parallels the behaviour reported for Ni-Al alloys [Sha91]. Namely smaller frequencies are observed for higher valence electrons per atom ratio. The electron-phonon coupling origin of phonon anomalies could be the same [1]. Furthermore, lattice dynamic investigations in five different NiAl single crystals, with a Ni content from 50 at.% to 63.9 at%, could reveal a shift in the q-position of the kink observed in the dispersion of the $TA_2[\xi\xi 0]$ phonon branch. The anomaly has been found to shift to smaller q-values with increasing Ni content *i.e.* the valence electron per atom ratio. Such behaviour could not be evidenced from our measurements on Ni_2MnAl.

Martensitic transformations, which are first order transitions, can be described by a modified Landau theory in which the average displacement of the atoms in the mode which causes the phase transition [Kru92] is the order parameter. A consequence of assumptions of this theory is that the frequency ω of this mode can be written as:

$$\omega^2 = a(T - T_M) \tag{7.4}$$

where a is constant and T_M is the temperature where the lattice would become dynamically unstable. The degree of softening is quantified by the temperature dependence of the

[1] Electronic structure calculations in NiAl and Ni_2MnGa reveal a Fermi surface nesting along the [110] direction at q-vectors corresponding to the position where the phonon anomalies are seen.

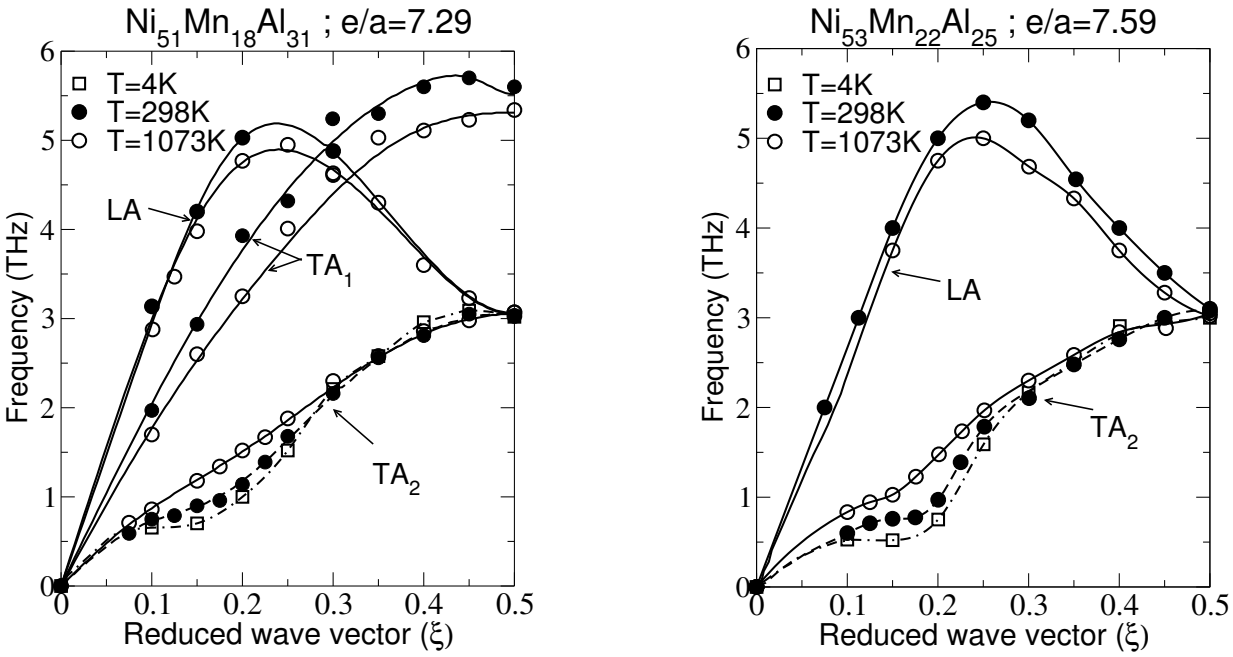

Figure 7.10: Temperature dependence of the acoustic phonon branches along the [110] direction in $Ni_{51}Al_{31}Mn_{18}$ (left, $e/a = 7.29$) and $Ni_{53}Mn_{22}Al_{25}$ (right, $e/a = 7.59$). Note the anomalous softening of the $TA_2[\xi\xi 0]$ phonons in the range 0.1–0.25 of ξ.

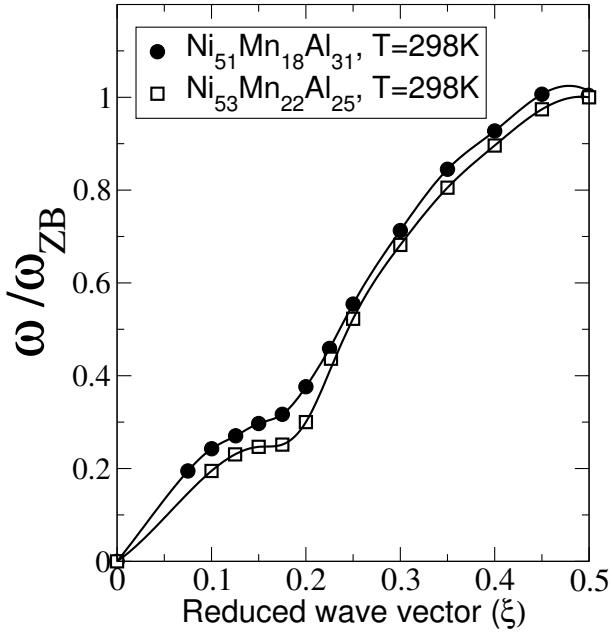

Figure 7.11: Phonon frequencies of the $TA_2[\xi\xi 0]$ normalised to the zone boundary phonon frequency ω_{ZB} measured at room temperature in $Ni_{51}Mn_{18}Al_{31}$ ($e/a = 7.29$) and in $Ni_{53}Mn_{22}Al_{25}$ ($e/a = 7.59$). The solid lines are guide to the eyes.

frequency squared of the soft phonon. An example of typical soft phonon modes $\xi = 0.15$ and $\xi = 0.2$ of the $TA_2[\xi\xi 0]$ branch in Ni_2MnAl upon cooling is depicted in Fig. 7.12.

The data of the different samples presented in Fig. 7.12 can be well fitted by equation 7.4 yielding different slopes for different ξ values. For the different chemical compositions the strongest softening is seen for $\xi = 0.2$. However due to the relatively broad region where the softening is observed in the dispersion of the $TA_2[\xi\xi 0]$ branch and to the absence of any clear minimum down to 4 K in all investigated crystals a precise determination of the soft mode wave vector is not possible. The investigated crystals order antiferromagnetically below 300 K. However no substantial change in the softening is seen below this temperature. The situation is different in Ni_2MnGa which orders ferromagnetically below 350 K where the softening is significantly enhanced in the ferromagnetic state as compared to the paramagnetic state [Stu97].

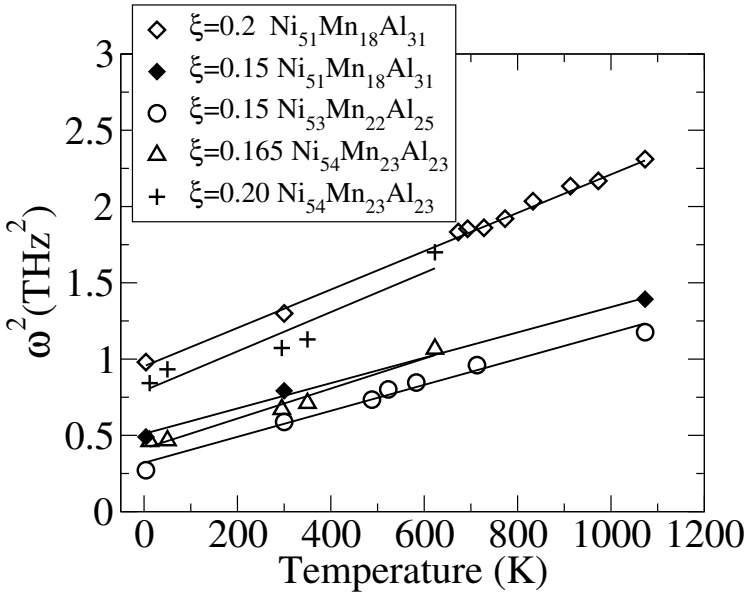

Figure 7.12: Temperature dependence of the frequency squared of the $TA_2[\xi\xi 0]$ phonon modes for typical ξ values measured in the two different crystals. The solid lines show the result of linear fits. The data of $Ni_{54}Mn_{23}Al_{23}$ are taken from [Moy06a].

In order to investigate the effect of the atomic ordering on the lattice dynamics, a $Ni_{51}Mn_{18}Al_{31}$ single crystal has been annealed in a quartz tube under argon atmosphere at 673 K during 45 days. Despite of the very long annealing time, neutron diffractions performed on the sample revealed a relatively weak $L2_1$ ordering. The order parameter was not exceeding 10%. Whether the missing single $L2_1$ phase is due to a too short annealing time or a metastable equilibrium between the B2 and the $L2_1$ phase is reached is unclear. The annealed $Ni_{51}Mn_{18}Al_{31}$ has been aligned to have its (001) plane coincide with the scattering plane to access the $TA_2[\xi\xi 0]$ phonon branch which has been measured at different temperatures. Fig. 7.13 displays the temperature dependence of the $TA_2[\xi\xi 0]$ phonon branch. Again a kink is observed in the ξ range 0.1–0.25 r.l.u which deepens with decreasing temperatures but does not result in any clear minimum down to 10 K. Despite of the weak $L2_1$ state of order, a comparison of the phonon frequencies of the as-quenched and the annealed sample reveals clear differences. This is clearly seen in Fig. 7.14 where the frequency squared of the $TA_2[\xi\xi 0]$ phonon modes for $\xi = 0.15$ and $\xi = 0.2$ in the two crystals are reported as function of temperature. The degree of softening is slightly smaller in the annealed sample for temperatures below 673 K but changes substantially

above this temperature which is slightly below the B2→B2+$L2_1$ order-disorder transition temperature reported in literature (T_{OD}=700 K). Whereas the magnetic order of the retained metastable B2 phase of Ni_2MnAl is well known to be conical antiferromagnetic [Zie75], the magnetic state of the $L2_1$ phase has been an issue that has not been fully clarified basically because of difficulty in stabilising a single $L2_1$ phase. Based on magnetisation measurement in field cooled and zero field cooled, it was shown that although a single $L2_1$ phase is not readily stabilised, but rather a mixed $L2_1$+B2 state occurs which incorporates ferromagnetic and antifferomagnetic parts for which close lying Curie and Néel temperatures can be identified from magnetisation measurements [Ace02].

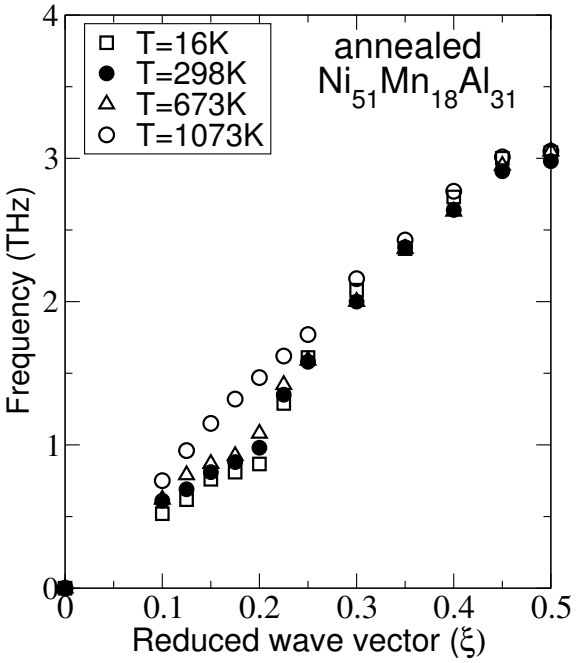

Figure 7.13: Temperature dependence of the $TA_2[\xi\xi 0]$ phonon frequencies measured in the annealed $Ni_{51}Mn_{18}Al_{31}$ crystal.

Whether the effect of long-time annealing on the phonon frequencies of the $TA_2[\xi\xi 0]$ phonon branch is due to the atomic ordering itself or to the induced magnetism in the sample can not be concluded here. As reported above, it was shown in Ni_2MnGa that the magnetism significantly affects the degree of the $TA_2[\xi\xi 0]$ phonon softening. An other possible explanation of the effect of the annealing on the phonon frequencies may lie in the formation of precipitates within the B2+ $L2_1$ matrix due to the very long aging time. Differential scanning calorimetry measurement on Ni_2MnAl samples revealed a strong influence of the aging time on the transitional behaviour of Ni_2MnAl samples (see section 3.4). Formation of precipitates may lead to changes in the valence electron per atom ratio in the matrix for which the $TA_2[\xi\xi 0]$ phonons are sensitive as seen in Fig. 7.11.

Motivated by recent *ab-initio* phonon calculations in the Heusler $L2_1$-Ni_2MnAl which predicted that the phonon anomaly might not be restricted to acoustic modes only, the temperature dependence of the phonon dispersion of the acoustic $TA_2[\xi\xi 0]$ phonon branch has been extended to optical phonons with the same polarisation namely the $TO_2[\xi\xi 0]$

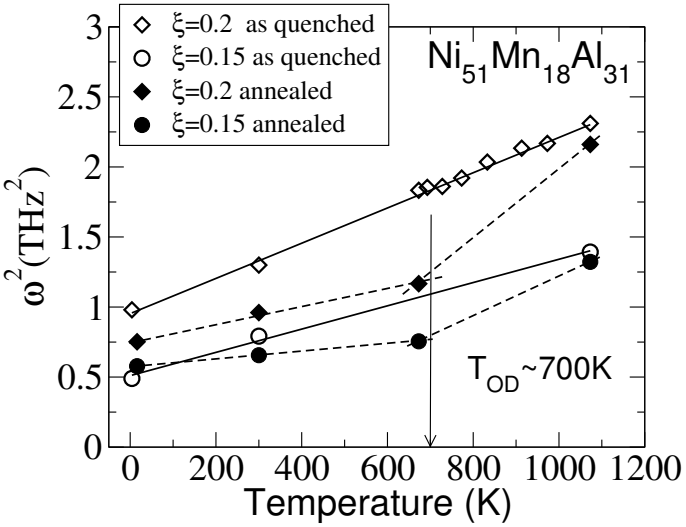

Figure 7.14: Temperature dependence of the frequency squared of the $TA_2[\xi\xi 0]$ phonon modes for $\xi = 0.15$ and $\xi = 0.20$ as measured in the as-quenched and in the annealed $Ni_{51}Mn_{18}Al_{31}$ crystals. The arrow shows the B2→B2+$L2_1$ order-disorder transition temperature as reported from literature [Kai00].

branch. The optical transverse mode with the same polarisation as the $TA_2[\xi\xi 0]$ has been measured for small q-values at room temperature and at 1073 K in $Ni_{51}Mn_{18}Al_{31}$. The measured phonons are depicted in Fig. 7.15. A normal softening with increasing temperature has been observed. This optical modes do not play an important role on the lattice instability as the acoustical modes in the B2 phase in contrary to the predictions of *ab-initio* calculations performed in Ni-based and Co-based Heusler alloys [Zay05]. Based on density functional theory, Zayak et al. have found that the $TA_2[\xi\xi 0]$ is unstable due to the repulsion from the symmetry corresponding optical mode called T_2g mode. No clear evidence of such behaviour is seen from our measurements. On the contrary, the measured acoustic and the optic phonons in B2- $Ni_{51}Mn_{18}Al_{31}$, with the polarisation $\{1\bar{1}0\}$, have opposite temperature dependence. However, one should keep in mind that the calculations have been performed in the ordered $L2_1$ Heusler structure. Whether this discrepancy is due to the atomic ordering or to the induced magnetic order can not be concluded here.

The optical phonon, in the long-time annealed sample, has been measured at the Γ-point (T_{2g} mode) from 1073 K down to 4 K. The measured data are depicted on Fig. 7.16. A normal decrease in the frequency with increasing temperature is seen, synonym of a normal temperature dependence due to anharmonicity.

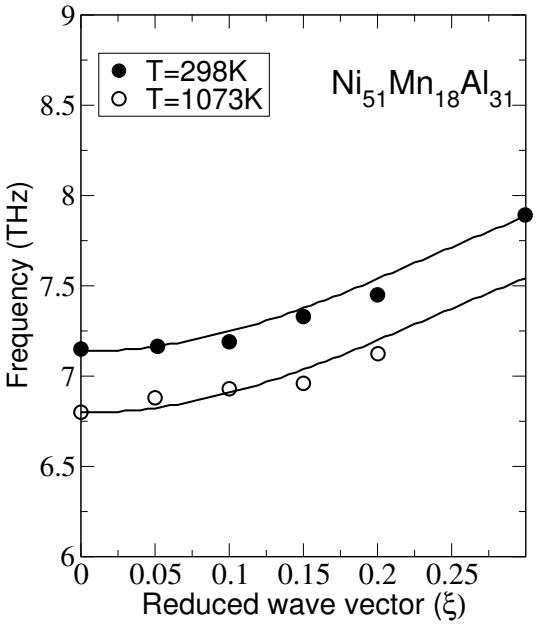

Figure 7.15: Temperature dependence of the $TO_2[\xi\xi 0]$ phonon modes in $Ni_{51}Mn_{18}Al_{31}$ measured at small q-values. Note the normal softening with increasing temperatures.

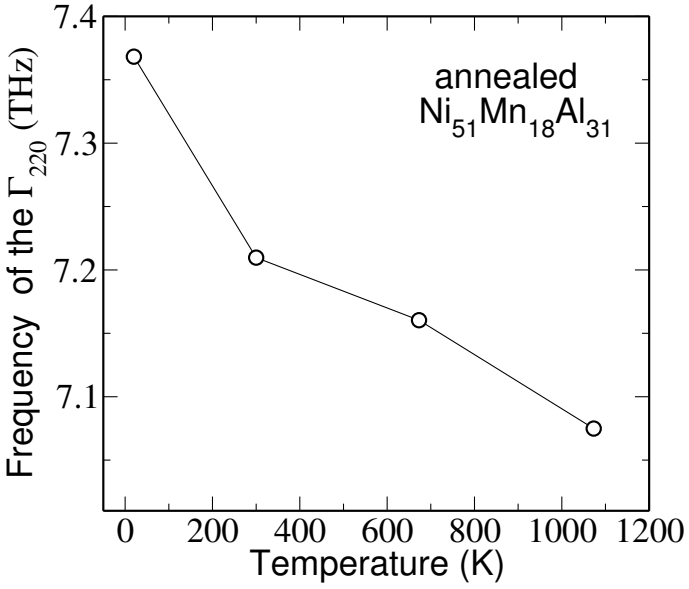

Figure 7.16: Temperature dependence of the optical zone center Γ mode (T_{2g}) in the annealed $Ni_{51}Mn_{18}Al_{31}$ crystal measured at the (220) reciprocal point. Note the normal softening with increasing temperatures. The line is a guide to the eye.

7.5 Elastic neutron scattering

Martensitic transitions are usually preceeded by pretransitional phenomena announcing that the system is preparing for a phase transition before it actually occurs [Bru81]. These are called *precursor effects*. Thermodynamic calculations discuss precursor effects in terms of local fluctuations into the low-temperature phase [Lin89, Lin90, Kru89]. In different systems, precursor take many different forms and are commonly observed as anomalous effects in x-ray, electron and neutron scattering measurements. The quasi-elastic "central peak" observed in neutron scattering refers to the appearance of elastic streaks and satellites, whose intensity increases as the transition is approached. It represents either static or rather long-lived fluctuations in position and is associated with existence of dips at specific wave vectors in the phonon dispersion curves.

A systematic check for the presence of any precursor effects in pure martensitic bcc metals has been performed by elastic neutron scattering on high quality single crystals. The measurements in pure Hf, Co, Zr, Ti, La, Sc, Cr, Ce did not reveal any additional diffuse scattering a the q-positions where the phonon anomalies are seen (see [Nic01] and references therein). However neutron scattering experiments on metal alloys have revealed such elastic precursors which are drastically increasing as the martensitic transition is approached [Sha89, Zhe95]. This marked difference in the behaviour of pure samples with respect to alloys suggests that the appearance of the central peak prior to the transformation in not generic to the martensitic phase transition. Rather it can be related to the appearance of intermediate phases or driven by point defects. Indeed, pure Zr crystals have been exposed to a constant air leak at high temperatures prior to the elastic scattering. This contamination resulted in a splitting of the (110) Bragg peak and in the appearance of additional peak at 0.98(110) [Hei91]. The authors demonstrated that these observations can be explained by the coexistence of α and β phases due to alloying with O or N. These observations on Zr alloyed by O and N have been latter completed by addition of Co or Nb to bcc Zr. In both alloys, additional diffuse elastic signal was found in q-positions where low-lying phonons have been observed. The diffuse scattering originates from static lattice displacements due to the misfit of the Nb atoms in the Zr matrix [Neu91]. The coincidence of the q-positions where the diffuse signal appears mostly with the low-lying phonons can be explained by the "*weakness*" of the lattice a these q-positions.

In Ni_2MnGa, the appearance of the central peak has been attributed to the occurrence of a structural phase transition prior to the martensitic phase transition (intermediate transition) to a micromodulated phase, which preserves the cubic symmetry, resulting from the freezing of ξ=0.33 $TA_2[\xi\xi 0]$ phonon mode. Such a phase transition has been evidenced by neutron scattering [Zhe95], x-ray [Fri94], electron microscopy [Ces97] and ultrasonic measurements [Wor96, Man97]. The dramatic increase in the intensity of the central peak and the increase the soft mode frequency below T_1=260 K confirm these observations. Based on a phenomenological model which includes a magnetoelastic coupling, it has been evidenced that the premartensitic transition must be considered as a magnetically driven precursor announcing the martensitic transition by the modification of the dynamical response of the parent bcc lattice [Pla97].

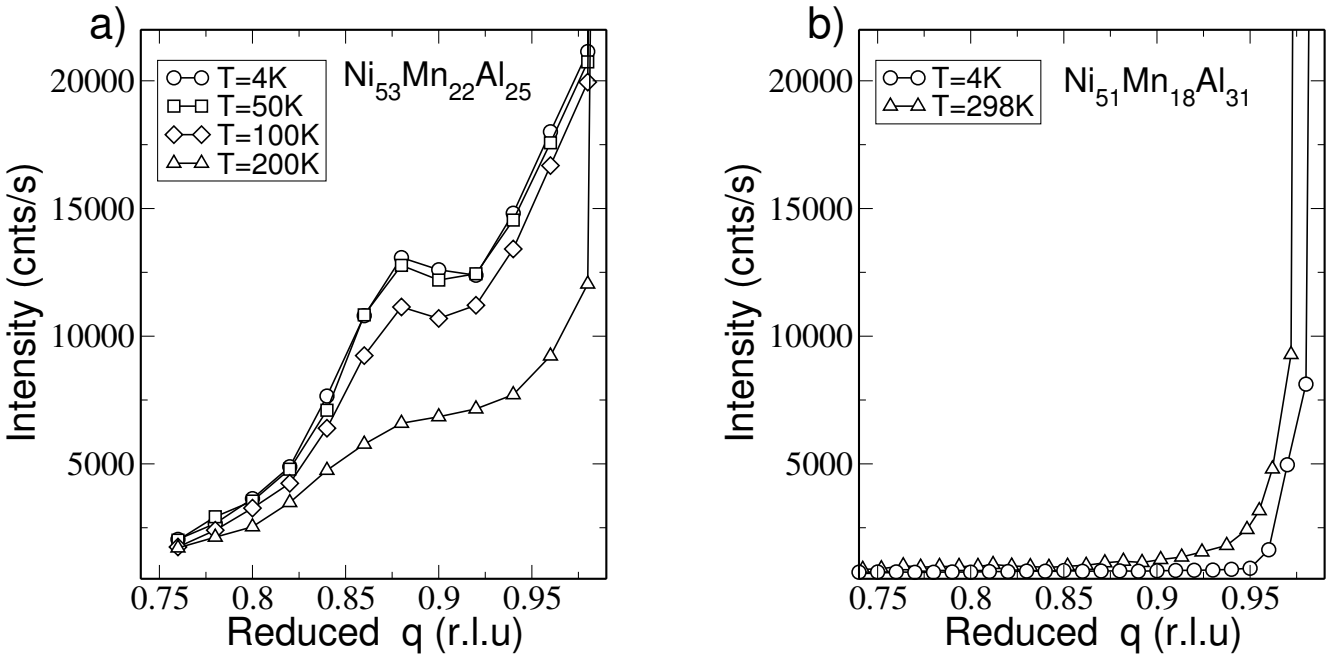

Figure 7.17: Temperature dependence of the elastic scattering along the $[\bar{1}10]$ direction starting from the (110) reflection measured in $Ni_{53}Mn_{22}Al_{25}$ (a) and in $Ni_{51}Mn_{18}Al_{31}$ (b).

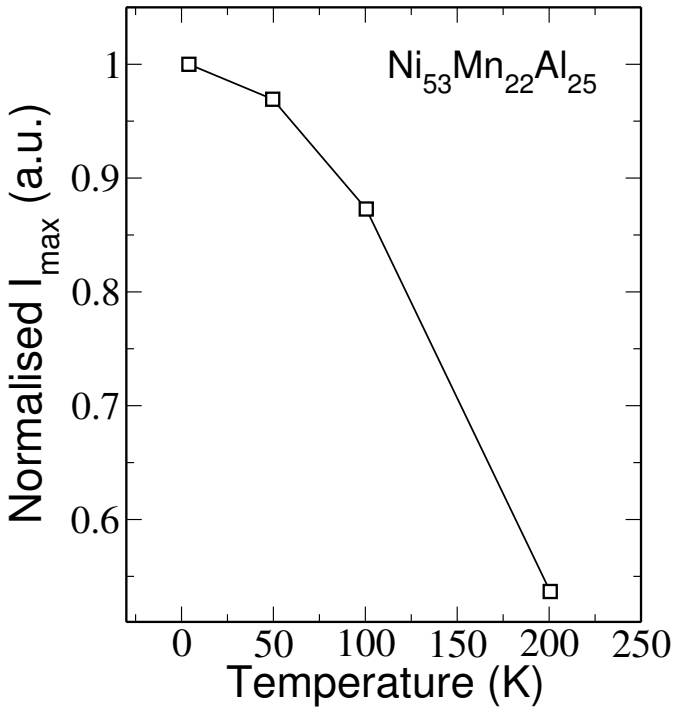

Figure 7.18: Temperature dependence of the normalised maximum intensity of the elastic signal measured $q = 0.875$ r.l.u ($\xi = 0.125$ r.l.u) in $Ni_{53}Mn_{22}Al_{25}$.

To check for the presence of such precursor effects in Ni_2MnAl, elastic neutron scattering has been performed on the two samples, $Ni_{51}Mn_{18}Al_{31}$ and $Ni_{53}Mn_{22}Al_{25}$. The (001) scattering plane has been scanned at different temperatures with longitudinal and transverse scans along $[1\bar{1}0]$ and [110] directions, respectively.

Elastic scattering has been measured starting from the fundamental reflection (110) along the $[\bar{1}10]$. Results in $Ni_{53}Mn_{22}Al_{25}$ are shown in Figure 7.17(a). As already observed in other Ni-based system, diffuse elastic scattering is observed. A diffuse intensity develops in the range 0.05-0.2 of ξ which corresponds to the position of the wiggle observed in the $TA_2[\xi\xi 0]$ phonon branch. The signal intensity increases with deceasing temperatures but does not develop in a sharp elastic peak down to 4 K. Fig. 7.18 shows the temperature dependence of the maximum intensity of the observed satellite normalised to the value at T=4 K. In addition to the satellite peak, there is an intense diffuse scattering that diverges as $\xi \rightarrow 0$. This scattering is a ridge or streak emanating from the (110) Brillouin zone center. The striking feature is that no diffuse elastic signal has been observed in $Ni_{51}Mn_{18}Al_{31}$ from 298 K down to 4 K (Fig. 7.17(b)).

Recently, neutron elastic scattering has been performed in $Ni_{54}Mn_{23}Al_{23}$ single crystal [Moy06a]. The measurements revealed two distinct satellite peaks, one associated to the anomalous dip in the $TA_2[\xi\xi 0]$ phonon branch and one attributed to an eventual splitting of the Bragg peak owing to a tetragonal distortion as reported in Ni_2MnGa from x-rays [Fri94] and neutron scattering [Stu97]. The difference in the behaviour of the different samples suggests that diffuse signal is due to Huang scattering arising from the local structural defects of the cubic lattice, characterised by the shear strain of the (110) planes along the $[1\bar{1}0]$ direction. This statement is consistent with the larger mosaic spread of $Ni_{53}Mn_{22}Al_{25}$ and with the linewidth (FWHM) of the diffuse elastic signal (0.1 r.l.u), one order of magnitude higher than that of the fundamental (110) reflexion (0.025 r.l.u). It was already considered that the central peak in shape memory systems is an extrinsic property attributed to crystal imperfections. Within this context, the theory proposed by Halperin and Varma [Hal76] appears to be relevant. It is based on the existence of defects that induce a force field on the undistorted lattice. The response to this field gives rise to a displacement field in the neighborhood of the defects.

The fact that no trace of elastic diffuse scattering has been measured in $Ni_{51}Mn_{18}Al_{31}$ suggests that the appearance of such satellite peaks are sample dependent and can be related to the inhomogeneity of the sample under study. This is consistent with the fact that the martensitic transition temperature in these alloy systems is extremely sensitive on composition, and therefore the existence of small amount of martensite growing as temperature decreases cannot be completely disregarded. Besides, a comparison of the electron per atom ratio and the phonon frequencies of the $TA_2[\xi\xi 0]$ phonon branch of the two samples might suggest that the $Ni_{53}Al_{22}Mn_{25}$ was measured in its pretransitional state.

7.6 Discussion

The existence of anomalous (with low energy) phonons at specific wave numbers on the $TA_2[\xi\xi 0]$ branch in materials exhibiting lattice instability can be related to the structure of the martensitic phase. It is important to recall that in order to achieve the adequate stacking sequence of the close-packed planes in the martensitic phase, intracell displacements called *shuffles* are necessary. As indicated in chapter 2, these displacements correspond to phonons on the $TA_2[\xi\xi 0]$ branch with specific wave numbers. The character of the phonon softening measured in Ni_2MnAl corresponds to the pattern of atomic displacements of the modulations 2M, 10M, 12M and 14M observed in bulk and thin-films. The reduced wave vector $\xi = 1/8$ represents a modulation with a period of 8 atomic planes (2M structure), while $\xi = 1/5$ characterises the 10M modulation. Finally, the 14M and the 12M modulations can be characterised by the reduced wave vectors $\xi = 1/7$ and $\xi = 1/6$, respectively, which also lie in the range between $\xi = 0.1$ and $\xi = 0.2$, *i.e.* where the anomalous phonon softening is seen. Due to the relatively broad region where the softening is observed in the dispersion of the $TA_2[\xi\xi 0]$ branch and to the absence of any clear minimum, precise determination of the soft mode wave vector is not possible. The wiggle observed in $TA_2[\xi\xi 0]$ phonon branch of Ni_2MnAl deepens when decreasing temperature but does not result in any clear minimum. The softening remains finite down to 4 K in both investigated samples. It has been argued for Ni-Al [Sha91] that the phonon dip for samples transforming to 3R never gets deep enough and the strain energy associated with this wave vector is not sufficiently large to induce a modulation in the low temperature martensite. Whether this arguments holds also for Ni_2MnAl can not be concluded here because both samples $Ni_{51}Mn_{18}Al_{31}$ and $Ni_{53}Mn_{25}Al_{22}$ did not transform martensitically down to 4 K. Besides, no change in the q-position of the phonon anomaly is seen with composition. It is interesting to mention that in Ni-Al alloys, the location of the dip moves from $\xi = 0.25$ in the case of stoichiometric NiAl to $\xi = 0.16$ for $Ni_{62.5}Al_{37.5}$. This change has been explained from first-principle calculations from which a linear relation of the dip position with the electron concentration is deduced [Zha92].

It is instructive to compare the $TA_2[\xi\xi 0]$ low-lying phonons measured in Ni_2MnAl to other Ni-based systems. In Fig. 7.19 we have plotted the absolute acoustic phonon frequencies in [110] direction of different Ni-based systems measured at room temperature. This representation enables a suitable comparison between different alloys. Contrary to Cu-based systems, in which it has been shown that the $TA_2[\xi\xi 0]$ curves are very flat over large parts of the Brillouin zone with similar energies (value at the zone boundary of approximately 1.2 THz) [Man93], Ni-based curves are marked by a systematic presence of a wiggle in the phonon dispersion at specific reduced wave vector ξ which is both system and chemical composition dependent. Contraty to the $TA_1[\xi\xi 0]$ and $LA[\xi\xi 0]$ branches which lie nearly on a unique curve for the different compounds, the $TA_2[\xi\xi 0]$ branch depends strongly on both composition and alloy system. We recall that these $TA_2[\xi\xi 0]$ phonon modes correspond to the sliding of the (110) atomic planes in the $\langle 1\bar{1}0 \rangle$ direction. Such displacements associated with atomic shuffles in the (110) planes constitute basal planes of the close-packed martensite in the low-temperature phase.

For most of the shape-memory alloys, the anomaly on the $TA_2[\xi\xi 0]$ branch becomes more pronounced as the alloys approaches the martensitic transition. This is not the case in Cu-based alloys; any phonon in the branch has a particular temperature dependence and the temperature softening in these alloys are small in comparison to that of other shape memory alloys. According to Landau theory of phase transitions, the frequency squared of the soft mode varies linearly with temperature, $\omega^2 = a(T - T_M)$. The squared frequency of the soft $TA_2[\xi\xi 0]$ phonons in different Ni-based alloy systems is given in Fig. 7.20 as function of temperature. The rate of change $d\omega^2/dT$ of the square of the frequency of the anomalous phonon is larger in Ni-based systems when compared to Cu-based systems [Nic00]. The significant distinction between these systems can probably explain their different pretransitional behaviour; in contrast to Ni-based systems, no trace of intermediate phase has been observed in Cu-based systems prior to the martensitic transition. A striking feature we see in Fig. 7.20 is the quite similar degree of softening in NiAl, Ni_2MnAl and paramagnetic Ni_2MnGa which becomes substantially enhanced when Ni_2MnGa orders in the ferrommagnetic state below $T_c = 350\ K$ [Stu97]. Actually in the paramagnetic phase, the rate $d\omega^2/dT$ is very similar to NiAl and Ni_2MnAl.

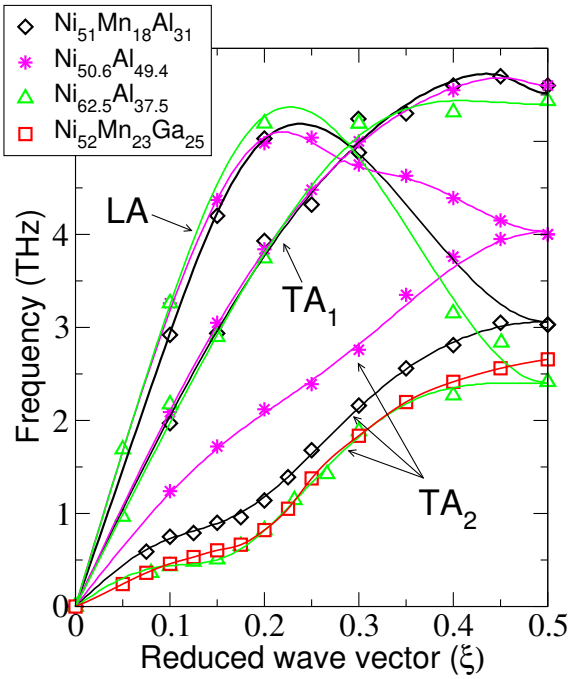

Figure 7.19: Acoustic phonon dispersion in $[\xi\xi 0]$ direction measured at room temperature in different Ni-based alloys. Note the strong dependence of the $TA_2[\xi\xi 0]$ on composition in comparison to the $TA_1[\xi\xi 0]$. The data of NiAl and NiMnGa are taken from [Sha91] and [Man01] respectively.

Despite of the fact that the investigated Ni_2MnAl samples order antiferromagnetically below 300 K, no substantial change in the degree of softening has been observed between the paramagnetic and the antiferromagnetic phases. It has been argued for Ni_2MnGa that the coincidence of the Curie temperature and the flexion point of the $d\omega^2/dT$ suggests that the magnetisation of the sample influences the phonon energy [Man01]. This can be described by introducing an additional term to the free energy of the system which contains a function of magnetisation. The occurrence of such a term is expected if magnetoelastic effects are considered. Recently, Moya *et al.* [Moy06b] have used ultrasonic methods to

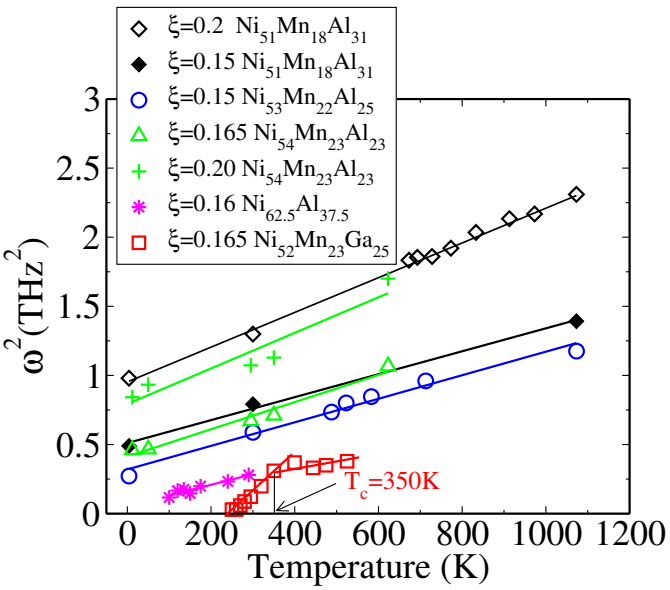

Figure 7.20: Temperature dependence of the frequency squared of the soft phonon $TA_2[\xi\xi 0]$ modes in different Ni-based alloys. Note the peculiar behaviour of Ni_2MnGa at the Curie temperature $T_c = 350\ K$.

determine the elastic constants of a Ni-Mn-Al Heusler alloy over a broad temperature range. Measurements under magnetic field, both isothermal and variable temperature, showed that the value of elastic constants depends on magnetic order, thus giving evidence for magnetoelastic coupling in this alloy system. The magnetoelastic coupling potential is expected to be proportional to the square of magnetisation M with $M \propto (1 - T/T_C)^{1/2}$, such an interaction would change the rate of the $d\omega^2/dT$, but not the linear behaviour. However, the magnetisation of the antiferromagnetically ordered Ni_2MnAl is smaller than that of the ferromagnetically ordered Ni_2MnGa. Thus the magnetoelastic coupling might be not enough to enhance the phonon softening in the antiferromagnetic state as seen from our measurements.

The degree of lattice instability in different systems can be quantified by the e/a dependence of the energy of the soft phonon mode. Fig. 7.21 shows the measured frequencies of the soft phonon mode $\xi = 0.175$ in Ni_2MnAl along with the as reported frequencies in the literature of other Ni-based systems *i.e.* NiAl and NiMnGa. The overall tendency is the decrease in the soft phonon frequency with increasing the valence electron per atom ratio. A linear fit of the data depicted in Fig. 7.21 yields different slopes for the different systems. It is already well known that the number of valence electrons per atom ratio plays an important role in the lattice instability. The martensitic transition was found to be linearly increasing with increasing the ratio e/a (see chapter 3). To our knowledge such linearity of the soft phonon mode with e/a has not yet been reported. Furthermore, within the limited number of Ni-based samples investigated up to now and plotted on Fig. 7.21, the measure of the soft phonon frequency at room temperature might be an indicative parameter of its structural instability. Independently of the system, the soft phonon mode frequency at room temperature of samples which undergo a martensitic transformation upon cooling lies below 0.55 THz, whereas stable samples show soft phonon frequency at room temperature above 0.7 THz. These results support the idea of investigating other samples with different e/a ratio in different systems to get more insight on the role played

by the valence electron per atom ratio in lattice instability which is so far not fully understood. The guiding idea behind this research is to properly tune the e/a ratio of the alloys by a subtle variation in composition.

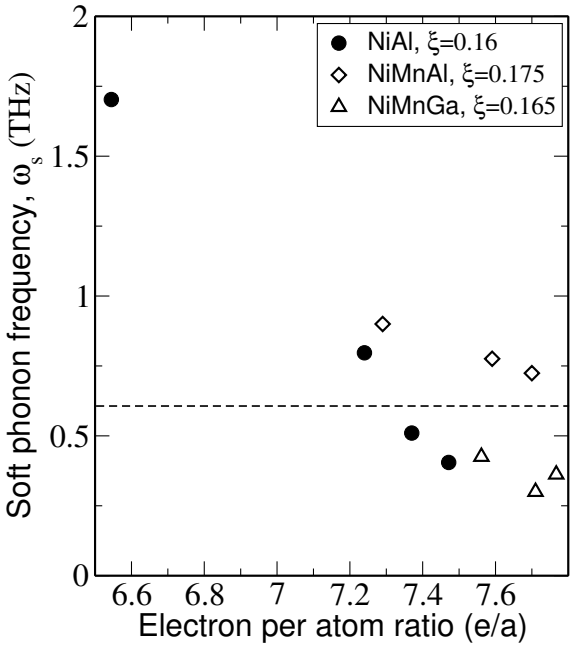

Figure 7.21: Soft phonon frequencies in Ni-based systems measured at, or close to, room temperature *versus* valence electron per atom ratio. The dashed line separates the stable samples (upper part) from sample which showed a martensitic transition upon cooling down (lower part). By stable sample is meant that no martensitic transformation was seen down to the lowest measured temperature.

Chapter 8

Outlook

8.1 Interplay of magnetism and vibrational degrees of freedom in MSM alloys

It is evident from the comparison of the measured phonon softening in the different Ni-based systems that the interplay of magnetism and lattice dynamics plays a key role in structural instability. Contrary to Ni_2MnAl, Heusler based ferromagnetic Ni_2MnGa, Ni_2MnSn and Ni_2MnIn alloys with concentrations close to the $L2_1$ stoichiometry are typical systems undergoing a martensitic transition within their ferromagnetic phase [Kre06a, Kre06b]. These magnetic shape memory (MSM) alloys are promising candidates for a new class of functional materials in which the shape recovery can be explored by an external magnetic field. In the martensitic state, the application of a magnetic field can cause strains up to about 10% [Soz02].

The interplay of magnetism and structural instability in the Heusler Ni-based magnetic shape memory alloys reveals fundamental differences. While in Ni_2MnGa the martensitic transformation is shifted to higher temperatures in an external magnetic field, Ni_2MnIn shows a reverse behaviour [Kre06a]. This result is supported by recent *ab-initio* calculations in Ni_2MnIn. The calculations predict that increasing magnetization due to an external field favours the high-temperature cubic phase and leads to a gradual vanishing of the phonon instability (Fig. 8.1) [Ent06a].

To get more insight on the interplay of magnetism and vibrational degrees of freedom, we plan in a first step to measure the magnetic field dependence of the acoustic and eventually optical phonons of austenitic Ni_2MnGa, Ni_2MnSn and Ni_2MnIn. Contrary to Ni_2MnGa, in which the temperature dependence of lattice dynamics in the austenitic phase has been widely investigated in the last decade, to our knowledge, no phonon measurements in Ni_2MnSn and Ni_2MnIn have been yet reported. Measurements of the optical phonons near the Brillouin zone center which are most sensitive to an overall weakness of the crystal towards the transformation can reveal phonon anomalies in optical modes which have been predicted by first-principle calculations [Ent06a] but not yet experimentally evidenced. Phonon measurements will serve to validate the interactions deduced from *ab-initio* calculations, which is mandatory for understanding the magnetoelastic coupling.

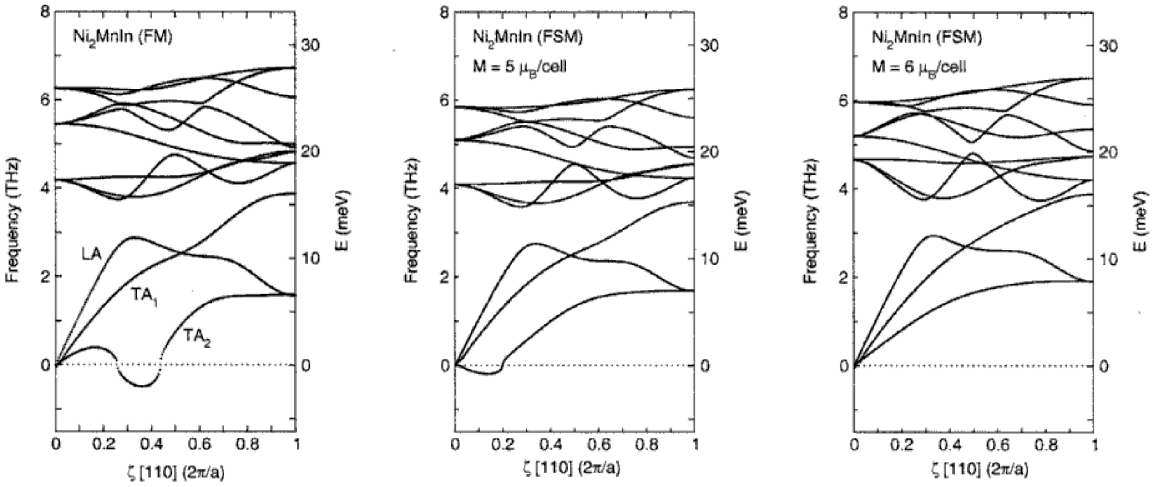

Figure 8.1: Influence of an external magnetic field on the phonon softening in ferromagnetic Ni_2MnIn using the fixed-spin moment method [Ent06a]. Note for a magnetic moment of $6\mu_B/cell$ the phonon softening has completely vanished (μ_B is the Bohr magneton).

8.2 Role of lattice dynamics in domain flipping in martensitic MSM alloys

The magnetic field induced strain in MSM alloys is caused by the reorientation of martensite variants by twin boundary motion. The driving force for the reorientation is provided by the difference in the Zeeman energy of neighbouring variants [Han98]. Lattice dynamics investigation in martensitic phase is up to now an open task. The transformation of a single crystal on cooling to the martensitic phase produces a twinned microstructre, resulting in differently oriented variants. This rules out the measurement of phonon dispersion relations as phonon energies measured for a multi-variant crystal cannot be related to wave vectors $\mathbf{q}$ along certain symmetry direction. However, single variants can be achieved, prior or during neutron measurements, by cooling the sample through the martensitic transition temperature under applied magnetic field or mechanical stress. We plan to measure the phonon response to external magnetic field in single variants of martensitic Ni_2MnGa, Ni_2MnSn and Ni_2MnIn. Dynamic precursor phenomena for the twinning process can be observed by the phonon response in a single variant when transforming from one variant to another or from a single variant to a multi-variant configuration. Acoustic and, eventually optical phonons near the Brillouin zone center are most sensitive to an overall weakness of the crystal towards the transformation. Phonons of short wavelength may tell us whether periodic modulations of twins are favourable. Phonon measurements under applied magnetic field in the martensitic phase will give more insight on the extent of lattice dynamics contribution to the domain flipping in magnetic shape memory alloys. First test measurements of phonons in a 7-layered single

variant martensitic Ni_2MnGa have been recently performed at the three-axis spectrometer PUMA (Forschungsneutronenquelle Heinz Maier-Leibnitz, FRM II) (see Fig. 8.2). The measurements revealed low-lying $TA_2[\xi\xi 0]$ phonon frequencies with a Brillouin zone boundary frequency of 2.5 THz.

This work is planned to be performed in the frame of a new collaborative research priority program SPP1239 entitled "Magnetic field induced modification of microstructure and form of solid materials".

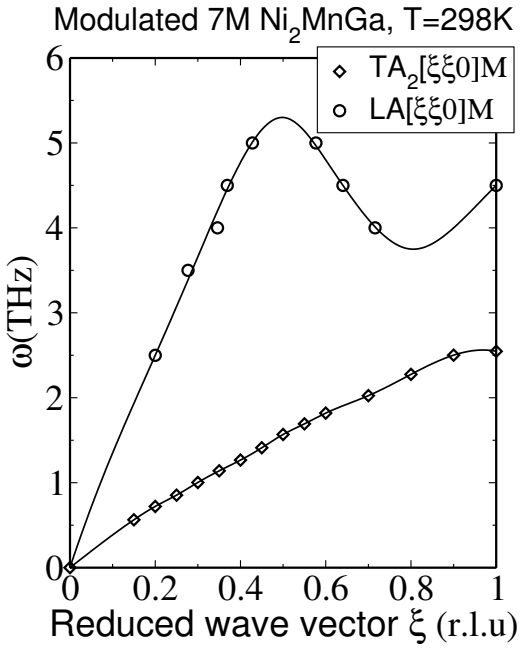

Figure 8.2: First phonons measured in a 7-layered single variant martensitic $Ni_{49}Mn_{31}Ga_{20}$ at room temperature.

Acknowledgment

This work has been done in the frame of my Ph.D thesis at the Forschungsneutronenquelle Heinz Maier-Leibnitz (FRM II) and at the E13 chair of physics department of the Technical University in Munich. It was accomplished during the period from January 2003 to June 2006 under the supervision of Dr. Jürgen Neuhaus. I thank everybody who directly and indirectly contributed to this thesis work. In this sense I wish to express my gratitude to

- Jürgen Neuhaus for his supervision and continuous support during the last three years
- Winfried Petry for giving me the opportunity to perform this thesis in his institute.
- Klaudia Hradil, Harald Schneider, Philippe Bourges and Arno Hiess for their assistance and their disponibility during the neutron scattering experiments performed respectively at PUMA (FRM II, Garching), 2T1(CEA, Saclay, France) and IN3 (ILL, Grenoble, France).
- Mr. Funer and Mr. Dörbecker of the E13 mechanical workshop who accurately performed all work for sample holders and the sample environment of neutron scattering experiments.
- Heiko Schneider, Katarzyna Danielewicz, Michael Stanger and Sonja Huber of the crystal lab who continously prepared the samples for the x-rays and the optical microscopy. Special thanks to Mr. Schneider for his numerous advises during the tedious task of crystal growth.
- all former and present PhD students and postdoctoral research fellows of E13 who welcomed me at the institute and permanently offer a pleasant working atmosphere.
- my parents, who have been away from the eyes but close to the heart. They have continuously supported my education and my research work.

Bibliography

[Ace02] M. Acet, E. Duman, E. F. Wassermann, Ll. Mañosa, and A. Planes J. Appl. Phys. **92**, (2002) 3867.

[And60] P. W. Anderson, *Fizika Dielektrikov*, ed. G.I. Skanavi, Akademia Nauk, Moscow (1960) 290.

[Bar81] J. Baram, M. Rosen, Philos. Mag. A. **44**, (1981) 895.

[Bha05] K. Bhattacharya, R. D. James, *Nature* **53**, (2005) 307.

[Blo94] P. E. Blöchl, Phys. Rev. B **50**, (1994) 17953.

[Bro60] B. N. Borckhouse, Bull. Amer. Phys. Soc. **5**, (1960) 462.

[Bru81] A. D. Bruce and R. A. Cowley, *Structural Phase Transitions*, Taylor and Francis, London (1981).

[Bru82] R. Bruinsma, Phys. Rev. B **25**, (1982) 2951.

[Bue63] W. J. Buehler, J. V. Gilfrich and K. C. Weiley, J. Appl. Physics **34**, (1963) 1467.

[Bue04] T. Büsgen, J. Feydt, R. Hadorf, S. Thienhaus, M. Moske, M. Boese, A. Zayak, and P. Entel, Phys. Rev. B **70**, (2004) 014111.

[Buh81] W. Bührer, O. Mercier, P. Brüesch, R. Gotthard, ETH Report, AF-SSP-115 (1981).

[Cas99] T. Castán, E. Vives, and P. Lindgard, Phys. Rev. B **60**, (1999) 7071.

[Ces97] E. Cesari, V. A. Chernenko, V. V. Kokorin, J. Pons, and C. Segu, Acta Mater. **45**, (1997) 999.

[Cher95] V. A. Chernenko, E. Cesari, V. V. Kokorin, and I. N. Vitenko, Scr. Metall. Mater. **33**, (1995) 1239.

[Cher99] V. A. Chernenko, Scr. Mater. **40**, (1999) 523.

[Chr75] J. W. Christian, *The Theory of Transformations in Metals and alloys*, 2nd ed. Pergamon Press, Oxford, (1975).

[Coc64] W. Cochran, Phys. Rev. **133**, (1964) 412.

[Deb12] P. Debye, *Ann. Phys., Lpz.* **39**, 789.

[Doo85] L. R. Doolittle, Nucl. Instr. Meth. B **9**, (1985) 344.

[Doy79] B. L. Doyle and P. S. Peercy, Appl. Phys. Lett. **34**, (1979) 811.

[Doy88] B. L. Doyle and D.K. Brice, Nucl. Instr. Meth. B **35**, (1988) 301.

[Due90] T. W. Duering in *Engineering aspects of Shape Memory Alloys*, Butterworth-Heinemann Ltd., London (1990).

[Eck04] G. Eckold, D. Caspary, P. Elter, F. Güthoff, A. Hoser, W. Schmidt, Physica B **350**, (2004) 83.

[Ecu76] J. L. Ecuyer, C. Brassard, C. Cardinal, J. Chabbal, L. Deschenes and J. P. Labrie, J. Appl. Phys. **47**, (1976) 381.

[Ent06a] P. Entel, M. E. Gruner, W. A. Adeagbo and A. T. Zayak, ESOMAT (2006).

[Ent06b] P. Entel, V. D. Buchelnikov, V. Khovailo, A. T. Zayak, W. A. Adeagbo,M. E. Gruner, H. C. Herper, E. F. Wassermann, J. Phys. D: Appl. Phys. **39**, 865 (2006).

[Flo87] T. Flottmann, W. Petry, R. Serve and G. Vogl, Nuclear Instruments and Methods in Physics Research **A260**, (1987) 165.

[Fuj00] A. Fujita, K. Fukamichi, F. Gejima, R. Kainuma, and K. Ishida, Appl. Phys. Lett. **77**, (2000) 3054.

[Fri94] G. Fritsch, V. V. Kokorin, and A. Kempf, J. Phys.: Condens. Matter **6**, (1994) 107.

[Gej99] F. Gejima, Y. Sutou, R. Kainuma and K. Ishida, Metall. Mater. Trans. A **30**, (1999) 2721.

[Gil66] G. Gilat, L. J. Raubenheimer, Phys. Rev. B **144**, (1966) 390.

[Hal76] B. I. Halperin and C. M. Varma. Phys. Rev. B **14**, (1976) 4030.

[Han98] R. C. O'Handley, J. App. Phys. **83**, 3263 (1998).

[Hei91] A. Heiming, W. Petry, J. Trampenau, M. Alba, C. Herzig, H. R. Schober, G. Vogl, Phys. Rev. B **43**, (1991) 10948.

[Hil56] T. L. Hill, *Statistical mechanics: principles and selected applications*, McGraw-Hill, New York 1956.

[Hod88] D. E. Hodgson, *Proceedings of Engineering Aspects of Shape Memory Alloys* Lansing, MI (1988).

[Hua01] X. Huang, C. Bungaro, V. Godlevsky, K. Rabe, Phys. Rev. B **65**, (2001) 14108.

[Joh69] O. Johari, G. Thomas, *The stereographic projection and its application*, interscience Publishers: New York (1969).

[Kai92] R. Kainuma, H. Nakano, K. Oikawa and K. Ishida and T. Nishizawa, Mat. Res. Soc. Symp. Proc. **246**, (1992) 403.

[Kai95] R. Kainuma, N. Ono, K. Ishida, Mat. Res. Soc. Symp. Proc. **360**, (1995) 467.

[Kai96] R. Kainuma, H. Nakano, and K. Ishida, Metall. Mater. Trans. A **27**, (1996) 4153.

[Kai98] R. Kainuma, M. Ise, K. Ishikawa, I. Ohnuma and K. Ishida, J. Alloys and Comp. **269**, (1998) 173.

[Kai00] R. Kainuma, F. Gejima, Y. Sutou, I. Ohnuma, K. Ishida, Mat. Trans. JIM **41**, (2000) 943.

[Kha02] J. Khalil-Allafi, A. Dlouhy, G. Eggeler, Acta Mater. **50**, (2002) 4255.

[Kit76] C. Kittel, "Introduction to solid state physics", Ed. J. Wiley, New-York (1976).

[Kre06a] T. Krenke, M. Acet, E. F. Wassermann, X. Moya, Ll. Mañosa and A. Planes, Phys. Rev. B **72**, 14412 (2006).

[Kre06b] T. Krenke, M. Acet, E. F. Wassermann, X. Moya, Ll. Mañosa and A. Planes, Phys. Rev. B **73**, 174413 (2006).

[Kre96] G. Kresse and J. Furthmüller, Phys. Rev. B **54**, (1996) 11169.

[Kre99] G. Kresse and D. Joubert, Phys. Rev. B **59**, (1999) 1758.

[Kri69] M. A. Krivoglaz, "Theory of x-ray and thermal neutron scattering by real crystals", Plenum Press (1969).

[Kru87] J. F. Krumme, Connect. Technol. **3** (No. 4), Apr. (1987) 41.

[Kru89] J. A. Krumhansl and R. J. Gooding, Phys. Rev. B **39**, (1989) 3047.

[Kru92] J. A. Krumhansl, Solid State Com. **84**, (1992) 251.

[Lan04] N. Lanska, O. Söderberg, A. Sozinov, Y. Ge, K. Ullako, V. K. Lindros, J. Appl. Phys. **95**, (2004) 8074.

[Lau74] E. Preuss, B. Krahl-Urban, R. Butz, *Laue Atlas*, Edited by Kernforschungsanlage Jülich, (1974).

[Lin89] P.-A. Lindgard and O. G. Mouritsen, Phys. Rev. B **57**, (1986) 2458.

[Lin90] P.-A. Lindgard and O. G. Mouritsen, Phys. Rev. B **41**, (1990) 688.

[Liu96] X. J. Liu, R. Kainuma, H. Ohtani, K. Ishida, J. Alloys and Comp. **235**, (1996) 256.

[Leh62] G. W. Lehman, T. Wolfram and R. E. De Wames, Phys. Rev. **128**, (1962) 1593.

[Lov84] S. M. Lovesey, *Theory of Neutron Scattering from Condensed Matter*, Oxford University Press (1984).

[Lov90] F. C. Lovey, A. Amengual, V. Torra, M. Ahlers, Philos. Mag. A **61**, (1990) 159.

[Man89] Ll. Mañosa, A. Planes, D. Rouby, M. Morin, P. Fleischmann, J. L. Macqueron, Appl. Phys. Lett. **54**, (1989) 2574.

[Man90] Ll. Mañosa, A. Planes, D. Rouby, J. L. Macqueron, Acta metal. **38**, (1990) 1635.

[Man93] Ll. Mañosa,J. Zarestky, T. A. Lograsso, D. W. Delaney and C. Stassis, Phys. Rev. B **48**, (1993) 15708.

[Man97] Ll. Mañosa, A. Gonzàlez-Comas, E. Obradó, A. Planes, V. A. Chernenko, V. V. Kokorin, and E. Cesari, Phys. Rev. B **55**, (1997) 11068.

[Man99] Ll. Mañosa, J. Zarestky, M. Bullock, and C. Stassis, Phys. Rev. B **59**, (1999) 9239.

[Man00] Ll. Mañosa and A. Planes, Adv. Solid State Phys. **40**,(2000) 361.

[Man01] Ll. Mañosa and A. Planes, J. Zarestky, T. Lograsso, D. L. Schlagel, and C. Stassis Phys. Rev. B **64**, (2001) 24305.

[Mas90] T. B. Massalski et al (Eds.), *Binary Alloys Phase Diagrams*, 2nd ed., ASm International (1990).

[Mat02] H. Matsumoto, Journal of Alloys and Compounds **350**, (2002) 13.

[Mil71] A. J. Millington, G. L. Squires, J. Phys. F: Met. Phys. **1**, (1971) 244.

[Mor93] A. Nagasawa and Y. Mori, Mater. Trans. JIM. **34**, (1993) 855.

[Mor96] S. Morito and K. Otsuka, Mater. Sci. Eng. A **208**, (1996) 47.

[Moy06a] X. Moya, Ll. Mañosa, A. Planes, T. Krenke, M. Acet, V. O. Garlea, T. A. Lograsso, D. L. Schlagel, and J. L. Zarestky, Phys. Rev. B **73**, (2006) 064303.

[Moy06b] X. Moya, Ll. Mañosa, A. Planes, T. Krenke, M. Acet, M. Morin, J. L. Zarestky, T. A. Lograsso, Phys. Rev. B **74**, 024109 (2006).

[Neu91] J. Trampenau, Ph.D Thesis, Wilhems-University Münster (1991).

[Nic00] K. Nicolaus, Ph.D Thesis, Technical University Munich, (2000).

[Nic01] K. Nicolaus, J. Neuhaus, W. Petry, and J. Bossy, Eur. Phys. J. B **21**, (2001) 357.

[Ort91] J. Ortin, A. Planes, J. Phys. IV (Paris) **1**, (1991). C4-13.

[Ots99] K. Ostuka, X. Ren, Mater. Sci. Eng. A **273-275**, (1999) 89.

[Ots02] K. Ostuka, X. Ren, Materials Science Forum **394-395**, (2002) 177.

[Ove84] A. W. Overhauser, Phys. Rev. Lett. **53**, (1984) 64.

[Pas75] R. Pascual, M. Ahlers, R. Rapacioli, W. Arneodo, Scripta metall. **9**, (1975) 79.

[Per96] J. P. Perdew, K. Burke, and Y. Wang, Phys. Rev. B **54**, 16533 (1996).

[Pet91a] W. Petry, A. Heiming, J. Trampenau, M. Alba, H. R. Schober and G. Vogl, Phys. Rev. B **43**, (1991) 10933.

[Pet91b] J. Trampenau, A. Heiming, W. Petry, M. Alba, C. Herzig, W. Mickeley and H. R. Schober, Phys. Rev. B **43**, (1991) 10963.

[Pet91c] W. Petry, *Martensitic Transition in bcc Metals: Diffusion and Phonons*, Institut Laue-Langevin Grenoble, (1991).

[Pla81] A. Planes, J. L. Macqueron, M. Morin, G. Guénin, Phys. Stat. Sol. (A) **66**, (1981) 717.

[Pla82] A. Planes, J. L. Macqueron, M. Morin, G. Guénin, L. Delaey, J. Phys. (Paris) **43**, (1982) C4-615.

[Pla92] A. Planes, J. Ortin, J. Appl. Phys. **71**, (1992) 950.

[Pla97] A. Planes, E. Obradó, A. Gonzàlez-Comas and Ll. Mañosa, Phys. Rev. Lett. **79**, (1997) 3926.

[Sha89] S. M. Shapiro, B. X. Yang, G. Shirane, Y. Noda, L. E. Tanner, Phys. Rev. Lett. **62**, (1989) 1298.

[Sha91] S. M. Shapiro, B. X. Yang, Y. Noda, L. E. Tanner and D. Schryvers, Phys. Rev. B **44**, (1991) 9301.

[Sch92] W. Schwarz, O. Blaschko, I. Gorgas, Phys. Rev. B **46**, (1992) 14448.

[Shi06] G. Shirane, S. M. Shapiro and J. M. Tranquada, *Neutron Scattering with a Triple-Axis Spectrometer: Basic Techniques*, Cambridge University Press, (2006) p.283.

[Soz02] A. Sozinov, A. A. Likhachev, N. Lanska, and K. Ullako, Appl. Phys. Lett. **80**, (2002) 1746.

[Smi87] H. G. Smith, Phys. Rev. Lett. **58**, (1987) 1228.

[Squ78] G. L. Squires, *Introduction to the Theory of Thermal Neutron Scattering*, Cambridge University Press (1978).

[Stu97] U. Stuhr, P. Vorderwisch, V. V. Kokorin, and P.-A. Lindgard, Phys. Rev. B **56**, (1997) 14360.

[Sri90] G. P. Srivastava, *The physics of phonons*, ed. Adam Hilger, Bristol (1990).

[Suo04] I. Suorsa, E. Pagounis, J. Appl. Phys. **95**, (2004) 4958.

[Tan77] C. Cohen-Tanoudji, B. Diu and F. Laloe, *Quantum Mecanics*, Wiley-Interscience publication (1977), p. 898.

[Tie84] H. Tietze, K. Müllner, B. Renker, J. Phys. C: Solid State Phys. **17**, L529 (1984).

[Vas99] A. N. Vasil'ev, A. D. Bozhko, V. V. Khovailo, I. E. Dikshtein, V. G. Shavrov, C. D. Buchelnikov, M. Matsumoto, S. Suzuki, T. Takagi, and J. Tani, Phys. Rev. B **59**, (1999) 1113.

[Viz90] G. Vizkelethy, Nucl. Instr. Meth. B **45**, (1990) 1.

[Wad84] H. N. G. Wadle, J. A. Simmons, J. Res. Nat. Bur. Stand. **98**, (1984) 55.

[Wal87] E. Waldbusser, Semicond. Saf. Assoc. J. Aug (1987), 34

[Woo62] A. D. B. Woods, B. N. Brockhouse, R. H. March, A. T. Stewart and R. Bowers, Phys. Rev. B **128**, (1962) 1112.

[Wor96] J. Worgull, E. Petti, and J. Trivisonno, Phys. Rev. B **54**, (1996) 15695.

[Yam86] Y. Yamada, *Proc. Int. Conf. on martensitic Transformations*, Japan Institute of Metals, Nara Japan, (1986) p.89

[Yam92] Y. Yamada, Mater. Trans. JIM **33**, (1992) 191.

[Yu87] Z. Yu, P. C. Clapp, J. Appl. Phys. **62**, (1987) 2212.

[Zay05] A. T. Zayak, P. Entel, K. M. Rabe, W. A. Adeagbo, and M. Acet, Phys. Rev. B **72**, (2005) 054113.

[Zay06] A. T. Zayak, W. A. Adeagbo, P. Entel and K. M. Rabe, Appl. Phys. Lett.**88**, (2006) 111903.

[Zen47] C. Zener, Phys. Rev. **71**, (1947) 846.

[Zha92] G. L. Zhao and B. H. Harmon, Phys. Rev. **45**, (1992) 2818.

[Zha06] Z. Zhang, J. Frenzel, Ch. Somsen, J. Pesicka, K. Neuking and G. Eggeler, Mater. Sc. and Eng.: A **438-440**, (2006) 879.

[Zhe95] A. Zheludev, S. M. Shapiro, P. Wochner, A. Schwarz, M. Wall, and L. E. Tanner, Phys. Rev. B **51**, (1995) 11319.

[Zhi03] H. Zhi-Rong, Z. Jing-En, Mater. Sc. and Eng. A **360**, (2003) 183.

[Zie75] K. R. A. Ziebeck and P. J. Webster, J. Phys. F: Met. Phys. **5**, (1975) 1756.